The Dissertation Committee for Byoung-ick Cho Certifies that this is the approved version of the following dissertation:

Experimental Study of Fast Electrons from the Interaction of Ultra Intense Laser and Solid Density Plasmas

Committee:

Todd Ditmire, Supervisor

Boris N. Breizman

Michael C. Downer

Greg O. Sitz

Shaochen Chen

Experimental Study of Fast Electrons from the Interaction of Ultra Intense Laser and Solid Density Plasmas

by

Byoung-ick Cho, B.S.

Dissertation

Presented to the Faculty of the Graduate School of
The University of Texas at Austin
in Partial Fulfillment
of the Requirements
for the Degree of

Doctor of Philosophy

The University of Texas at Austin
August, 2008

To my family

Acknowledgements

It is great pleasure for me to express gratitude for people who helped me completing this work. Without them, I can hardly imagine the works in the thesis would be realized.

First, I would like to thank my advisor, Professor Todd Ditmire. His energy, enthusiasm, and supports always encouraged and inspired me during past six years. Furthermore I really appreciate that he has shown me a great vision in science. I believe that it will be great nutrients for my future scientific carrier.

I thank to my colleagues in our group and collaborators in other institutes. Dr. Greg Hays was so kind enough to share his great lab skills with me from the very first day in the lab. With Dr. Gilliss Dyer and Stefan Kneip, we had non-stop day and night shifts with a lot of excitement and fun. I believe we were a great solid target team. Dr. Jens Osterholz visited our group and gladly shared his knowledge about CTR with us, in particular with me. Though it was only one year visiting, we had very productive time and his prudence on science influenced me a lot. Professor Nathalie Lenard-Re Galloudec has provided us excellent cone targets. For several years and all subjects for thesis, she has been a great collaborator.

I also should mention my appreciation to dear friends. Dr. Bonggu Shim, Dr. Yunpil Shim, and Dr. Suyong Jung and I were grilling Sam-gyub-sal, watching TV and drinking together on almost every Saturday for years. In Austin, it was the most comfortable and relaxed time that I will never forget. I also want to thank to Hyo Jeong Kim. She is a delightful friend to chat about every subjects; literature, music, science and even politics. Her knowledge and interests about wide range of topics always entertained me a lot.

Finally, I thank all of my family for their endless love. Ever since I was a kid, my parents Myong-won Cho and Kye-ock Chang taught me to be a right person and

respect knowledge. My grandmother Jeong-ock Lee let me have confidence for what I do. They always esteemed their boy's opinions and decisions, and supported him seamlessly. Now they pray for him everyday. My young brother Byoung Hooi Cho had been with parents and grandmother when I had to but couldn't. Now he also cares his brother a lot while he is busy with his own Ph.D works. Without them, I might not be myself after all. I would like to dedicate this thesis to all my family.

BYOUNG-ICK CHO

The University of Texas at Austin
August 2008

Experimental Study of Fast Electrons from the Interaction of Ultra Intense Laser and Solid Density Plasmas

Publication No._____

Byoung-ick Cho, Ph.D.
The University of Texas at Austin, 2008

Supervisor: Todd Ditmire

A series of experiments have been performed to understand fast electron generation from ultra intense laser-solid interaction, and their transports through a cold material. Using Micro-Electro-Mechanical Systems (MEMS), we contrived various shape of cone and wedge targets. The first set of experiment was for investigating hot electron generations by measuring x-ray production in different energy ranges. $K\alpha$ and hard x-ray yields were compared when the laser was focused into pyramidal shaped cone targets and wedge shaped targets. Hot electron production is highest in the wedge targets irradiated with transverse polarization, though $K\alpha$ is maximized with wedge targets and parallel polarization. These results are explained with particle-in-cell (PIC) simulations utilizing PICLS and OOPIC codes. We also investigate hot electron transport in foil, wedge, and cone targets by observing the transition radiation emitted from the targets rear side along with bremsstrahlung x-ray measurement. Two-dimensional images and spectra of 800 nm coherent transition radiation (CTR) along with ballistic electron transport analysis have revealed the spatial, temporal, and temperature characteristics of hot electron micro-pulses. Various patterns from different target - laser configurations suggest that hot electrons were guided by the strong static

electromagnetic fields at the target boundary. Evidence about fast electron guiding in the cone is also observed. CTR at 400 nm showed that two distinct beams of MeV electrons are emitted from the target rear side at the same time. This measurement indicates that two different mechanisms, namely resonance absorption and $\boldsymbol{j} \times \mathbf{B}$ heating, create two populations of electrons at the targets front side and drive them to different directions, with distinct temperatures and temporal characteristics. This interpretation is consistent with the results from 3D-PIC code Virtual Laser Plasma Laboratory (VLPL).

Table of Contents

List of Tables

List of Figures

CHAPTER 1. INTRODUCTION

The interaction of intense laser and solid density matter has become a popular subject in recent years. It is well known that the irradiation of a solid surface with a high intensity laser leads to the production of energetic electron beams [1-4] and these keV and/or MeV electrons have been often observed in various short pulse laser-plasma experiments with focal intensities above 10^{18} W/cm^2 [5, 6]. Hot electrons also interact with cold material and produce x-ray radiations [7-9] and other energetic particles [10-12]. Since these photons and particles have extremely high energies and short time scale, researches in this field have contributed many applications, such as laser-fusion experiment [13], ultrafast radiographic source development [8], laser particle acceleration [14] and warm dense matter study [15-17].

Especially for the laser driven fusion experiment, a reentrant cone target was introduced to spark the fast ignition at the center of an imploding deuterium pellet [13]. The conical geometry may guide and deliver a large number of directed, high energy laser accelerated electrons into a small and predetermined region at the cone tip. This advantage is also very important to create high energy density and particle fluxes relevant to various applications previously mentioned. However, despite a number of suggestive experimental and computational results [14, 18-20], the nature of the interaction of an intense light pulse with fast electrons in such structures is not yet well understood and whether laser focusing and electron guiding can indeed occur in a cone target has not yet been definitively established.

The first motivation of this thesis comes from the interests about the cone target. Hence this thesis describes an experimental campaign to examine fast electron heating from various micro-structured targets. For this purpose we developed silicon based pyramidal cone and wedge targets using Micro-Electro-Mechanical System (MEMS) and present x-ray spectroscopy data obtained from these targets. Though the majority of

works in the thesis are devoted to experimental investigations, simulations and theoretical works are also included to explain appropriate physics. Therefore, results from particle-in-cell (PIC) simulations are also discussed to explain our x-ray data.

At the relativistic laser intensity, it is known that not only eclectic fields but also magnetic fields of the laser itself as well as self-generated, quasi-static fields play significant roles on plasma dynamics. Physics in these conditions are particularly complex and difficult. In particular, associated with cone target physics, an extensive knowledge about fast electron transports is very essential. Conventionally it has been studied by various groups with various methods, either directly by measurement of electron energy spectra using an electron spectrometer [21] or indirectly by x-ray measurements [9, 22, 23] and Cerenkov radiations [24, 25].

A more direct way to measure the emergence of hot electrons from the rear side of a target is by observing the transition radiation that is emitted when the hot electrons transit an interface in the dielectric function when they cross from the target material into vacuum [26]. Some early works showed that it is very useful tool providing sets of information which have been hardly determined by other methods [27-31].

The second motivation of this thesis arose from the attention to the transition radiation. In particular, coherent transition radiation (CTR) which has spectral peaks at harmonics of laser frequency, has been measured in another experimental campaign. Various CTR signals from various targets, including cone and wedge targets, are presented. Along with experimental data, theoretical analysis and PIC simulation results are also discussed and compared each other. These efforts make extensive studies for fast electron transports possible.

Hence this thesis is organized by the following. The next chapter gives an overview of the physics about the intense laser – solid interactions. It is followed by the chapter 3, in which about experimental setups are presented; the THOR laser, targets, and diagnostics. In the chapter 4, details about target fabrication procedure are described. Not only cone and wedge targets for this thesis, techniques in this chapter could have

been applied to also various other experiments, such as silicon shock targets and warm-dense matter targets. In the chapter 5 [32], $K\alpha$ and bremstrahlung x-ray measurement data from cone and wedges which were irradiated by the THOR laser are discussed with PIC simulation results. It reveals the several interesting physical aspects about high energy electron generations under the laser – cone configurations. In the chapter 6 [33-35], 800 nm and 400 nm coherent transition radiations are experimentally investigated along with theoretical modeling and 3D-PIC simulations. We simultaneously observed a multiple electron beams were generated and their transportations were strongly affected by quasi-static electromagnetic fields. Finally, the chapter 7 concludes the thesis, summarizing results and discussing future works.

CHAPTER 2. PHYSICS OF ULTRA INTENSE LASER – SOLID INTERACTIONS

The interaction of laser light with solid density plasma involves a variety of processes and mechanisms: ionization, laser propagation and refraction, plasma wave generation, and subsequent thermal and hydrodynamic evolution of targets. In the Figure 1 [36], the noticeable phenomena in the laser – solid interaction are summarized. These processes are greatly dependent on laser parameters; namely irradiance $I\lambda^2$. The energy electron can pick up from the laser is about order of the pondermotive energy in the electric field $U_p = e^2E^2/4m_e\omega^2$. At the irradiance of 10^{16} W/cm^2·μm^2, for example 800 nm Ti:sapphire laser with $I = 1.56 \times 10^{16}$ W/cm^2, the pondermotive energy is 1 keV.

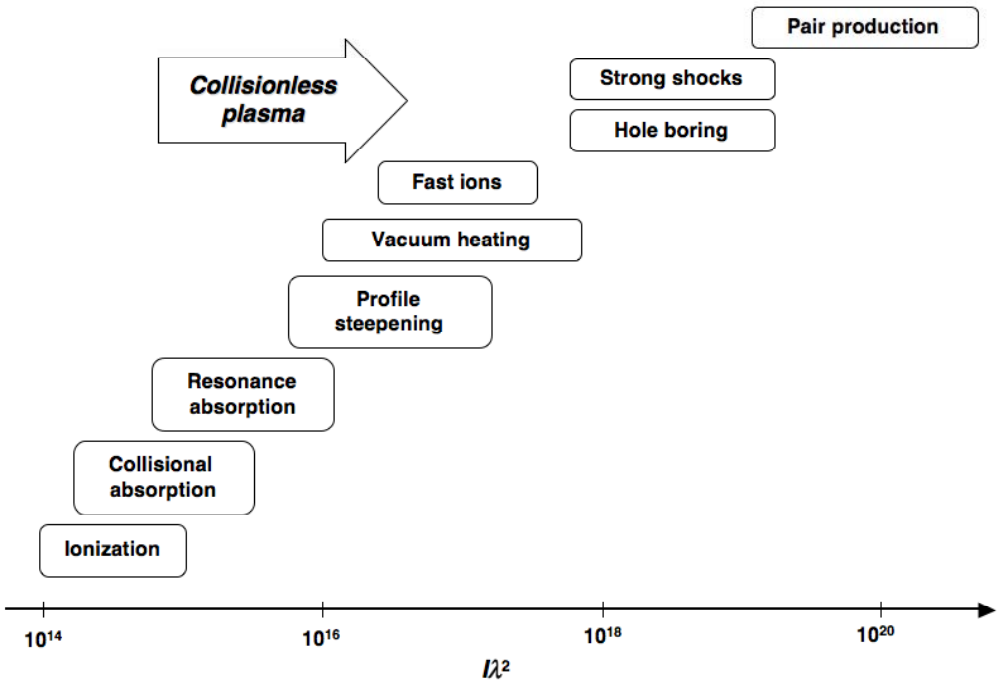

Figure 1. Physics of fs laser interaction with solid.

It is generally considered a threshold of collisonless plasma and the resonance absorption produces hot electrons. As the laser intensity increase, other phenomena start to be activated, such as vacuum heating and ion accelerations. As the laser intensity increases even higher, there is another laser parameter we need to note; the normalized vector potential $a = eA/m_e c^2 = (2e^2\lambda^2/\pi m_e^2 c^5)$. When this potential becomes the unity ($I\lambda^2 = 1.37 \times 10^{18}$ W/cm^2·μm^2), the energy in the magnetic field of the laser becomes comparable to that in the electric field. MeV electron acceleration by $\boldsymbol{v} \times \boldsymbol{B}$ force is a typical example in this regime. Therefore, relativistic treatment of plasma dynamics is very essential in this ultra high intensity regime.

In this chapter, I will overview theories about some noticeable features in ultra intense laser – solid interactions. The chapter 2.1 is mainly for hot electron generation mechanism; resonance absorption, Brunel-type heating, and $\boldsymbol{j} \times \mathbf{B}$ heating. In the following chapter 2.2, fast electron transports and their instabilities will be discussed. Finally, in the chapter 2.3 and 2.4, theories for subsequent radiative phenomena such as x-ray generation and transition radiations will be presented.

2.1. EM PROGARAGION IN A PLASMA GRADIENT AND HOT ELECTRON GENERATIONS

When a laser pulse propagates through plasma, plasma charge densities oscillate in the electromagnetic fields and plasma also makes effects on the propagation of electromagnetic waves. Here we can start from a simple situation, the non-relativistic plasma. Therefore electrons are driven by only electric field and self-generated magnetic fields are not considered.

Wave equations for the oscillating electric and magnetic fields in the plasma can be derived from Faraday's law and Ampere's law;

$$\nabla \times \mathbf{E} = \frac{i\omega}{c}\mathbf{B}, \tag{1}$$

$$\nabla \times \mathbf{B} = \frac{4\pi}{c}\sigma\mathbf{E} - \frac{i\omega}{c}\mathbf{E}. \tag{2}$$

σ is the high frequency conductivity of plasma and given by $\sigma = i\omega_p^2/4\pi\omega$, where ω_p is the plasma frequency. Then Eq. (2) becomes

$$\nabla \times \mathbf{B} = -\frac{i\omega}{c}\varepsilon\mathbf{E} \tag{3}$$

where $\varepsilon = 1 - \omega_p^2/\omega^2$, which is the dielectric function of the plasma. Substituting the curl of Eq. (1) into Eq. (3) results in

$$\nabla^2\mathbf{E} - \nabla(\nabla\cdot\mathbf{E}) + \frac{\omega^2}{c^2}\varepsilon\mathbf{E} = 0. \tag{4}$$

The equation for **B** driven in a similar way is given by

$$\nabla^2\mathbf{B} + \frac{\omega^2}{c^2}\varepsilon\mathbf{B} - \frac{1}{\varepsilon}\nabla\varepsilon\times(\nabla\times\mathbf{B}) = 0. \tag{5}$$

2.1.1. Resonance absorption

Let's consider a linearly polarized laser light incident onto a plasma slab with angle of incidence θ, which is defined by an angle between the laser propagating vector (**k**) and the direction of plasma density gradient ($\hat{z}$). Here we set a plane of incidence as a *y*-*z* plane, and the vacuum plasma interface as $z = 0$, without loosing generality.

S-polarization

When an electric field is pointing out *y*-*z* plane, it can be set as $\mathbf{E} = E_x\hat{x}$ and the wave equation [Eq. (4)] becomes

$$\frac{\partial^2 E_x}{\partial y^2} + \frac{\partial^2 E_x}{\partial z^2} + \frac{\omega^2}{c^2}\varepsilon(z)E_x = 0 . \quad (6)$$

Since *y*-component of laser propagating vector should be conserved, $k_y = (\omega / c)\sin\theta$ and

$$E_x = E(z)\exp\left(\frac{i\omega y \sin\theta}{c}\right). \quad (7)$$

Substituting Eq. (7) into Eq. (6) results in

$$\frac{d^2 E(z)}{dz^2} + \frac{\omega^2}{c^2}\left[\varepsilon(z) - \sin^2\theta\right]E(z) = 0 . \quad (8)$$

It is obvious that the obliquely incident electromagnetic wave reflects where $\varepsilon(z) = \sin^2\theta$. At this plane electron density is $n_e = n_{crit}\cos^2\theta$, where n_{crit} is the critical density defined by $n_{crit} = m_e\omega^2 / 4\pi e^2$.

***P*-polarization**

Now let's consider the case the electric field of the wave lies in the plane of incidence, namely, *p*-polarized wave. In this case, there exists an electric field component (E_z) parallel to the direction of density gradient of plasma. Although the obliquely incident light reflects at the surface of $\varepsilon(z) = \sin^2\theta$, where its density is less than the critical density, it can still tunnel into the critical surface and drives fluctuations in plasma density.

Let's start from the Poisson's equation;

$$\nabla \cdot (\varepsilon \mathbf{E}) = 0 . \quad (9)$$

Since ε is a function of z and E_y must be conserved, Eq. (9) becomes

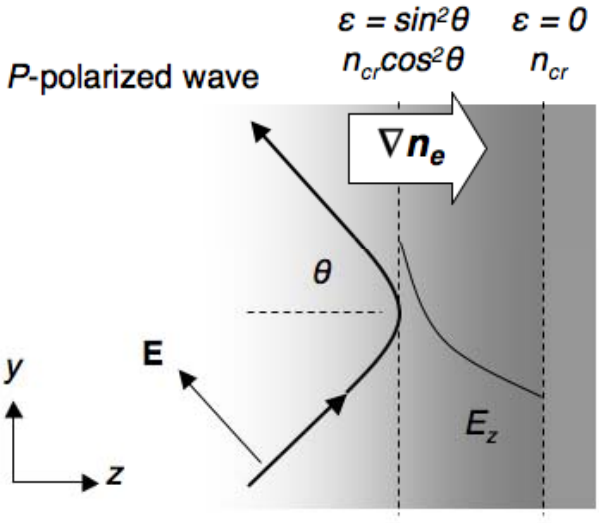

Figure 2. *P*-polarized light obliquely incident onto a plasma slab.

$$\nabla \cdot \mathbf{E} = -\frac{1}{\varepsilon}\frac{\partial \varepsilon}{\partial z} E_z . \tag{10}$$

Note that where $\varepsilon = 0$, i.e. the plane of critical density, the resonance can happens.

To determine the size of electric field at the point of resonance, we should find **E** and **B** fields at this plane. The magnetic field for *p*-polarized case is $\mathbf{B} = \hat{x} B_x$ and similar to Eq. (7), **B** field can be written as

$$\mathbf{B} = \hat{x} B(z) \exp\left(-i\omega t + \frac{i\omega y \sin\theta}{c} \right). \tag{11}$$

The associated **E** field is also found using Ampere's law [Eq. (3)]. The *z*-component of electric field is driven as

$$E_z = \frac{\sin\theta B(z)}{\varepsilon(z)} . \tag{12}$$

With an approximation $E_z = E_d / \varepsilon(z)$, the resonant driving field at the critical density E_d is estimated as the following form

$$E_d = \sin\theta \cdot B(z = L\cos^2\theta)e^{-\beta}. \tag{13}$$

Here we assume a linear density profile ($n_e = n_{crit} z / L$). Then the turning point of laser is $z = L\cos^2\theta$. Magnitude of magnetic field at the critical surface is evaluated from the exponential decaying of the field at the reflection plane and the decaying factor is defined as [37]

$$\beta = \int_{L\cos^2\theta}^{L} \frac{1}{c}\sqrt{\omega_p^2 - \omega^2\cos^2\theta}\,dz = (2\omega L/3c)\sin^3\theta. \tag{14}$$

Introducing a new variable $\tau = (\omega L/c)^{1/3}\sin\theta$, we find

$$E_d = \frac{E_{FS}}{\sqrt{2\pi\omega L/c}}\phi(\tau) \tag{15}$$

where E_{FS} is the electric field of laser in the free space, and $\phi(\tau) \cong 2.3\tau\exp(-2\tau^3/3)$. Eq. (15) implies that there is an optimum angle of incidence for the maximum absorption. E_d vanishes as τ (or θ) approaches zero, since the component of electric field of laser parallel to the plasma gradient is proportional to $\sin\theta$. When angle of incidence is large ($\theta \to 90°$), the distance that the evanescent wave has to penetrate is too large and the driver field intensity becomes small. Hence between these two limits, there is the optimum angle of incidence found as

$$\theta_{\max} \approx \sin^{-1}\left[0.8(c/\omega L)^{1/3}\right]. \tag{16}$$

The large amplitude of plasma wave is damped by various processes, such as electron-ion collisions, wave-particle interactions or even the wave and particle propagation out of the resonant region. Again assuming the linear density profile and small damping frequency ($\nu/\omega << 1$), the absorbed energy flux is given by [37]

$$I_{abs} \approx \frac{\omega L E_d^2}{8} = f_A \frac{c E_{FS}^2}{8\pi} \tag{17}$$

where f_A is the fractional absorption of the laser energy.

Through these resonant processes, absorbed laser energy is mainly converted into electron kinetic energy without collisions and they are driven once inward and once outward of the target per single laser cycle.

2.1.2. Vacuum heating (Brunel-type heating)

Vacuum heating, also known as Brunel's heating, was first described by F. Brunel for the case an intense electromagnetic field is incident obliquely on a "sharp" plasma

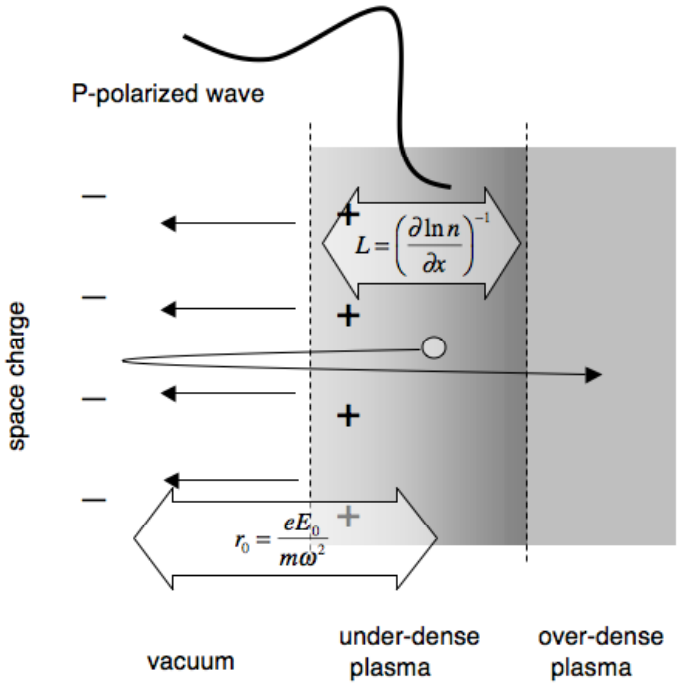

Figure 3. Strongly *p*-polarized laser pulse can directly pull electrons out of the sharp boundary of plasma and send them into clod plasma.

boundary [3] and experimentally confirmed by M. Downer, *at al*. [38] When an electron quiver radius in the strong laser field is greater than plasma scale length, electrons are pulled into vacuum in a first half of laser cycle and sent back to the over dense region in next half of cycle with the velocity $v \cong v_{osc} = eE_0 / m_e\omega$.

The energy picked up by electron is about an order of the energy stored in the electric field of laser, therefore the energy absorption in the time period $2\pi/\omega$ (or the absorbed power) is given by

$$I_{VH,abs} \approx \frac{\eta}{2\pi} v_{osc} \frac{E_0^2}{8\pi}. \tag{18}$$

We note that for the classical resonance absorption, absorption power is $I_{RA,abs} \approx \left(E_d^2/8\pi\right)L\omega$ for the case of $v/\omega << 1$. However for the vacuum heating, a distance is necessary to shield the electrostatic field by the space charge separation for the plasma at the critical density, i.e. $v_{osc}/\omega = r_0 > L = \left(\partial \ln n/\partial x\right)^{-1}$. Under this condition, the resonant absorption mechanism hardly takes place.

2.1.3. *j* × B heating

If the laser intensity becomes high enough ($a \geq 1$), the magnetic field becomes important to describe electron motion in the laser field. Let's consider the motion of electron in the laser field near the vacuum – plasma interface. The equation of motion is given by [39]

$$\frac{\partial \mathbf{p}}{\partial t} + \mathbf{v}\cdot\nabla\mathbf{p} = -e\left[\mathbf{E} + \frac{\mathbf{v}\times\mathbf{B}}{c}\right] \tag{19}$$

where **p** is relativistic momentum; $\mathbf{p} = \gamma m_e \mathbf{v}$. The r.h.s of Eq. (19) (the Lorenz force) clearly depicts the nature that electrons accelerated by the **E** field are pushed by **v** × **B** forces in the direction of laser propagation.

Replacing **E** and **B** with the vector (**A**) and electrostatic (ϕ) potentials and decomposing **p** into transverse ($\mathbf{p}_T$) and longitudinal ($\mathbf{p}_L$) components, the Eq. (19) can be rewritten as two equations;

$$\frac{\partial \mathbf{p}_T}{\partial t} = -\frac{e}{c}\frac{\partial \mathbf{A}}{\partial t}, \tag{20}$$

$$\frac{\partial \mathbf{p}_L}{\partial t} = e\nabla\phi - \frac{\mathbf{p}\cdot\nabla\mathbf{p}}{m_e\sqrt{1+\mathbf{p}^2/(m_e c)^2}} - \frac{e}{m_e c}\frac{\mathbf{p}}{\sqrt{1+\mathbf{p}^2/(m_e c)^2}}\times\nabla\times\mathbf{A}. \tag{21}$$

Since $\gamma = 1/\sqrt{1-v^2/c^2} = 1/\sqrt{1-\mathbf{p}^2/(\gamma m_e c)^2}$, we could set $\gamma = \sqrt{1+\mathbf{p}^2/(m_e c)^2}$ to obtain the above equations.

Now, we can replace $\nabla\times\mathbf{A}$ into $c/e\,\nabla\times\mathbf{p}_T = c/e\,\nabla\times\mathbf{p}$ because of $\nabla\times\mathbf{p}_L = 0$. Using a vector identity $\nabla\mathbf{p}^2/2 = \mathbf{p}\cdot\nabla\mathbf{p} + \mathbf{p}\times(\nabla\times\mathbf{p})$, Eq. (21) can be rewritten as

$$\frac{\partial \mathbf{p}_L}{\partial t} = e\nabla\phi - m_e c^2\nabla\sqrt{1+\frac{\mathbf{p}^2}{m_e^2 c^2}}. \tag{22}$$

It is clear that the second term of the r.h.s of Eq. (22) is nothing but the acceleration by the relativistic pondermotive force;

$$\mathbf{f}_p = -\nabla U_p = -m_e c^2\nabla(\gamma - 1) \tag{23}$$

where U_p is the relativistic pondermotive potential.

Therefore, the energy of electron accelerated by it is about an order of the ponderomotive energy and the electron temperature of these hot electrons can be scaled by

$$T_{hot} \approx m_e c^2\left(\sqrt{1+\frac{I\lambda^2}{2.8\times10^{18}}} - 1\right). \tag{24}$$

Considering non-relativistic case of $\boldsymbol{j} \times \mathbf{B}$ heating would be quite convenient to understand some properties of this mechanism. When a linearly polarized light with an electric field of $\mathbf{E} = \hat{\mathbf{y}} E_L(x) \sin \omega_0 t$, the pondermotive force exerted by this field is given by [1]

$$\mathbf{f}_p = -\hat{\mathbf{x}} \frac{m_e}{4} \frac{\partial}{\partial x} v_L^2(x) \left(1 - \cos 2\omega_0 t\right) \tag{25}$$

where $v_L = eE_L / m_e \omega_0$. The time-averaged part of this force pushes the plasma and produces the steepening of the density profile. The oscillating component of it drives the electro-static field. The corresponding driving field E_d is given by

$$\frac{eE_d}{m_e} = \frac{1}{4} \frac{\partial}{\partial x} v_L^2(x) \cos 2\omega_0 t \,. \tag{26}$$

This field E_d contributes the electron heating along the laser propagation direction. Since the magnitude of E_d is proportional to v_L and $\partial v_L/\partial x$, a significant absorption expected for the very high laser intensity (v_L is large) and at the region where plasma density varies very rapidly ($\partial x \to 0$). It should be noted that this mechanism drives electrons twice per a single laser cycle, in comparison to once per laser cycle for resonance absorption and vacuum heating.

2.1.4. Other mechanisms

Beside the absorption mechanisms described in the previous sections, various processes (collisional heating, stimulated Raman scattering, and hole boring, etc.) happen depending on the different laser – plasma parameters, as shown in the Figure 1. In particular, when laser intensity becomes very high and relativistic, various processes happen simultaneously and a whole interaction becomes very exotic and complex. Therefore in this section, I also add a brief introduction about couple of noticeable features.

Inverse bremsstrahlung

When an electron is in the free space, though it gets pondermotive energy from the oscillating electric field of laser, it will loose energy again when the field disappears. However, if a third particle (ion) is located in the vicinity of electron, a collision between electron and ion breaks the adiabaticity and kinetic energy of electron can be transferred to an ion. This process is called inverse bremsstrahlung and it is a most relevant collisional heating process in the plasma. In the non-relativistic case, the spatial damping rate of the laser energy is given by [40]

$$\kappa \propto \frac{Zn_e^2}{T^{3/2}\left(1-n_e/n_{crit}\right)^{1/2}}. \tag{27}$$

The absorption due to inverse bremsstrahlung is more effective for high Z, low temperature, and high density plasmas.

Stimulated Raman scattering (SRS) / Stimulated Brillouin scattering (SBS)

When a large amplitude of light wave incidents and excites density fluctuation in plasma, this incident wave, scattered lights, exited plasma wave and exited ion acoustic waves could couple each other. Under the frequency and wave number matching conditions, part of energy in the incident wave is scattered and deposited into the high frequency electron plasma wave. This plasma wave can have a high phase velocity (~ c) and produce energetic electrons when it damps (SRS). Nature of ion wave is the same as the electron plasma wave except for the low frequency (SBS). This acoustic wave can drive perturbations in the plasma density and induce instabilities such as filamentation.

2.2. FAST ELECTRON TRANSPORTS

2.2.1. Electron beam separation from the ambient plasma

Electrons which pick up energies from the laser can escape from the plasma only when their kinetic energies are greater than potential energy arisen by charge separation. When N electrons with energy of $\varepsilon_p = (\gamma - 1) m_e c^2$ separate from the plasma with diameter d, the following condition should be satisfied for the complete detachment [41]

$$\varepsilon_p N > (Ne)^2 / l > (Ne)^2 / d \tag{28}$$

where l is the separation distance and we assume $l << d$. The l.h.s. is the total kinetic energy of N electrons and the central term represents to the potential energy stored in the electric field created by charge separations. Considering the classical electron radius $r_e = e^2 / m_e c^2$ *, l.h.s and r.h.s of Eq. (28) can be rewritten as

$$\gamma - 1 > N r_e / d \,. \tag{29}$$

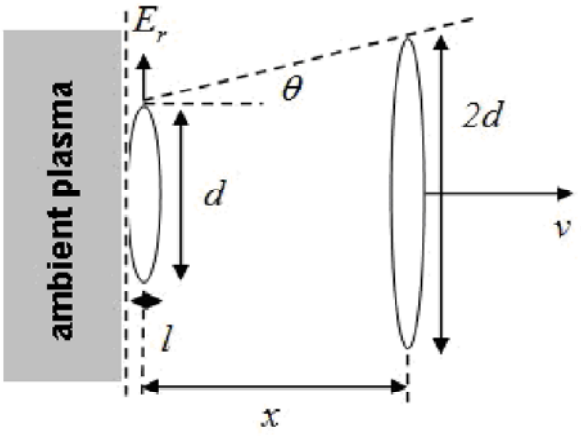

Figure 4. Electron bunch separation from the ambient plasma. The shape of electron bunch is assumed as pancake-like ($d >> l$).

* The classical electron radius is $2.8179402894 \times 10^{-15}$ m.

We note that d is about laser spot size and r_e/d is about order of 10^{-10}. Thus, even for a few MeV electrons, only a few nano coulomb of charges are allowed to leave the interaction regions.

For the highly relativistic electrons, for example $\gamma \sim 10$, $N \sim 10^{10}$, charge separation is not a serious consideration at the central part of laser focused plasma, $d > 3$ μm [42]. However, it would be a very serious problem for lower energy and higher density electrons. At around the laser intensity of $\sim 10^{19}$ W/cm^2 and electron density of $\sim 10^{21}$ cm^{-3}, typical parameters would be $\gamma \sim$ 2-3, $N \sim 10^{13}$ [33]. For this case, d should be an order of millimeter or larger, which is hardly met by the experimental conditions. Therefore those electrons cannot leave ambient plasma without charge neutralization.

A separated electron bunch acquires an angular divergence due to the Coulomb repulsion (See Figure 4). The radial electric field can be estimated from the Poisson's equation,

$$E_r = \pi e\, dn \tag{30}$$

where n is an electron density. Now set Δt as a time for the bunch diameter increasing twice and x as a distance the bunch propagates in Δt, then

$$\Delta t = \frac{x}{v} = \frac{x}{c} \cdot \frac{\gamma}{\sqrt{1-\gamma^2}}, \tag{31}$$

$$d \sim \frac{eE_r}{m_e} \Delta t^2 . \tag{32}$$

Therefore, the initial divergence of electron beam can be estimated by the following

$$\theta \sim \frac{d}{2x} \sim \sqrt{\frac{Nr_c}{l} \cdot \frac{\gamma^2}{\gamma^2 - 1}} . \tag{33}$$

2.2.2. Return current

Although the fast electrons are accelerated by collisonless processes, their distribution could be considered approximately Maxwellian [43, 44]. The current carried by these fast electrons is given by [45]

$$I_{fast} = \varepsilon_{laser} / \tau_{laser} / (1.5\, T_e) \tag{34}$$

where ε_{laser} is absorbed laser energy [J], τ_{laser} is laser pulse duration [sec], and T_e is the electron temperature [eV]. For the experiments in the thesis, typically ε_{laser} ~ 100 mJ, τ_{laser} ~ 40 fs, and T_e ~ 500 keV, so the current by hot electron beam I_{fast} is ~ 5 MA. This value is much over the Alfvén current, which defines the upper limit of a current consisting of charged particle [46]. Alfvén pointed out that electrons outside of a volume of electron beam carrying a certain current should be deflected by the self-generated magnetic fields. The current limit is given by

$$I_A = 1.7 \times 10^4 \beta\lambda = 30\,\text{kA} \quad \text{for} \quad \gamma = 2. \tag{35}$$

Hence, to maintain the fast electron stream, it must be neutralized by return current. The characteristic time of charge neutralization τ_c is dependant on the plasma frequency of cold electrons ω_p, and the collision frequency of cold electrons ν_{ep}. In the collisional limit $\nu_{ep} > \omega_p$, the continuity equation can be written as

$$en / \tau_c \sim j_{fast} / l = \sigma E / l \tag{36}$$

where j_{fast} is the drift current by the self consist electric field of the beam $E \sim 4\pi enl$, and $\sigma = ne^2 / m_e \nu_{ep}$ is a conductivity. From it, $\tau_c \sim \nu_{ep} / \omega_p^2$ is obtained. At the other limit, for the collisonless case $\omega_p > \nu_{ep}$, electric field can excite plasma waves. Therefore, the damping time of this plasma oscillation $\tau_c \sim 1/\nu_{ep}$ will determine current neutralization time. An easy interpolation results in $\tau_c \approx 1/\nu_{ep} + \nu_{ep} / \omega_p^2$. Because of a large number of electrons in metal, this time is typically shorter than 1 fs.

The magnitude of the electrostatic field by the return current can be evaluated from the condition $j_{fast} + j_{rc} \approx 0$,

$$E_{rc} \approx j_{rc}/\sigma = envl/\sigma \tag{37}$$

and the magnitude of magnetic field is given by the Faraday's law;

$$B_{rc} \sim \tau c E_{rc}/d \approx enlc/d\sigma \tag{38}$$

where $\tau = l/v$ is the duration of electron bunch. It is clear that the electric field generated in the conductor [Eq. (37)] is smaller than that in the vacuum [Eq. (30)]. Their ratio is about $d/c\tau_c$.

2.2.3. Two stream and the Weibel instabilities

As discussed in the previous section, a fast electron current and a neutralizing return current result in two-stream configuration. Instabilities arise from such a system can be classified into two classes. The first is the two-stream instability [47], which is longitudinal with a wave vector parallel to the beam. The second is the filamentation instability caused by the Weibel instability [48], which is transverse with wave vector normal to the beam.

Two stream instability

Let's consider a uniform unmagnetized plasma in which ions are stationary and electron velocity is $\mathbf{v}_0 = v_0\hat{\mathbf{z}}$. Setting electric field $\mathbf{E} = \hat{\mathbf{z}}E\exp[i(kz - \omega t)]$, we can start with a set of equation of motions for ions and electrons;

$$M_i n_0 \frac{\partial \mathbf{v}_i}{\partial t} = en_0\mathbf{E}, \tag{39}$$

$$m_e n_0 \left[\frac{\partial \mathbf{v}_e}{\partial t} + (\mathbf{v}_0 \cdot \nabla)\mathbf{v}_e \right] = -en_0\mathbf{E}\,, \tag{40}$$

and a set of continuity equations;

$$\frac{\partial n_i}{\partial t} + n_0 \nabla \cdot \mathbf{v}_i = 0\,, \tag{41}$$

$$\frac{\partial n_e}{\partial t} + n_0 \nabla \cdot \mathbf{v}_e + (\mathbf{v}_0 \cdot \nabla)\mathbf{v}_e = 0\,. \tag{42}$$

By replacing $\partial/\partial t$ and ∇ into $-i\omega$ and ik, velocities and densities are driven from Eq. (39~42);

$$v_i = \frac{ie}{M_i \omega} E\,, \quad v_e = -\frac{ie}{m_e} \frac{E}{\omega - kv_0}\,, \tag{43}$$

$$n_i = \frac{kn_0}{\omega} v_i\,, \quad n_e = \frac{kn_0}{\omega - kv_0} v_e\,. \tag{44}$$

Since the wave for instability is a plasma oscillation having high frequency components, plasma approximation may not be applicable. However, we can still utilize a Poisson's equation;

$$\varepsilon_0 \nabla \cdot \mathbf{E} = e(n_i - n_e)\,. \tag{45}$$

Replace n_i and n_e with Eq. (44), it becomes

$$ik\varepsilon_0 E = e(ien_0 kE)\left[\frac{1}{M_i \omega^2} + \frac{1}{m_e(\omega - kv_0)^2} \right]. \tag{46}$$

From Eq. (46), the dispersion relation is obtained as

$$1 = \omega_p^2 \left[\frac{m_e / M_i}{\omega^2} + \frac{1}{(\omega - kv_0)^2} \right]. \tag{47}$$

For more simplicity, let's introduce dimensionless variables; $\Omega = \omega/\omega_p$, $Z = kv_0/\omega_p$ and set $\Omega = \mathrm{A} + i\Gamma$. Then, the dispersion relation is rewritten as

$$1 = \left[\frac{m_e/M_i}{\Omega^2} + \frac{1}{(\Omega - Z)^2} \right]. \tag{48}$$

Note the imaginary part of Ω represents an exponential growth rate of the instability. For $m_e/M_i << 1$, the maximum growth rate obtained by solving Eq. (48) is given by [47]

$$\Gamma_{\max} \approx \left(\frac{m_e}{M_i} \right)^{1/3}. \tag{49}$$

The Weibel instability

The Weibel instability is driven in an anisotropic plasma [48]. Erich Weibel first pointed out that when the plasma is hotter in one direction than the others, perturbations arise and grow normal to the high temperature axis. In the relativistic electron beam, it causes filamentation and huge magnetic fields of the order of $m_e\omega_p c/e \sim 100(\omega_p/\omega_L)$ MG.

Now let's consider again infinite, unmagnetized and homogeneous plasma with electron density of n_e. I'll introduce P_L and P_T as thermal momentum speared in the *z*-direction and in the *x*-*y* plane respectively. $v_{t,L}$ and $v_{t,T}$ are thermal velocities. Setting $\mathbf{k} = k\hat{\mathbf{z}}$ and using the Vlasov equation with Maxwell equations, the dispersion equation for the Weibel instability is given by [49]

$$D(\mathbf{k}, \omega) = \varepsilon_{yy} - k^2c^2/\omega^2 = 0 \tag{50}$$

where

$$\varepsilon_{yy} = 1 - \frac{\omega_p^2}{\omega^2} + \frac{\omega_p^2}{n_e\omega^2} \int p_y^2 \frac{\mathbf{k} \cdot \partial f/\partial \mathbf{p}}{m_e\omega - \mathbf{k} \cdot \mathbf{p}} d^3p. \tag{51}$$

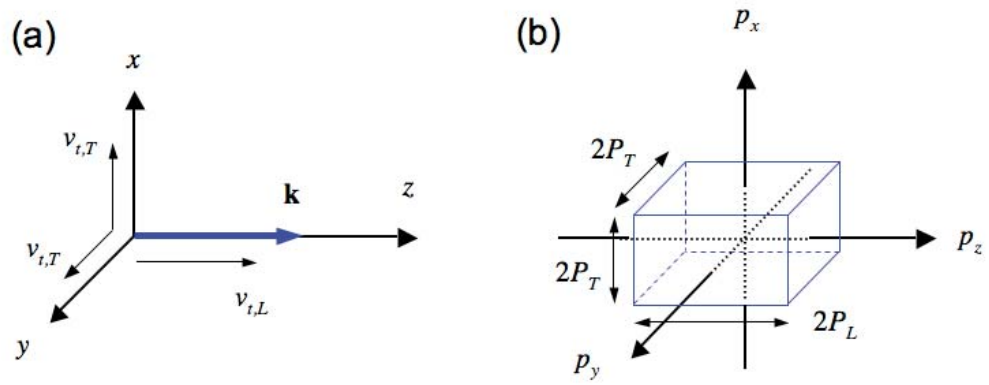

Figure 5. (a) Definition of momentum of electrons and thermal velocities. (b) Water-bag like thermal momentum spread [Eq. (52)] in the phase space.

For simplicity, let's assume some water-bag like distribution function f which is given by [50]

$$f = \frac{n}{(2P_T)^2 2P_L}\left[\Theta(p_x + P_T) - \Theta(p_x - P_T)\right] \times\left[\Theta(p_y + P_T) - \Theta(p_y - P_T)\right]\times\left[\Theta(p_z + P_L) - \Theta(p_z - P_L)\right] \tag{52}$$

where Θ is a step function. This distribution function is easy to be handled analytically and the results from it fit in the Maxwellian calculations, only apart to some factors [50, 51]. By defining dimensionless variables; $\Omega = \omega/\omega_p$, $\mathbf{Z} = \mathbf{k}v_{t,xy}/\omega_p$, $\beta = v_{t,xy}/c$, $\rho = v_{t,z}/v_{t,xy}$, the dispersion equation can be simplified as

$$D(\mathbf{Z},\Omega) = 1 - \Omega^2 + \frac{\mathbf{Z}^2}{\beta^2} - \frac{\mathbf{Z}^2}{3\mathbf{Z}^2\beta^2 - 3\Omega^2} = 0\,. \tag{53}$$

Note that ρ represents anisotropy of the plasma. Putting $\Omega = \mathrm{A} + i\Gamma = (\alpha + i\delta)/\omega_p$, the growth rate can be calculated from the dispersion equation [50]

$$\Gamma = \frac{1}{\sqrt{2}}\left[-1 - Z^2\left(\rho^2 + \frac{1}{\beta^2}\right) + \sqrt{\left(1 - Z^2\left(\rho^2 - \frac{1}{\beta^2}\right)\right)^2 + \frac{4}{3}Z^2}\right]^{1/2}. \quad (54)$$

We can take a derivative of Eq. (54) with respect to Z and find a solution Z_{max} for an equation $\partial\Gamma / \partial Z = 0$. Putting Z_{max} into Eq. (54) again, the maximum growth rate $\Gamma_{\max}$ can be obtained. At the two limits $\rho \to 0$ and $\rho \to 1/\sqrt{3}$, $\Gamma_{\max}$ are evaluated by [50]

$$\Gamma_{\max}(\rho \sim 0) \sim \frac{\beta}{\sqrt{3}}\left(1 - \rho\sqrt{3 + \beta^2}\right), \quad (55)$$

$$\Gamma_{\max}(\rho \sim 1/\sqrt{3}) \sim \frac{\beta}{9}\left(\frac{1}{\sqrt{3}} - \rho\right). \quad (56)$$

2.3. X-RAY EMISSIONS

2.3.1. Inner-shell radiation

Incidence of a hot electron generated by ultra-intense laser pulse on a multi-electron atom can knock free a core electron. Lost energy of a hot electron is used for a core electron to overcome the binding energy and to supply a kinetic energy to a free electron. Then, the core vacancy will be filled with an electron from the higher level of orbits to minimize the total energy of atom itself. It is done by either radiative or non-radiative processes.

A radiative process is accomplished by the photon emission of a characteristic energy corresponding to an energy difference of initial and final atomic states. Theoretically, the energy level of initial and final states can be treated with hydrogen-like approximation. We can set an effective nuclear charge $Z_{eff} = Z - \sigma_n$ and $Z_{eff} = Z - s_n$ with σ_n and s_n are screen constants. σ_n depends on the quantum number l while s_n depends on also j. Then the energy of inner shell is given by

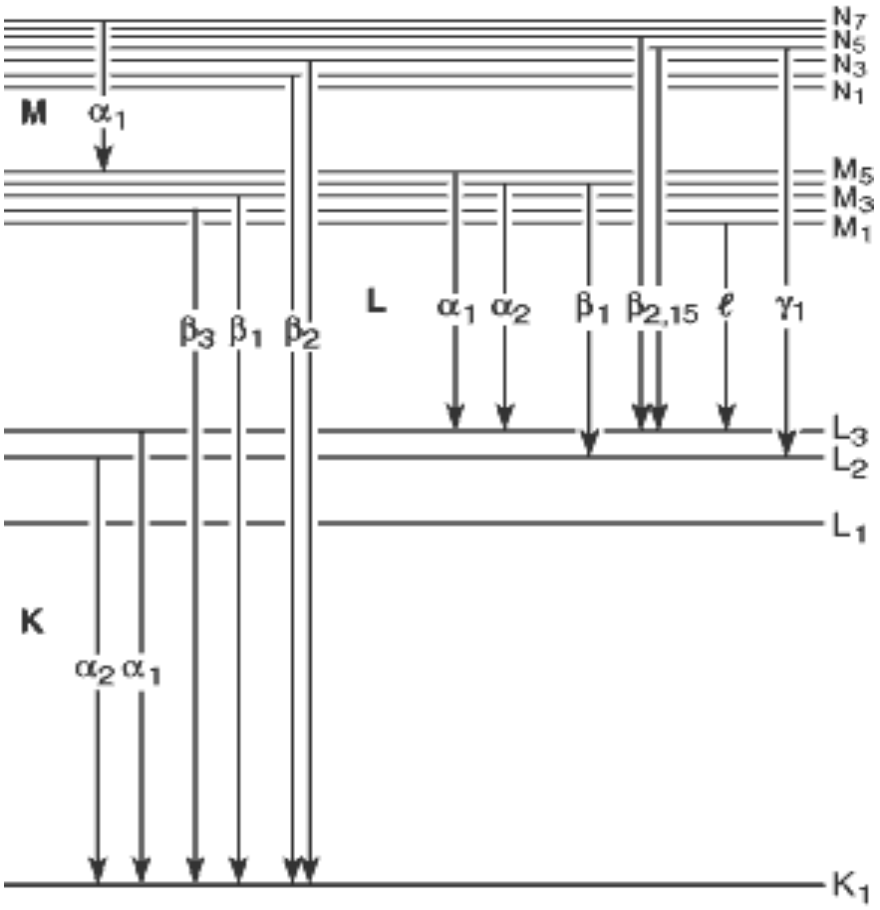

Figure 6. Transition that give rise to the various emission lines [52].

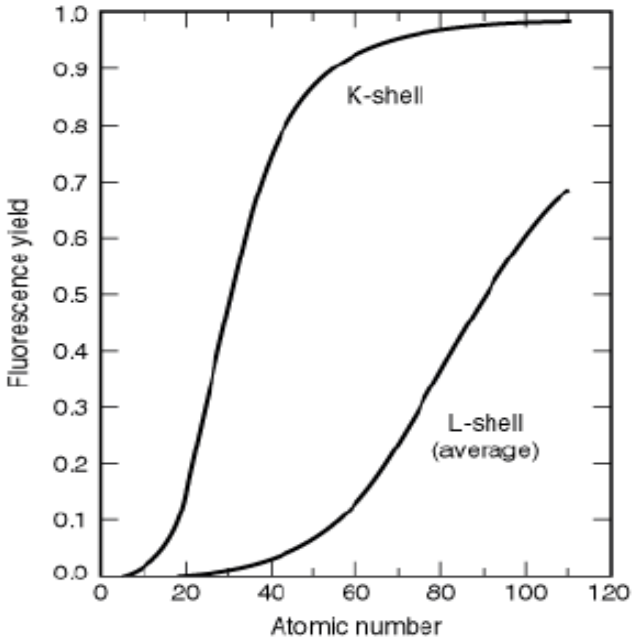

Figure 7. Fluorescence yields for *K*- and *L*-shells for $5 \leq Z \leq 110$. The plotted curve for the *L*-shell represents an average of L_1, L_2, and L_3 effective yields.

$$E_{nlj} = -hcR\frac{(Z-\sigma_n)^2}{n^2} - \frac{hcR\alpha^2(Z-s_n)^4}{n^4}\left(\frac{n}{j+1/2} - \frac{3}{4}\right) \tag{57}$$

where R is the Rydberg constant.* Therefore the energy of x-ray photon energy is determined by the initial and final state of energy levels. Another fact should be considered is a transition rule for the electron - hole. It is basically identical to the selection rule for one electron atom, i.e. Δn = arbitrary, $\Delta l = \pm 1$, $\Delta j = 0, \pm 1$. For example, *K*-shell radiations, i.e. $K\alpha_1$ and $K\alpha_2$ lines are given by the transitions of $2P_{3/2} \rightarrow 1S_{1/2}$ and $2P_{1/2} \rightarrow 1S_{1/2}$ (See Figure 6). Because of the population ratio of $2P_{3/2}$ and $2P_{1/2}$, the radiation intensity ratio of $K\alpha_1$ and $K\alpha_2$ is also determined as 2:1.

One noticeable process is Auger process in which one electron makes a transition to the core vacancy, while a second electron of characteristic energy is emitted.

* Rydberg constant is 10973731.534 m^{-1}

However, the second electron is not necessarily emitted from the same shell. Auger process is non-radiative process competing with fluorescence for the *K*-shell holes. The probability for the *K*-shell hole to be filled by a radiative process is shown in the Figure 7 [52].

2.3.2. Bremsstrahlung

In addition to line emissions, an additional continuous radiation is also observed in collisions of electrons with matter. When a charge is decelerated in collision with free or bounded atoms, a part of energy loss can be transferred into electromagnetic radiations. This phenomenon was named bremsstrahlung by Arnold Sommerfeld.

The radiation energy *S* by an electron per unit time is governed by its acceleration **w** [53]

$$S = \frac{2}{3}\frac{e^2}{c^3}\mathbf{w}^2, \tag{58}$$

and the total radiation energy over all time ΔE can be written as

$$\Delta E = \int_{-\infty}^{\infty} S dt = \int_{-\infty}^{\infty} S_\nu d\nu \tag{59}$$

where S_ν is the radiant energy per unit frequency interval emitted with a frequency ν, which is given by

$$S_\nu = \frac{16\pi^2}{3}\frac{e^2}{c^3} w_\nu^2 \tag{60}$$

where w_ν is the Fourier component of **w**.

Now let's introduce an impact parameter of an electron-ion collision ρ. Then the energy radiated in the frequency interval ν and $\nu + d\nu$ is

$$dq_\nu = d\nu \int_0^{\infty} S_\nu 2\pi\rho d\rho . \tag{61}$$

Using the acceleration vector given in the Landau and Lifshitz's book [54], it becomes

$$dq_v = \frac{32\pi^2}{3\sqrt{3}} \frac{Z^2 e^6}{m_e^2 c^3 u^2} d\nu \tag{62}$$

at the high frequency range ($\nu >> m_e u^3 / 2\pi Ze^2$), where we are mostly interested.

Now, we calculate the energy emitted by electrons having velocity from u and $u + du$ per unit volume per unit time in the frequency range ν to $\nu + d\nu$. Setting N_+ is the positive ion density with charge Ze and N_e electron density, the energy is given by [53]

$$N_+ N_e f(u) du \; u \; dq_v(u) \tag{63}$$

where $f(u)du = 4\pi (m_e / 2\pi kT)^{3/2} \exp(m_e u^2 / 2kT) u^2 du$ is a Maxwellian velocity distribution. Integrating Eq. (63) over velocity from u_{min} to infinity, spectral emission coefficient due to bremsstrahlung is found to be

$$J_v dv = \frac{32\pi}{3} \left(\frac{2\pi}{3 m_e kT} \right)^{1/2} \frac{Z^2 e^6}{m_e c^3} N_+ N_e e^{-h\nu / kT} dv \,. \tag{64}$$

For our experiment, this exponential bremsstrahlung spectrum was used to calculated electron temperature. X-ray energy deposited in the NaI(Tl) detector is proportional to $\int E_\gamma T(E_\gamma) J_{E_\gamma} dE_\gamma$, where E_γ is x-ray photon energy $h\nu$, $T(E_\gamma)$ is the transmission of cut-off filter (See chapter 3.3.6) and $J_{E\gamma}$ is a rewritten function of Eq. (64) in terms of E_γ. Varying an initial temperature, x-ray yield data can be fitted using a least square analysis and the hot electron temperature can be evaluated.

2.4. TRANSITION RADIATIONS

Transition radiation, which was first described by V. Ginzburg and I. Frank [26], occurs when a propagating charged particle encounters a change in dielectric constants. A motion of charged particle in the middle of uniform medium has a certain field

characterization. In different media, the field characteristics will be different, even though particle motion is the same. Hence, at the boundary of two media, some reorganization process in the electromagnetic field is necessary, i.e. two different field characteristics induce dipole moments. This field shaking off is shown as transition radiation.

Recently, in order to study fast electrons from the laser solid density plasma interactions, measuring transition radiation is considered as a very useful technique, which provides lots of information. In this section, I introduce theoretical calculation procedures for these radiations from our experiments.

Setting the target medium and electron motion as presented in the Figure 8, let's begin with a set of Maxwell's equations;

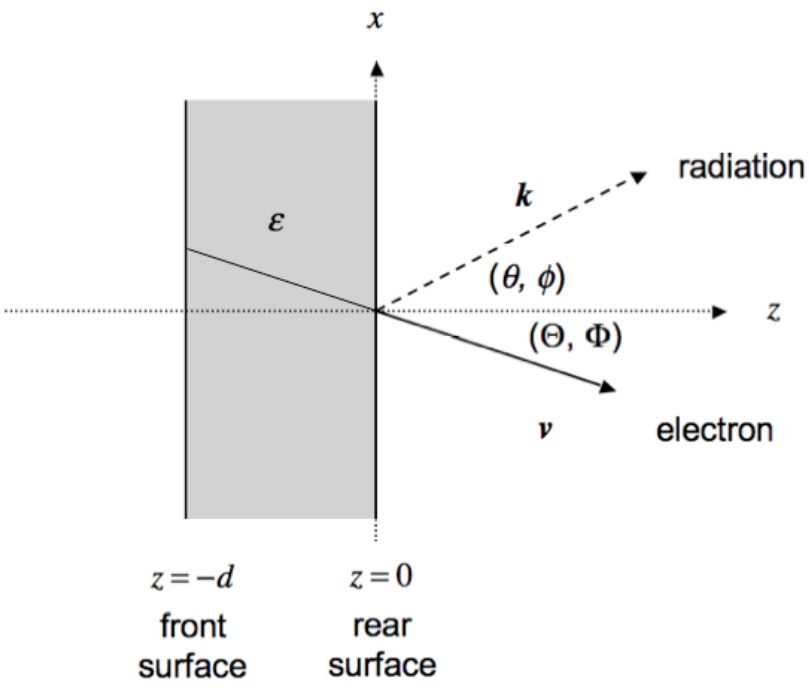

Figure 8. Two dimensional configuration of the calculation for transition radiations.

$$\nabla^2\mathbf{A}-\frac{\hat{\varepsilon}}{c^2}\frac{\partial^2}{\partial t^2}\mathbf{A}=-\frac{4\pi}{c}e\sum_{i=1}^{N}\mathbf{v}_i\delta\left[z-u_i(t-t_i)\right]\times\delta\left[\boldsymbol{\rho}-\boldsymbol{\rho}_i-\mathbf{w}_i(t-t_i)\right], \tag{65}$$

$$\hat{\varepsilon}\left(\nabla^2\varphi-\frac{\hat{\varepsilon}}{c^2}\frac{\partial^2}{\partial t^2}\varphi\right)=-4\pi e\sum_{i=1}^{N}\mathbf{v}_i\delta\left[z-u_i(t-t_i)\right]\times\delta\left[\boldsymbol{\rho}-\boldsymbol{\rho}_i-\mathbf{w}_i(t-t_i)\right] \tag{66}$$

where $\mathbf{A}$ and φ are the vector and scalar potentials of the electromagnetic field, t_i is the time when the i-th electron leaves the target rear surface, $\mathbf{v}_i = (\mathbf{w}_i, \mathrm{u}_i)$ is the velocity of the i-th electron, $\boldsymbol{\rho}_i$ is the tangential coordinate of i-th electron at t_i, $\varepsilon(\omega)$ is the dielectric function of the target and $\hat{\varepsilon}$ is an operator defined by $\hat{\varepsilon}\exp(-i\omega t)=\varepsilon(\omega)\exp(-i\omega t)$. Magnetic permeability is set to unity. Since the radiation field is transverse, i.e. $k^2=\varepsilon\omega^2/c^2$, the Fourier component of it in the vacuum ($z > 0$) can be written as [30, 55]

$$\mathrm{E}^r(\mathbf{k},\omega)=\mathrm{E}_z^r\left[\hat{\mathbf{z}}-(\eta/q^2)\mathbf{q}\right]\delta\left(k^2-\varepsilon\omega^2/c^2\right). \tag{67}$$

Following M. L. Ter-Mikaelian's method [55], the amplitude of field E_z^r is evaluated as

$$\mathrm{E}_z^r=\sum_{i=1}^{N}\mathrm{E}_i(\mathbf{w}_i,u_i)e^{i\omega t_i-i\mathbf{q}_i\cdot\boldsymbol{\rho}_i} \tag{68}$$

where

$$\begin{aligned}\mathrm{E}_i=&-i\frac{4(2\pi)^2e|\eta_2|}{(|\eta_1|+\varepsilon|\eta_2|)u_i}\\&\times\left\{-\frac{\left(q^2-\varepsilon\omega\mathbf{q}\cdot\mathbf{w}_i/c^2\right)\left(1+|\eta_1|/\kappa_i\right)}{q^2+\kappa_i^2-\varepsilon(\omega/c)^2}+\frac{\left(q^2-\omega\mathbf{q}\cdot\mathbf{w}_i/c^2\right)\left(\varepsilon+|\eta_1|/\kappa_i\right)}{q^2+\kappa_i^2-\varepsilon(\omega/c)^2}\right\}\end{aligned} \tag{69}$$

and

$$\eta_1=-\sqrt{\varepsilon\omega^2/c^2-q^2}\ ,\quad \eta_2=-\sqrt{\omega^2/c^2-q^2}\ ,\quad \kappa_i=(\omega-\mathbf{q}\cdot\mathbf{w}_i)/u_i\ . \tag{70}$$

When we assume a good conductor $|\varepsilon|\to\infty$, Eq. (69) can be rewritten as

$$\mathrm{E}_i = -i\frac{4(2\pi)^2 e\beta_i}{c}\left[\frac{\sin\theta\cos\Theta_i\left[\sin\theta-\beta_i\sin\theta\cos(\phi-\Phi_i)\right]}{\left(1-\beta_i\sin\theta\sin\Theta_i\cos(\phi-\Phi_i)\right)^2-\beta_i^2\cos^2\theta\cos^2\Theta_i}\right]. \qquad (71)$$

β_i and (Θ_i, Φ_i) are the speed (in the unit of c) and direction of the moving particle, respectively. (θ, ϕ) is the observation direction (See Figure 8). Then the energy spectrum of this transition radiation is given by

$$\frac{d^2\mathcal{E}}{d\omega d\Omega} = \frac{c}{4(2\pi)^6\sin^2\theta}\left|\sum_{i=1}^{N}\mathrm{E}_i(\mathbf{w}_i,u_i)e^{i\omega t_i - i\mathbf{q}_i\cdot\boldsymbol{\rho}_i}\right|^2. \qquad (72)$$

This can be separated into two parts. The first is the summation of the radiation spectra from individual particles, namely, incoherent transition radiation (ITR)

$$\frac{d^2\mathcal{E}_{ITR}}{d\omega d\Omega} = \frac{c}{4(2\pi)^6\sin^2\theta}\left|\sum_{i=1}^{N}\mathrm{E}_i(\mathbf{w}_i,u_i)\right|^2. \qquad (73)$$

Second part is determined by the interference between the radiations from different particles, called coherent transition radiation (CTR)

$$\frac{d^2\mathcal{E}_{CTR}}{d\omega d\Omega} = \frac{c}{4(2\pi)^6\sin^2\theta}\sum_{i\neq j}^{N}\mathrm{E}_i(\mathbf{w}_i,u_i)\mathrm{E}_j^*(\mathbf{w}_j,u_j)e^{i\omega(t_i-t_j)-i\mathbf{q}_i\cdot(\boldsymbol{\rho}_i-\boldsymbol{\rho}_j)}. \qquad (74)$$

2.4.1. Incoherent transition radiation (ITR)

Eq. (73) shows ITR spectrum is dependent on the velocity of each particle. Fast electrons from the laser solid interaction can be described with a velocity distribution function, which is defined as ensemble average of each velocity distribution

$$f_{\mathbf{v}}(\mathbf{v}) = \left\langle\frac{1}{N}\sum_{i=1}^{N}\delta(\mathbf{v}-\mathbf{v}_i)\right\rangle. \qquad (75)$$

Then, ITR spectrum becomes [30]

$$\frac{d^2\mathcal{E}_{ITR}}{d\omega d\Omega} = \frac{Ne^2}{\pi c^2}\int d\mathbf{v}\ f(\mathbf{v})\frac{\beta^2\cos^2\Theta\left[\sin\theta-\beta\sin\Theta\cos(\phi-\Phi)\right]^2}{\left[\left(1-\beta\sin\theta\sin\Theta\cos(\phi-\Phi)\right)^2-\beta^2\cos^2\theta\cos^2\Theta\right]^2} \quad (76)$$

We note that it is not a function of the radiation frequency. It means that the ITR spectrum is flat in the spectral range where the condition $|\varepsilon| >> 1$ is satisfied (good conductor assumption). One more thing that should be mentioned is that the radiation intensity is proportional to the number of particle *N*. Considering ITR is the summation of the radiation from individual particle, it is quite obvious result.

2.4.2. Coherent transition radiation (CTR)

CTR spectrum given by Eq. (74) indicates that it depends not only the particle velocity but also relative particle configurations to each other, such as temporal and spatial coordinates. Thus, the particle distribution function used in the previous section needs to be modified as the following;

$$f_{\mathrm{v}}(\tau,\boldsymbol{\rho},\mathbf{v}) = \left\langle \frac{1}{N}\sum_{i=1}^{N}\delta(\tau-t_i)\delta(\boldsymbol{\rho}-\boldsymbol{\rho}_i)\delta(\mathbf{w}-\mathbf{w}_i)\delta(u-u_i)\right\rangle. \quad (77)$$

Then, the CTR spectrum becomes [30]

$$\frac{d^2\mathcal{E}_{CTR}}{d\omega d\Omega} = \frac{N(N-1)e^2}{\pi c^2}\left|\int d\tau d\boldsymbol{\rho} d\mathbf{v}\ f(\tau,\boldsymbol{\rho},\mathbf{v})e^{i\omega\tau-i\mathbf{q}\cdot\boldsymbol{\rho}}\right. \times\left.\frac{\beta\cos\Theta\left[\sin\theta-\beta\sin\Theta\cos(\phi-\Phi)\right]}{\left[\left(1-\beta\sin\theta\sin\Theta\cos(\phi-\Phi)\right)^2-\beta^2\cos^2\theta\cos^2\Theta\right]}\right|^2. \quad (78)$$

It is very complex to calculate this directly. Nevertheless, it is clear that this radiation is proportional to the square of particle number N^2, and has frequency dependence. Therefore, when we consider a large number of electrons generated from the laser-solid interaction, a much brighter CTR emission can be expected comparing to ITR at a certain spectral range.

In general, we can have some reasonable assumptions for further calculations. First of all, Maxwellian velocity distribution of electron and one-dimensional moving of particles is assumed;

$$f_{\mathrm{v}}(\beta)=\frac{\beta}{T(1-\beta^2)^{3/2}}\exp\left[-\frac{1}{T}\left(\frac{1}{\sqrt{1-\beta^2}}-1\right)\right]. \tag{79}$$

More simple but realistic case would be electrons move along z-axis, target normal direction. In this case, Eq. (78) can be rewritten as

$$\begin{aligned}\frac{d^2\mathcal{E}_{CTR}}{d\omega d\Omega}=\frac{N_b^2e^2}{\pi c^2}\sin^2\theta\, e^{-q^2a^2}\Bigg|\int d\tau d\beta e^{i\omega\tau}\frac{\beta}{T\left(1-\beta^2\right)^{3/2}}e^{-\varepsilon/T}\\ \times\sum_{n=1}^{\Lambda}\delta(\tau-\tau_n-t_0/\beta)\frac{\beta\cos\Theta\left(\sin\theta-\beta\sin\Theta\right)}{\left[\left(1-\beta\sin\theta\sin\Theta\right)^2-\beta^2\cos^2\theta\cos^2\Theta\right]}\Bigg|^2.\end{aligned} \tag{80}$$

After integrating over β, remaining part in the integration is shown as the form of Fourier transform of a certain function;

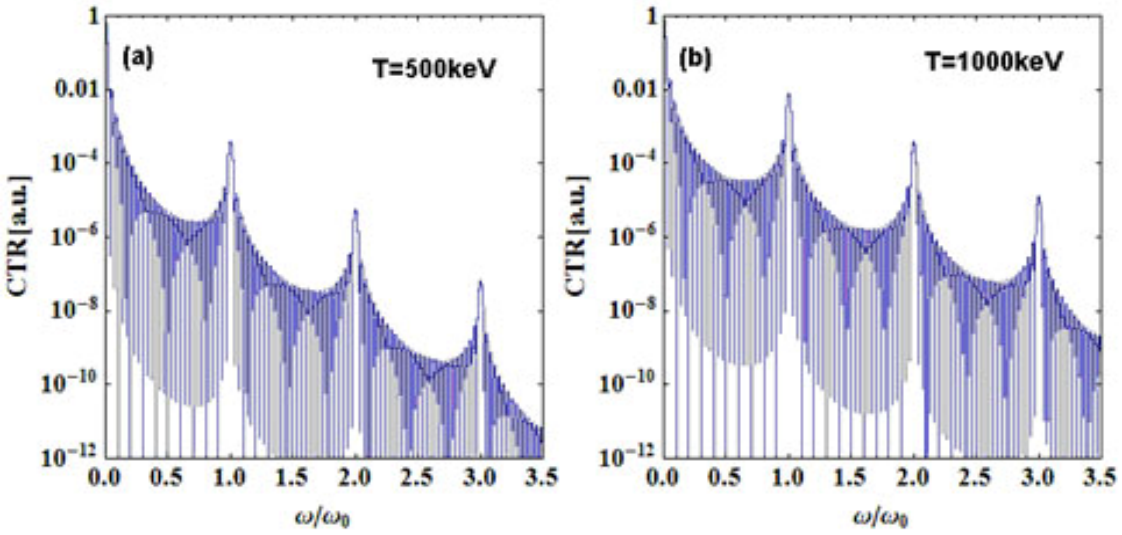

Figure 9. Calculated CTR spectra using Eq. (80). $\Theta = 0°$, $\Lambda = 30$, $d = 10$ μm, $\theta = 45°$, (a) $T = 500$ keV and (b) $T = 1$ MeV

$$\frac{d^2\mathcal{E}_{CTR}}{d\omega d\Omega} = \frac{N_b^2 e^2}{\pi c^2 T^2 t_0^2} \sin^2\theta \, e^{-q^2 a^2} \left|\tilde{g}(\omega,\theta,T,d)\right|^2 \tag{81}$$

where

$$g(\tau,\theta,T,d) = \sum_{n=1}^{\Lambda} \frac{\left(t_0/(\tau-\tau_0)\right)^4 \exp\left[-\frac{1}{T}\left(\frac{1}{\sqrt{1-\left(t_0/(\tau-\tau_0)\right)^2}}-1\right)\right]}{\left[1-\left(t_0/(\tau-\tau_0)\right)^2\cos^2\theta\right]\left[1-\left(t_0/(\tau-\tau_0)\right)^2\right]^{3/2}}. \tag{82}$$

The sequence of spikes in the function g by the term of $1/(\tau-\tau_0)$ infers that the corresponding CTR also have peaks in the spectrum.

It is obvious that the CTR spectrum is also dependent on electron temperature T and target thickness d. Because of the velocity dispersion, the more electron bunches propagate, the more it broadens in the time and adjacent bunches overlap each other. It is clearly observed from the number of electrons passing though a target rear side at time τ, which is given by [30]

$$N(\tau) = \frac{N}{\Lambda T}\sum_{n=1}^{\Lambda} \frac{\left(t_0/(\tau-\tau_0)\right)\exp\left[-\frac{1}{T}\left(\frac{1}{\sqrt{1-\left(t_0/(\tau-\tau_0)\right)^2}}-1\right)\right]}{t_0\left[1-\left(t_0/(\tau-\tau_0)\right)^2\right]^{3/2}} \tag{83}$$

Note that this current is very similar form to the g factor in the Eq. (82). The oscillating amplitudes of a current with specific frequencies determine the peak value at corresponding wavelengths in the CTR spectrum. Figure 9 and Figure 10 were created using Mathematica code presented in the Appendix B.

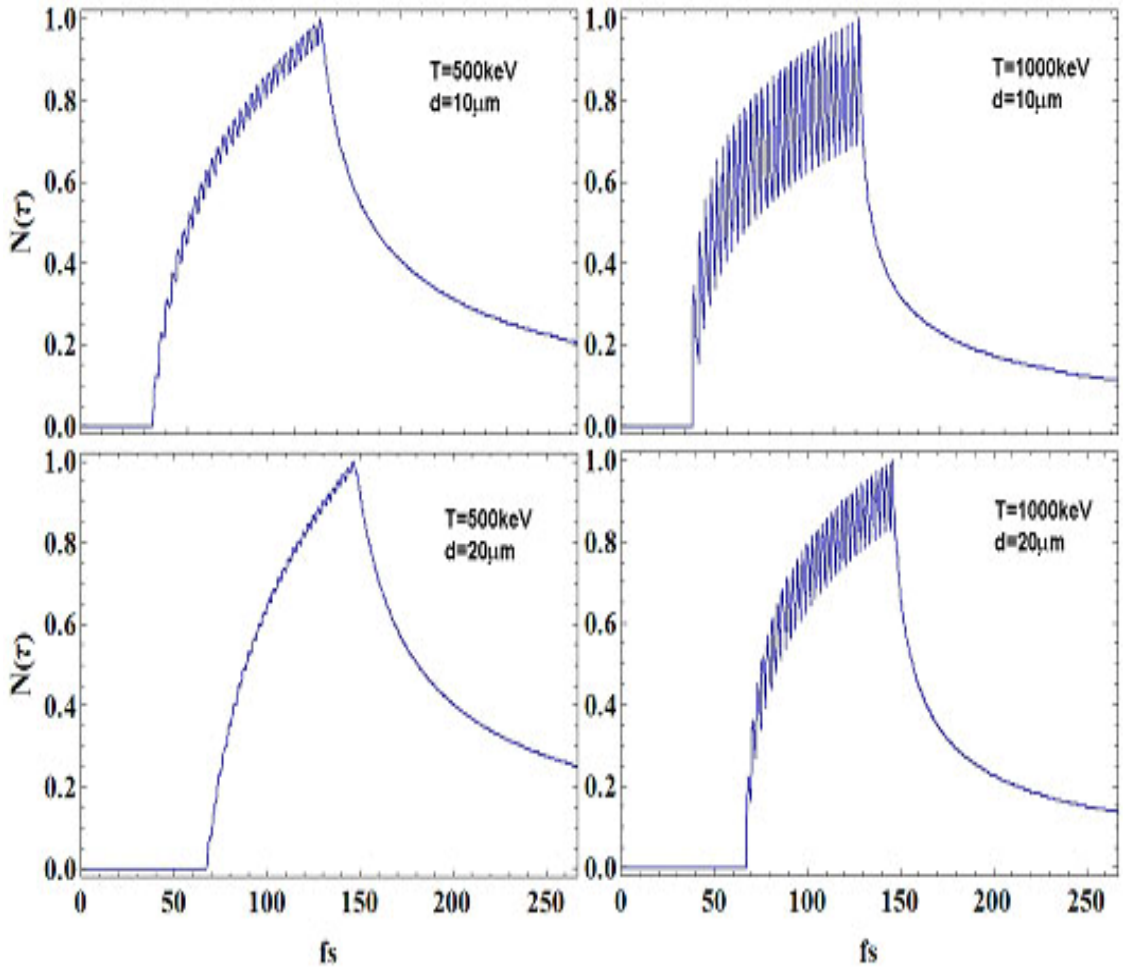

Figure 10. Calculated current at target rear side using Eq. (83). $\Theta = 0°$, $\Lambda = 30$, (left) $T = 500$ keV and (right) $T = 1$ MeV, (top) $d = 10$ μm and (bottom) $d = 20$ μm. Two currents on the upper line are corresponding to CTR spectra in Figure 9.

CHAPTER 3. EXPERIMENTAL APPARATUS

This chapter is for experimental hard wares in the THOR laser room and target area. This chapter consists of three parts. First section describes the primary tool, the Texas high-intensity optical research (THOR) laser. The second is for micro-structured laser targets with various shapes. Finally, the last is for the clamshell target chamber and various diagnostics installed inside and outside of the chamber.

3.1. TEXAS HIGH INTENSITY OPTICAL RESEARCH (THOR) LASER

Two major approaches for developing high-power laser system is keeping the laser pulse short and amplifying pulse energy high. Currently these two requirements are mostly achieved by utilizing Ti:sapphire crystal as a laser medium and chirped pulse amplification (CPA) technique. The state of the art Ti:sapphire systems generate pulses as short as a few femtosecond (a couple of optical cycles) and/or with energy of a hundred of joules.

Since Ti:sapphire was introduced as a laser material in late 80's, its unique properties such as a relatively high gain cross section and an extremely large tuning bandwidth (700 nm ~ 1100 nm) make it the most versatile laser medium for the short pulse laser [56]. In the chapter 3.1.1, the detailed feature for the short pulse generation, Kerr lens mode locking in the Ti:sapphire oscillator is described.

CPA invented by Strickland and Mourou in 1985 was a revolutionary invention for the amplifying laser pulse energy [57]. The biggest limitation of amplifying laser pulse energy is keeping the peak intensity of beam below a damage threshold of optic materials. Before the advent of CPA, this criterion could be achieved only increasing size of beam. However, CPA technique expands pulses in the time domain instead the spatial domain. Detailed process of CPA for the THOR laser is described in the chapter

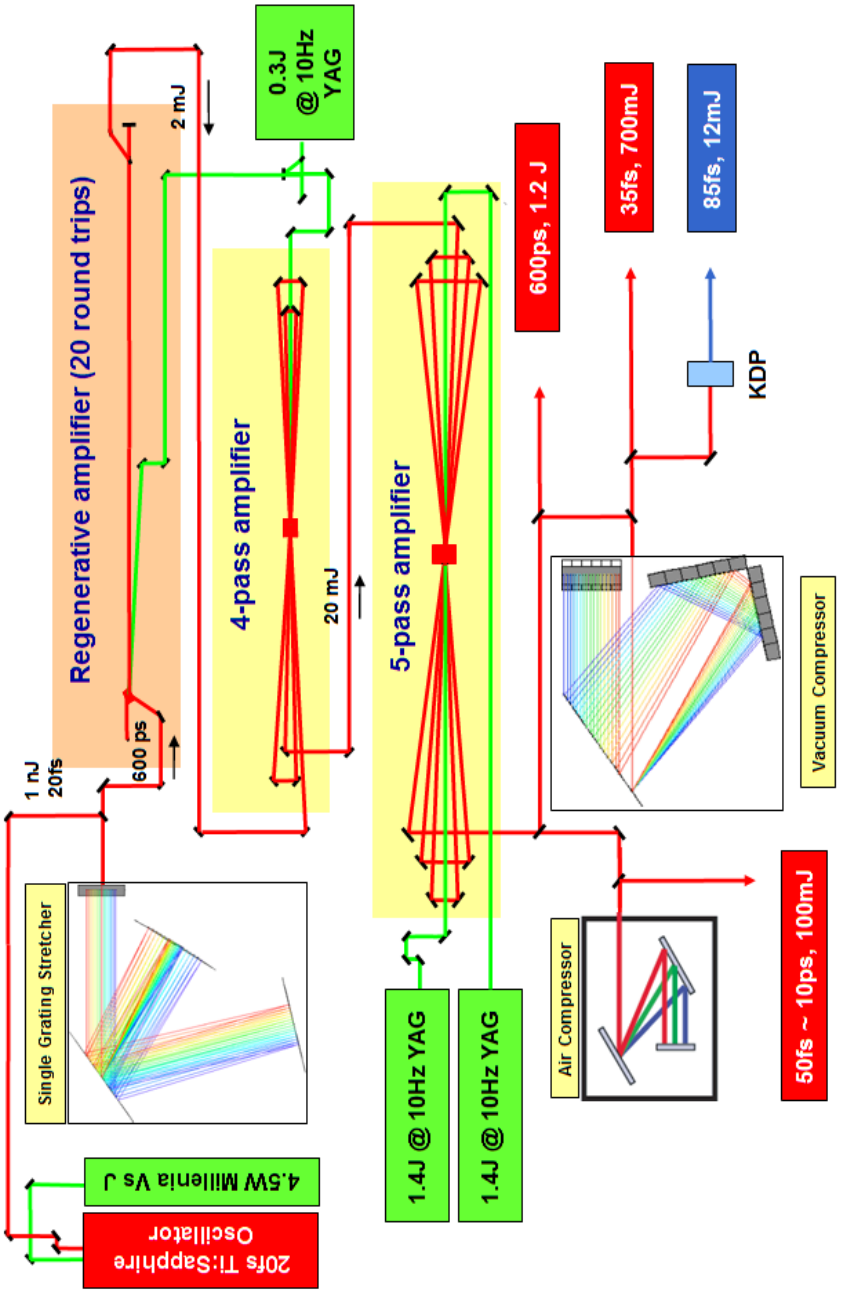

Figure 11. Layout of the THOR laser. The THOR is a short pulse Ti:sapphire laser system employing a novel technique of chirped pulse amplification.

3.1.2.

The THOR laser, on which experiments in this thesis were performed, utilizes both Ti:sapphire as a gain material and a chirped pulse amplification technique. The front end is Ti:sapphire oscillator generating 20 fs, 1 nJ pulses with a repetition rate of 75 MHz. After reducing the repetition rate of 10Hz, pulses are stretched to 600 ps and through three amplification stages, energy boosted up to 1.2 J per pulse. This pulse is compressed in the vacuum and finally up to 700 mJ of laser energy can be delivered on target in 35 fs. Peak intensity of the beam focused by an off-axis parabola is achieved up to 2×10^{19} W/cm^2.

3.1.1. Kerr lens mode-locking (KLM) / Ti:sapphire oscillator

The optical Kerr effect is a change of refractive index of material by the strength of electric field [58];

$$n = n_0 + n_2 I \tag{84}$$

When the laser intensity becomes high enough, this intensity-dependent index of refraction (n_2) leads a modulation of spatial beam profile. For a Gaussian beam, the

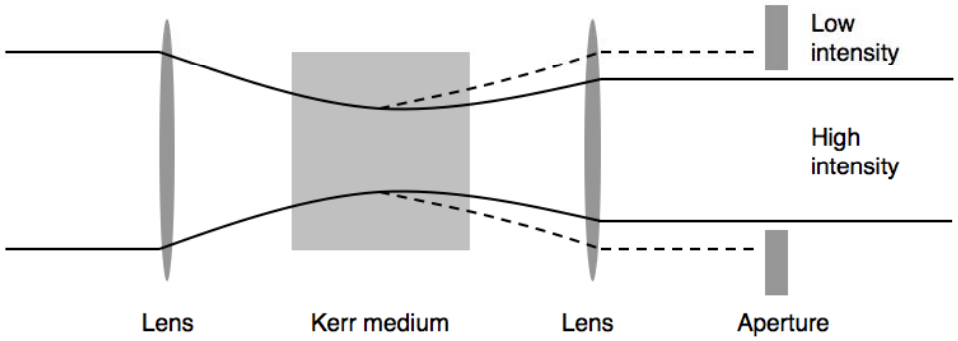

Figure 12. Self-focusing inside the Kerr medium favors to be build up in phase whereas low intensity CW modes are suppressed.

Kerr effect focuses it toward the beam center, namely Kerr lensing. With a proper aperture which allows the higher transmission for intense beam, the Kerr effects can provide a fast saturation absorber and very simple means for ultra-short pulse generation. This technique is named Kerr lens mode-locking (KLM).

For designing and analyzing KLM oscillator, it is convenient to introduce a parameter δ, called Kerr lens sensitivity. It represents the small signal relative a spot size variation and is defined as [59]

$$\delta = \left(\frac{1}{2w} \frac{dw}{dp} \right)_{p=0} \tag{85}$$

where w is the mode size and p is normalized laser power with critical power for the Kerr effect.

A typical resonator used for Kerr lens mode-locking of Ti:sapphire ($Ti:Al_2O_3$) crystal pumped by green laser, for example Ar^+ laser or frequency doubled YAG laser, is illustrated in Figure 14 (a). Ti:sapphire has absorption and fluorescence bands around 500 and 800 nm respectively. The wide separation is caused by the strong coupling between the ion and host lattice, and it is also the key of the broad emission spectra which makes Ti:sapphire laser.

The oscillator for the THOR front end is Femtosource Scientific S20 and pumped with Spectra Physics Millennia Vs DPSS laser. The Millennia outputs 4.5 W of green beam, which is focused into the Ti:sapphire crystal of the oscillator. Dispersions from the crystal are compensated by a pair of chirped multi-layer dielectric mirrors. The oscillator generates 20 fs, 8 nJ pulses at a repetition rate of 75 MHz and average power of over 600 mW. Kerr lens sensitivity for this oscillator is calculated and presented in Figure 14 (b). In the region of negative value of δ, the mode size decreases as intensity increases and Kerr lens mode-locking is available. Calculation code is presented in the appendix A.

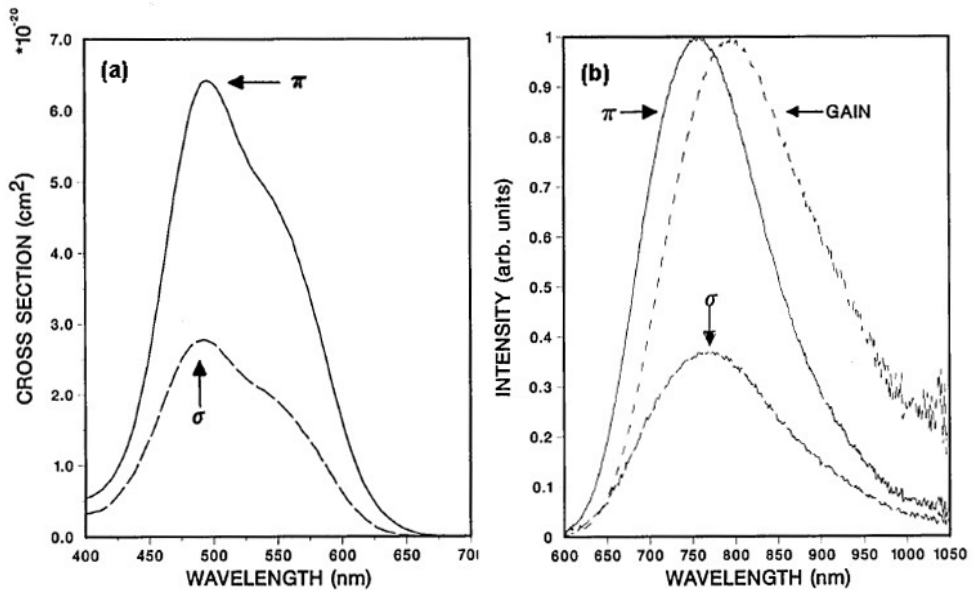

Figure 13. (a) Absorption and (b) fluorescence spectra of the Ti^{3+} ion in Al_2O_3 [56].

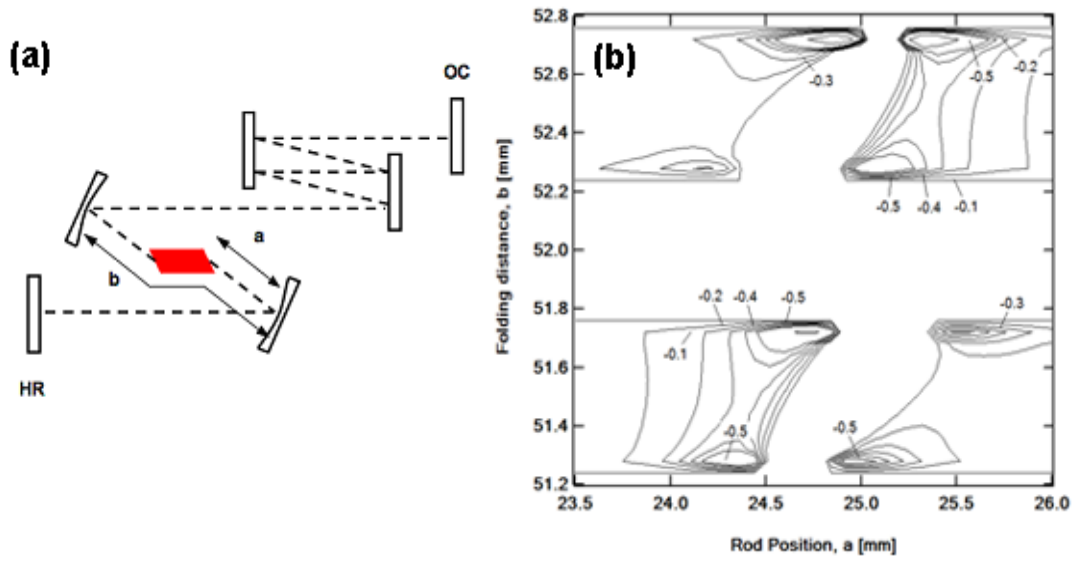

Figure 14. (a) Schematic of the oscillator. Position of the Ti:sapphire crystal from one curved mirror and total length of sub-resonator are denoted by *a* and *b*, respectively. (b) Kerr lens sensitivity for the THOR oscillator.

3.1.2. Chirped pulse amplification (CPA) / Stretcher, amplifiers and compressor

Though novel solid-state gain media developed in 70s and 80s showed promises for high peak power lasers due to their high energy fluence and broad gain bandwidth, amplification of short pulse in this medium raised strong intensity dependent nonlinear effects, such as the optical Kerr effect accounting for serious effects on beam, before its fluence reaches the saturation limit. As mentioned in previous section, this limitation could have been overcome by revolutionary concept of chirped pulse amplification, a major breakthrough of the laser technology in developing high power tabletop system. The concept of CPA is illustrated in Figure 15. Instead of expanding beam size, CPA exploits the inverse relation between time scale and the peak intensity of pulse.

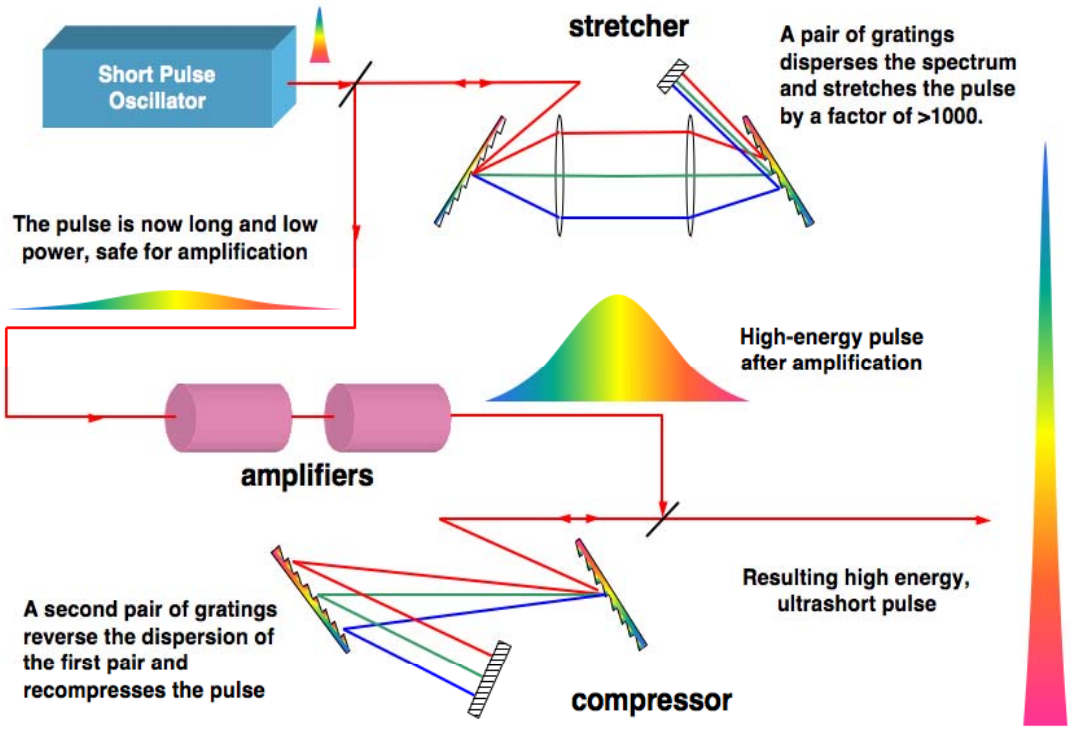

Figure 15. Illustration of chirped pulse amplification.

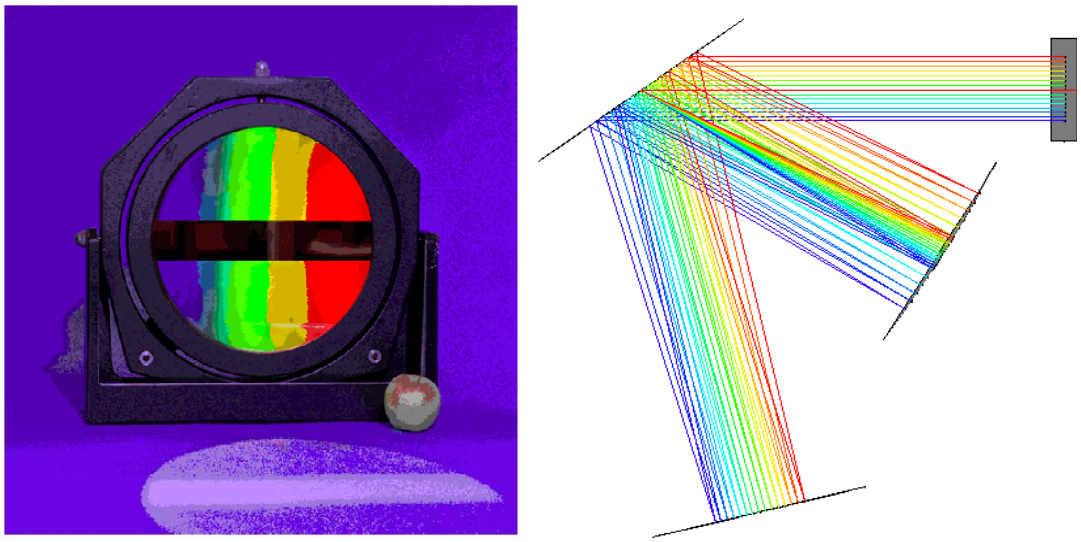

Figure 16. Photograph of 40cm gold coated grating which is similar to that in the THOR laser. Optical ray trace of the stretcher. [60]

Grating stretcher

Low energy ultra short seed pulses generated from mode-locked oscillator are sent through a Faraday rotator and a fast on-off Lasermetrics Pockels cell. Faraday rotator protects the oscillator from back reflections and Pockels cell slices out 10 Hz pulses out of 75 MHz oscillator outputs. Each component is surrounded by two calcite polarizers and provides extinction with the ratio of about 1:1000.

A sliced pulse sent to the grating stretcher and temporally stretched a factor of at least 10^3. Stretcher generally consists of an anti-parallel grating pair and two-lens telescope for 1 to 1 imaging of input and output beams. This configuration let the different frequency components propagate different optical pass lengths, i.e. blue light travels longer distance than red, namely a positive chirp. By controlling the distance and angle between grating pairs precisely, desired amount of dispersion can be added on each frequency component.

For the THOR, instead of using pair of grating, a folded design is utilized using a large flat mirror between two gratings. Stretcher equips a 40 cm wide, 1480 line/mm

diffraction grating fabricated at LLNL. Two-inch mirror strip is placed at the center of the grating to eliminate spherical aberration from off-axis reflection at the spherical mirror, which is replacement of lens to avoid chromatic errors. Telescope consists of a spherical mirror with focal length of 1130 mm, a 30 cm diameter flat mirror and a central mirror strip on the grating. With this configuration, 20 fs pulses generated from the oscillator are stretched approximately 600 ps.

Stretched pulse is sent through a single mode fiber to pre-compensate all dispersions given by the entire laser system. For the shorted pulse length after compression, up to 5^{th} order dispersions from all transmitting optical components such as Ti:sapphire crystals, Pockels cells, polarizers, waveplates, lenses and windows, were calculated and 4^{th} order dispersion is minimized by selecting 4.5 m of Fused-silica fiber [61]. Single mode fiber is served as a good spatial filter too. Pulse out of the fiber passes through a Faraday rotator unit and sent to amplifying stages. A Faraday rotator protects the output of the fiber from intense back reflections or leakage from the regenerative amplifier.

Three amplifying stages

In the THOR system, energy of stretched pulse is boosted in the three amplification stages. Each stage utilizes a Ti:sapphire crystal pumped by *Q*-switched YAG laser that produces frequency double 532 nm pulses. As discussed in previous section, Ti:sapphire has broad emission spectrum that covers from 700 to 1100 nm. Gain cross section around the peak wavelength (2.9×10^{18} cm^2 at 800 nm) is a relatively large, but its fluorescence lifetime is as short as 3.2 μs. Thus, for effective pumping and extraction of energy, another short pulse laser is required to put a large amount of energy in this short time scale.

The first amplification stage is a regenerative (regen) amplification stage consisting of 20 round trips in the resonator. This regen is nothing but a laser cavity

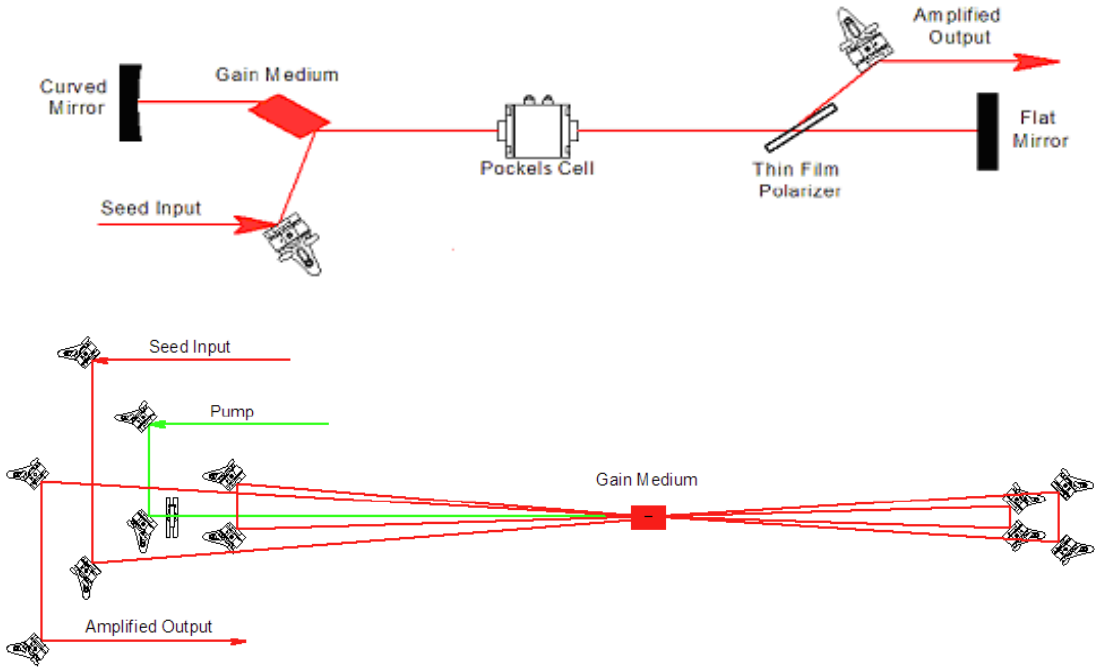

Figure 17. Schematic of (top) regenerative amplifier and (bottom) 4-pass amplifier [60].

equips 5 mm × 10 mm × 10 mm, Brewster cut Ti:sapphire crystal pumped by 532 nm, 45 mJ pulses from BigSky CFR-400 laser. In this cavity, a fast Pockels cell and a polarizer are inserted for optical switching. Once a low energy seed pulse is injected into the cavity, a Medox dual-pulse fast on/off Pockels cell is turned on and traps this pulse in the cavity. After 20 round trips this pulse is saturated, the Pockels cell is off and the polarization of the saturated pulse is rotated and switched out of the cavity. Since the regenerative amplifier is basically a laser cavity itself, it re-establishes the mode of beam and it helps to stabilize beam pointing through the amplifying chains. One thing should be noted is the existence of pre- and post-pulses coming out around the main pulse. Therefore output pulse is sent through another high-speed Pockels cell and sliced, and also sent through a combination of waveplate and polarizers. Beam is spatially expanded from 1 to 2 mm (FWHM diameter), resulting 3.5 mJ of pulse energy is sent to the next stage.

The second stage is a four-pass bow-tie amplifier. Generally, multi-pass amplifiers utilize a higher gain and large volume of Ti:sapphire crystal than the regen. It allows that a fewer passes are required to reach the saturation. 10 mm diameter, 20 mm long Ti:sapphire (α = 1.05 cm^{-1}) for this stage is also Brewster cut and pumped by 532 nm, 110 mJ pulses which is also from BigSky laser. About 90% of pump beam is absorbed in the crystal. The pump beam is arrived 350 ns before the seed and time difference between each pass is 7 ns. After four passes, pulse energy increases up to 20 mJ. Although 20 mJ is not a saturated energy in this amplifier, the limited pass length and angles do not allow more beam passes. Spatial mode of amplified pulse is cleaned with a vacuum spatial filter and it is expanded to 15 mm in diameter for the final amplification.

The final stage is an another multi-pass amplifier utilizing a Ti:sapphire crystal (α = 2.3 cm^{-1}) that is 20 mm long and 20 mm in diameter. Each side of crystal is normally cut and pumped by 1.4 J, 8 nm, frequency doubled *Q*-switched pulses from the Spectra Physics PRO 350 YAG laser. Since transmitted pump pulse still has about 10% of energy, it is reflected back to the crystal to deposit more energy in the Ti:sapphire. Crystal axis is oriented for vertically polarized beam. Precise orientation alignment can be accomplished by monitoring spectrum of output pulse. If the angle is not correctly set, the different light speeds along the different crystal axis cause modulation in the spectrum. Two pump lasers deposit ~ 28 W of average power in the crystal and ~ 9 W of heat produces a thermal effect on the beam; thermal lensing, even though it is mounted on a water cooled copper block. Divergence induced by this thermal lensing is corrected at the telescope either before or after the 5-pass amplifier. Flat top profile of the pump beams allows a super Gaussian profile of the amplified beam when it is saturated. By controlling the timing of each PRO laser, from 17 mJ to 1.2 J of output energy can be achieved.

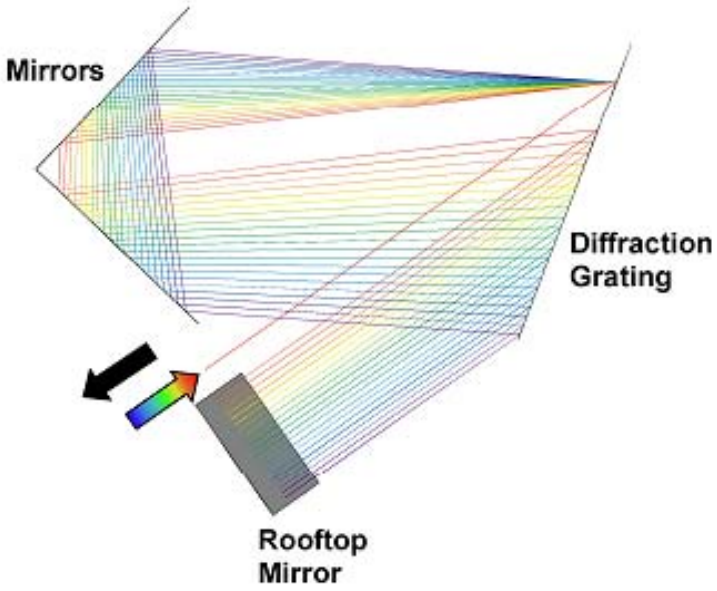

Figure 18. Ray tracing of the vacuum compressor [60].

Vacuum compressor

Amplified pulse is spatially expanded 3 inch diameter and sent to compressor in the vacuum chamber. This compressor equips the gold grating; 1480 lines/mm, 40 cm of diameter and two sets of roof-top mirrors (See Figure 18). By controlling the distance between the grating and horizontal roof-top mirrors, dispersions originally given by the stretcher are compensated accurately. Effective grating space is about 1.4 m. Grating efficiency is about 90% for whole spectral range of the laser. Therefore the entire throughput of the compressor is about 60% without spectral clipping. Compressed pulse energy was 700 mJ.

Final pulse length was measured with the second order single shot autocorrelator [62]. A pick-off mirror on the translation stage inserted into the center of beam after compression send the compressed beam to the beam splitter and they are recombined at a thin KDP crystal with an angle to generate second harmonic lights. The second

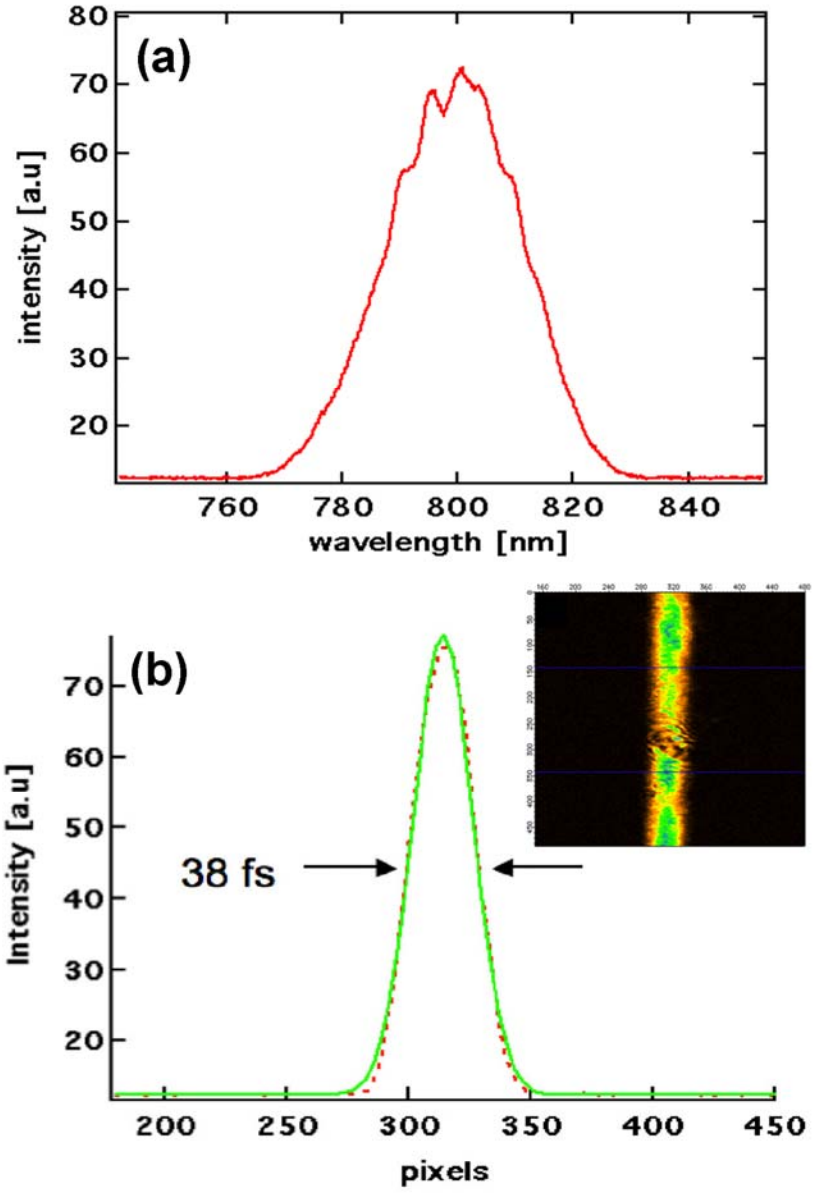

Figure 19. (a) Spectrum of fully compressed pulse. It was measured with MicroHR spectrometer at the clamshell target chamber. (b) Second order autocorrelation measurement (red dotted line). Gaussian fit of horizontal line out of image in the inset (green line).

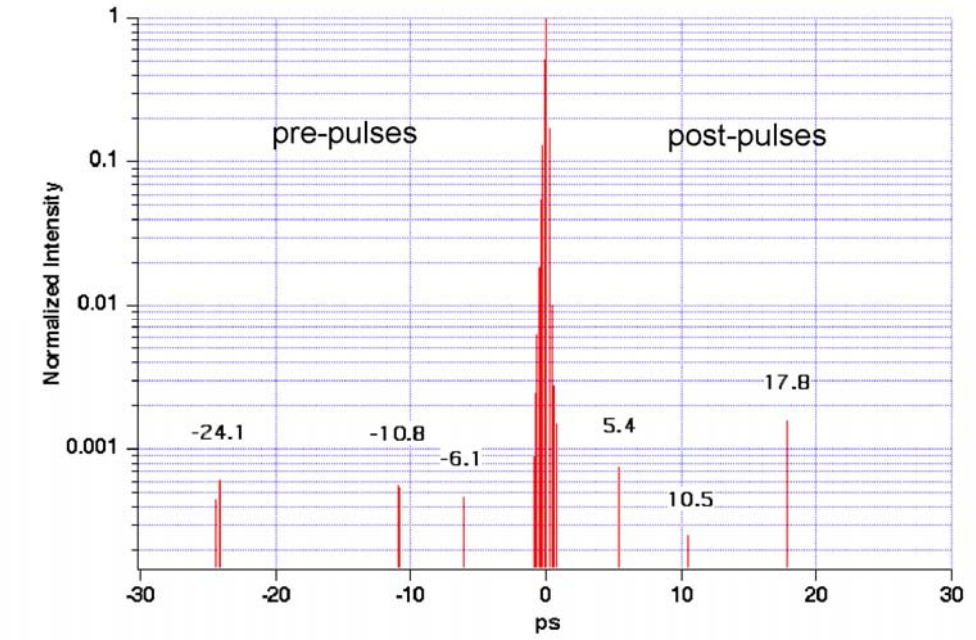

Figure 20. Pre- and post-pulses measured using the third order autocorrelator.

harmonics are filtered through BG39 glass and imaged on the CCD located outside of the compressor. A typical autocorrelation data is shown in Figure 20 (a). CCD pixel/time ratio is calibrated by monitoring pick positions at different delays given by one pass of beam. Gaussian de-convolution suggests that for the autocorrelation image in the Figure 19, CCD pixel/time ratio is 1.795 fs/pixel and fully amplified pulse has 38 fs duration.

Compressed pulses are also sent to the third order autocorrelator. The second harmonic generation from thin KDP crystal utilizes the type-I phase matching condition. The fundamental and the second harmonic beam are separated on a dichroic mirror and recombined on another dichroic mirror. Spatially collinear two color beams generate the third harmonics from BBO crystal and it is filtered through band-pass filters and UV coated mirrors. Calibrated glass plates and thin-transparent plastics are used as effective neutral density filters for UV. The third order autocorrelation scan shows a couple of pre- and post-pulses, of which magnitudes are about $10^{-3} \sim 10^{-4}$ of that of main pulse,

exist in ps ranges. Pre-plasma generated by these pre-pulses had been systematically studied by Hernan A. Sumeruk [63]. When the beam is focused up to 10^{19} W/cm^2, these pre-pulses generated ~ 3 μm of pre-plasma in front of the solid target surface. The effects from the pre-plasma should be taken into account to interpret data.

3.2. TARGETS

For experiments performed in the thesis, slab targets and cone / wedge targets with various materials and geometries had been shot. X-rays and transition radiations from flat targets were measured for characterizing our experimental conditions, comparing them with published results from other groups, and setting references for cone and wedge target data. Various shape of micro-structured targets were designed to investigate laser – cone interactions, such as polarization effects on hot electron generation and transport, and quasi-static electromagnetic field effects on cone surfaces for guiding light and electrons. All targets were mounted on an aluminum holder and grounded in the chamber.

3.2.1. Silicon wedge and pyramidal cone*

The reentrant cone targets were produced from (100) single crystal silicon wafers using standard semiconductor processing techniques [45, 46]. The silicon features were contrived by etching with KOH. Because the etching rate is strongly dependent on crystallographic orientation, we could etch into a (100) wafer structures with walls along the (111) planes, the angle between (100) and (111) planes being 54.5º resulting in cones and wedges with a 70.5º opening angle. Targets formed in this fashion are shown in Figure 21. The precision of the mask allowed the tip of the cones to reach within 10 μm of the back surface, and yielded a tip sharpness of better than 1×1 μm^2. Figure 21 (c)

* Detailed procedures for silicon cone and wedge are described in the chapter 4.

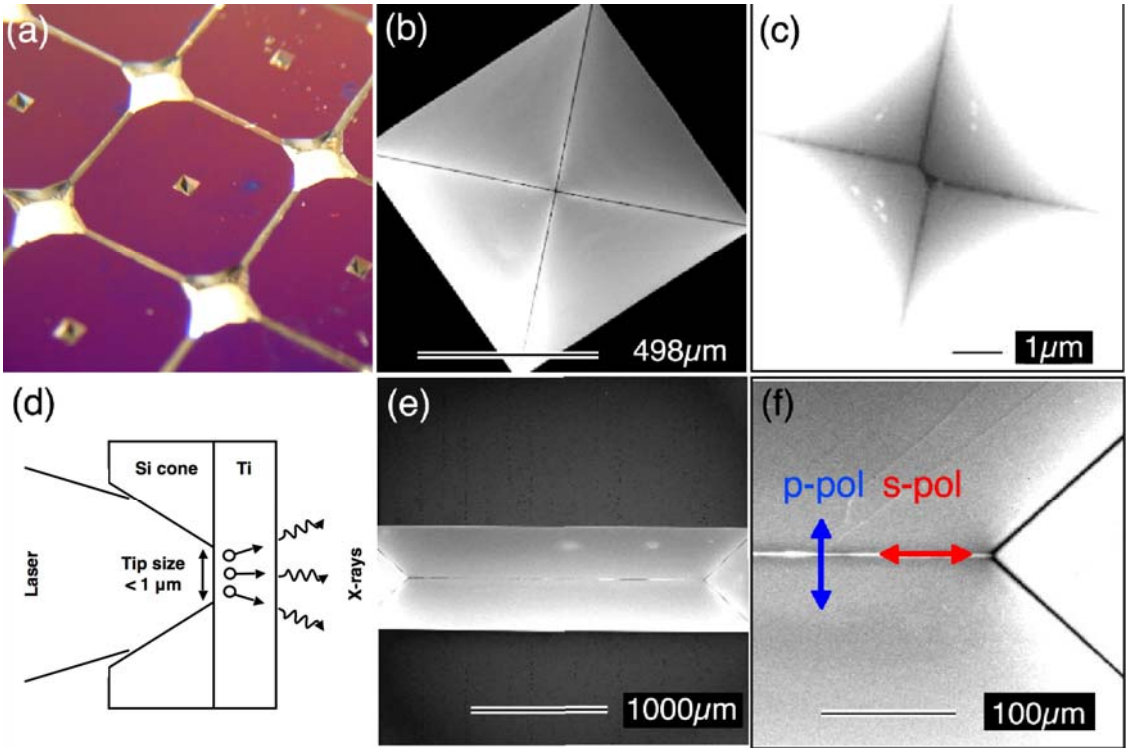

Figure 21. Photo and scanning electron microscopy (SEM) images of reentrant cones and wedges (a) Square based cones produced in an array (b, c) Cones produced in this way have very smooth walls and sharp tips (d) Geometry of the laser irradiation in the cone and wedge targets (e) Wedge target SEM (f) By orientation of the laser polarization, wedges can be used to study the 2D case of each polarization in isolation.

illustrates the micron-scale tip. The size of the square opening on the silicon slab surface is 700 × 700 μm^2 and the depth is 500 μm. In the same fashion, using rectangular patterns, we also produced silicon wedges, analogous to a 2-dimensional cone. These are also shown in Figure 21 (e). The wedge targets permitted us to study the electric field polarization effects on hot electron production; we utilized both *p*- and *s*-oriented polarization [Figure 21 (f)]. In order to generate titanium K_α fluorescence, 25 μm thick titanium foil was adhered to the back surface of the silicon.

3.2.2. Gold and copper cones*

Free-standing gold pyramid targets and copper cone targets had been fabricated by nanofabrication group at University of Nevada at Reno. Instead of etching negative structures into the silicon wafer, positive structures were remained by etching silicon bulk. This process could be done by applying techniques for making sharp micro probes for atomic force microscope [64]. SEM image of these pyramid arrays is presented in Figure 22. Gold layer of 10 μm thickness was deposited on the substrate. Because gold is very inert and not affected in KOH solution, silicon substrate could be etched and array of freestanding gold pyramids were obtained.

Copper cones were also obtained utilizing similar nanofabrication processes yielding thousands on a surface equivalent to a silicon wafer. However, unlike pyramid structure, cones did not have uniform shapes and sizes. Therefore, each target was characterized with a scanning electron microscope and categorized; long-nose (< 30°), 30°, 45° or 60° cone angles, and rough or smooth surfaces. Figure 23 shows typical cones with various opening angles. Such cones measure 250 μm at the base and 200 ~ 300 μm in height, and have 10 μm thick materials.

* Detailed fabrication techniques and procedures were patented by University of Nevada at Reno.

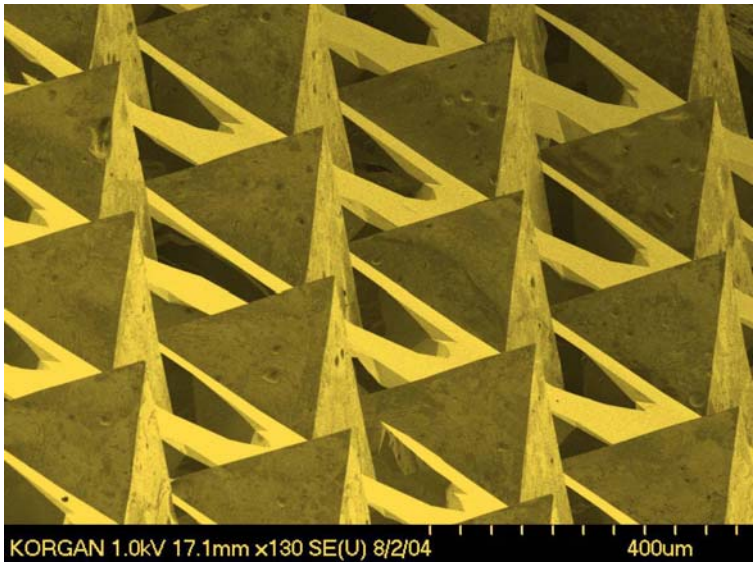

Figure 22. SEM image of positive silicon pyramid array. (Courtesy of Nathalie Renard-Le Galloudec)

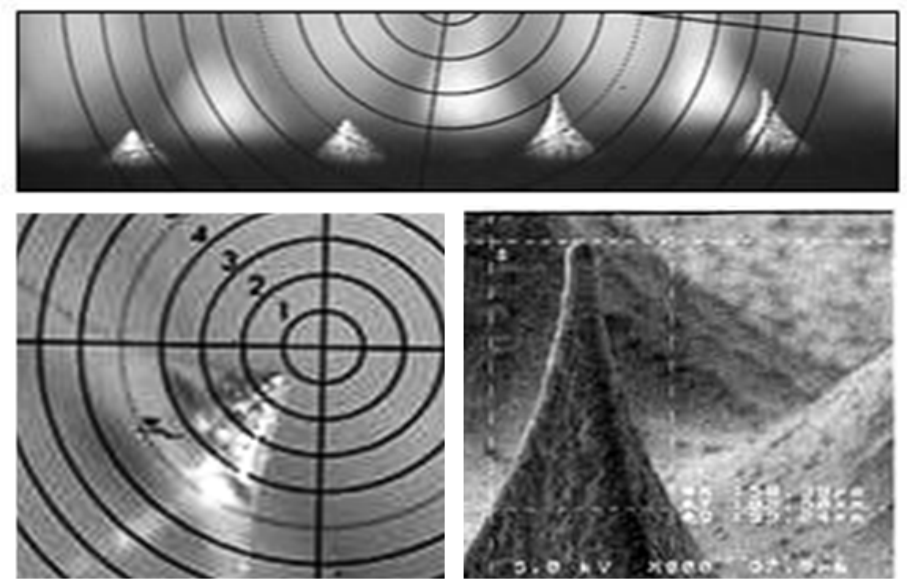

Figure 23. SEM images of copper cones, of which opening angles are 30° ~ 60° and material thickness is 10 μm. (Courtesy of Nathalie Renard-Le Galloudec)

3.3. CLAM SHELL TARGET CHAMBER AND DIAGNOSTICS

For all experiments in the thesis, the blue clamshell target chamber (a.k.a. solid target chamber) in the THOR target area was used. A spherical volume with a diameter of 24 inch is connected to the switchyard chamber through 4 inch vacuum tube. A gate-value installed in the middle of a beam line isolates the chambers and allows breaking the vacuum without venting the compressor. Normal operating pressure for experiments is less than 10^{-4} Torr.

Various diagnostics for the laser, x-rays and optical emissions from targets were equipped inside and outside of the chamber. In this section, I will briefly introduce each diagnostics.

3.3.1. Off-axis parabolic mirror and laser focusing

The THOR laser pulses were focused into the targets with an aspheric mirror.* It is a gold-coated, 45º off-axis parabola with an aperture diameter of 76.2 mm and a focal length of 178.53 mm, resulting F/#2.8. Focused beam is imaged with a 20× microscope objective or two inch diameter achromatic lens with f = 100 mm onto a CCD camera at outside of the chamber. Air force test images were used for the calibration of the far field beam diagnostics.

Spatial beam profile along the laser propagation, i.e. z-direction is defined as a $1/e^2 \sim 0.135$ intensity radius $w(z)$ which is given by [65]

$$w(z) = w_0\left(1+\frac{z^2}{z_r^2}\right)^{1/2}. \qquad (86)$$

It assumed its minimum value of w_0 at z = 0 plane. $2w_0$ is called waist diameter of the beam. $z_r = \pi w_0^2/\lambda$ is known as the Rayleigh range in which the beam can be treated as collimated.

* JANOS technology Inc.

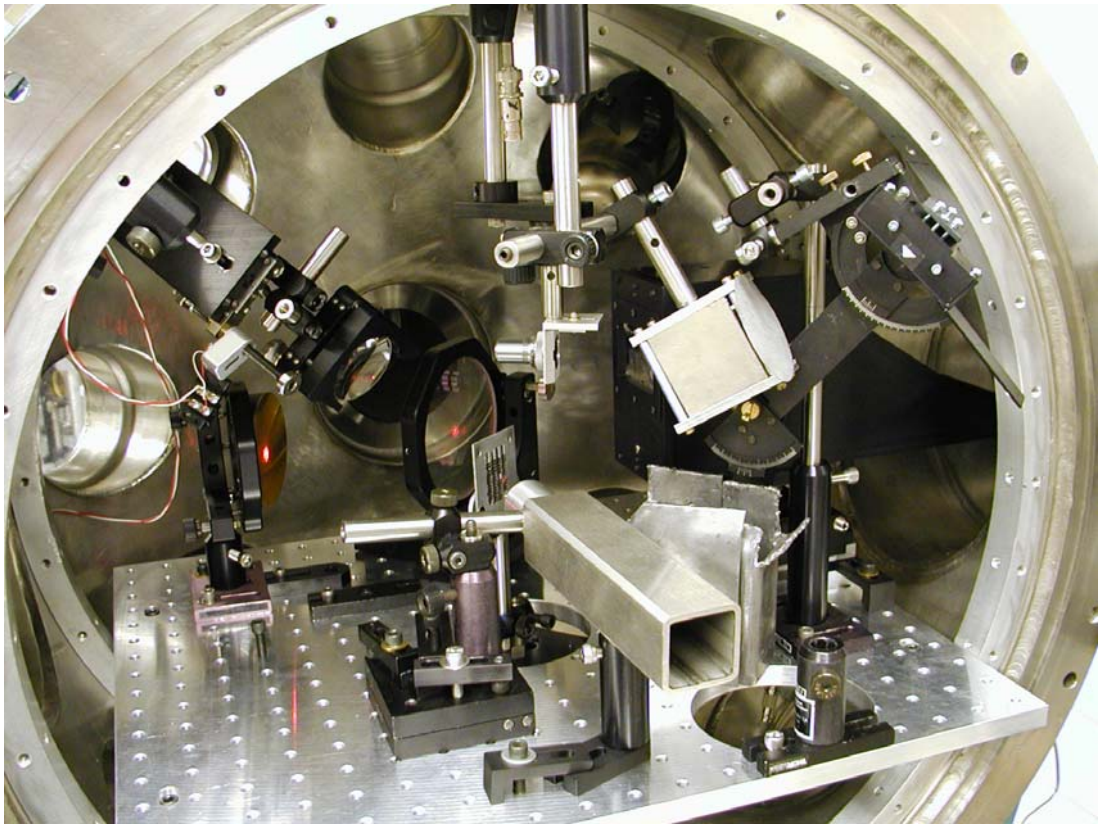

Figure 24. An example of solid target chamber setup. This is for x-ray spectroscopy experiment of which results are presented in the chapter 5.

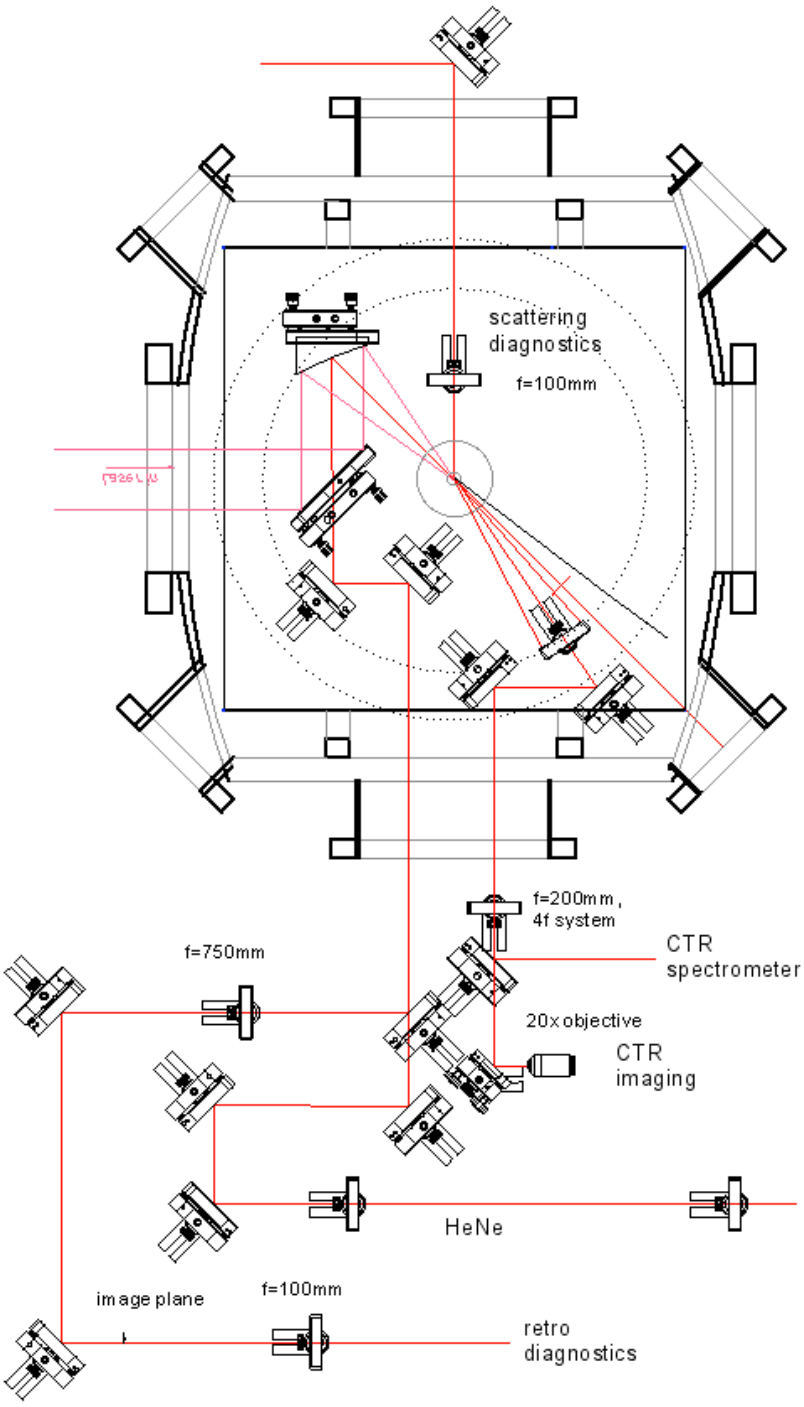

Figure 25. An example of CAD drawing of the solid target chamber and CTR diagnostics setup.

In general, focal spot diameter can be expressed in terms of F/# of beam. Assuming D is a the diameter of the collimated beam before focusing optics,

$$d_0 = 2w_0 = \frac{4}{\pi}\frac{\lambda f}{D} = \frac{4}{\pi}\lambda F/\#. \quad (87)$$

Since the focal spot size given by this formula is diffraction limited, its validity must be always confirmed by measurement.

3.3.2. Scattering and retro diagnostics

To find accurate target position respect to the laser focus, two backscattering diagnostics were installed. We set a coaxial alignment HeNe beam and a sharp STM tip in the beam pass. Scattered lights from the tip were collected by a lens set off the z-axis and imaged on the CCD (magnification ~ 30). This off-axis scattering diagnostic translates the z-position of the tip into x-y position on the CCD (Figure 26). Sharpness of STM tip and the high magnification ensure precise control of z-position. For the cone and wedge target shots, after setting z-position of target, a precise alignment in x-y plane is required and a retro diagnostic is a key for this task.

Two types of retro diagnostic are used for this thesis. The first is utilizing alignment screen (Figure 27). By monitoring the diamond pattern of the back reflected HeNe lights on the removable screen, precise control of x-y target positions respect to the laser focal spot is accomplished. However, for round and various angle of cones, clear diamond patterns are hardly observed. Hence another type of retro-imaging diagnostic was designed. ASE is reflected back on target surface and the leakage through the last turning mirror is relayed onto a CCD, through a lens (f = 750 mm). This telescope consisting a parabola (f = 178.53 mm) and a lens images the back reflection of ASE with magnification of 4.2 [See Figure 26 (b)]. When the cone is off from the laser axis, due to the conical shape of the target, lights get reflected out of the axis and are not collected by the imaging system. As ASE enters a cone on axis, it is reflected symmetrically and

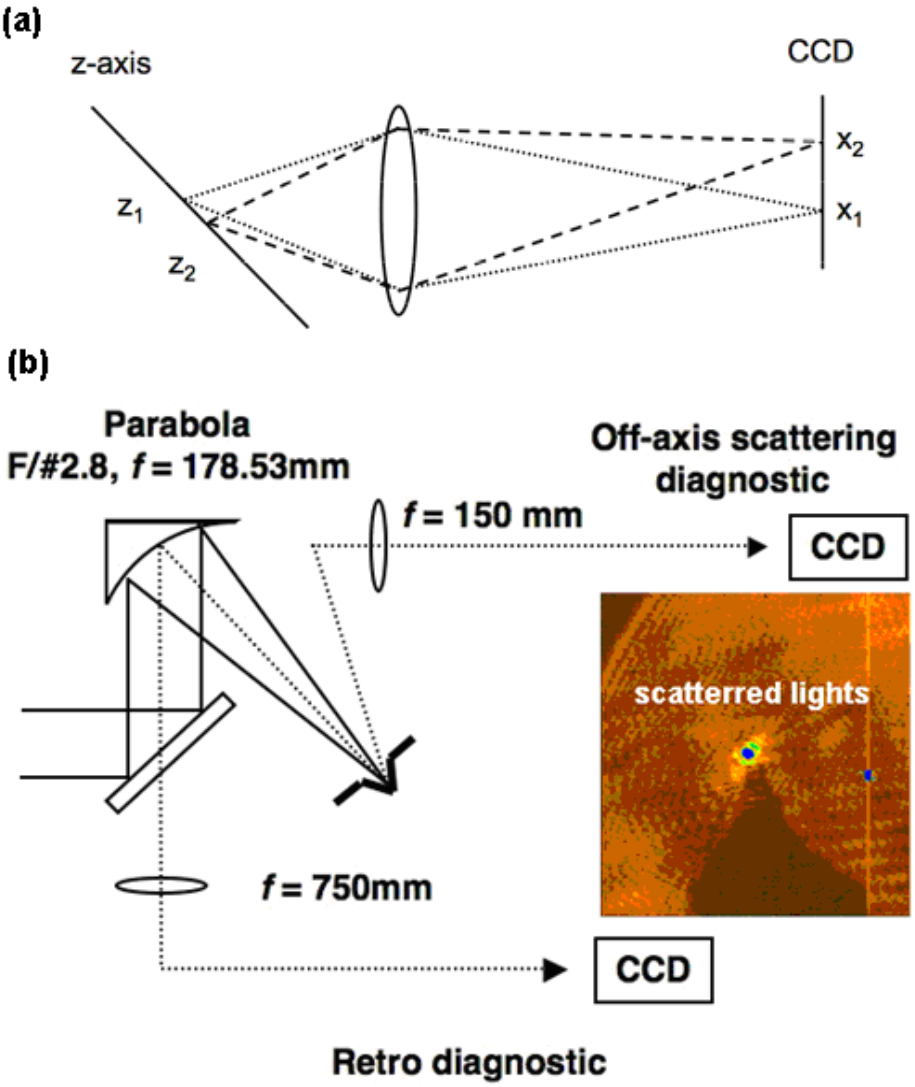

Figure 26. (a) Off-axis scattering diagnostics. Scattered lights from z_1 and z_2 are imaged on x_1 and x_2, respectively. (b) Schematics of the scattering and retro imaging diagnostics. (Inset) Image of scattered lights from a STM tip.

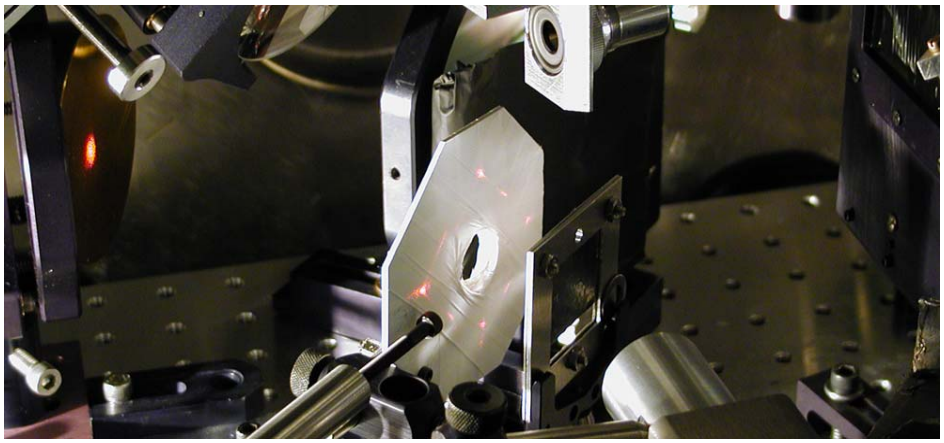

Figure 27. Photograph of a removable screen.

fills a wide area on the plane being imaged. Indeed we could see a symmetric light pattern filling the entire image on the backscattering. Utilizing this technique, the precision obtained in the plane perpendicular to the laser axis was of the order of 1 μm.

3.3.3. X-ray pinhole camera

A pinhole camera with proper band-pass filters such as beryllium foil and thin aluminum film is the simplest instrument for imaging spatial distribution of x-ray radiations. In general pinhole camera theory, a small pinhole results in good image resolution. However a small diameter of which is compatible with wavelength causes diffractions and less imaging quality. Diffraction pattern from a round pinhole is known as the Airy pattern [66];

$$I/I(0) = \left[\frac{2J_1(ka\sin\theta)}{ka\sin\theta}\right]^2 = \left[\frac{2J_1(kaq/R)}{kaq/R}\right]^2 \qquad (88)$$

where J_1 is the Bessel function of 1st order. Other variables are also indicated in the Figure 28. At the 4th peak of this function where $ka\sin\theta = 11.6$, $I/I(0)$ drops 10^{-3}.

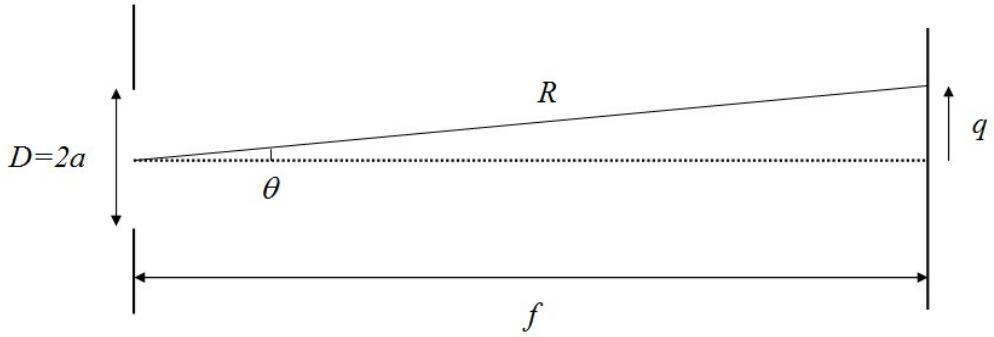

Figure 28. Pinhole camera geometry. D: pinhole diameter, *f*: focal length of the pinhole camera.

If two identical spots are imaged, when one center of the Airy pattern falls on this point, two spots can be considered to be clearly resolved. This condition is written as

$$q \approx \frac{11.6}{\pi}\frac{\lambda f}{D} \tag{89}$$

where f is a focal length, i.e. the distance from the pinhole to a film and normally $f \sim R$. By setting $q = D$, an optimum pinhole size can be obtained by

$$D = 1.9\sqrt{\lambda f}\ . \tag{90}$$

In case of x-rays, wavelengths are very small, so the diffraction is not considered seriously. However, when a diameter approaches a thickness of plate, a pinhole is considered as a cylinder and shadings effect from the side of cylinder should be counted. In addition, due to an usually low sensitivity of DEF x-ray films, an extremely small diameter could hardly ensure good exposures. To select a right pinhole size, above points need to be considered.

A material for the plate on which a pinhole is punched should be thin and block x-rays effectively. To satisfy these criteria, a high Z soft metal such as gold and platinum is usually chosen. For the experiments, 50 μm of pinhole on a 10 μm thick plate of 95%

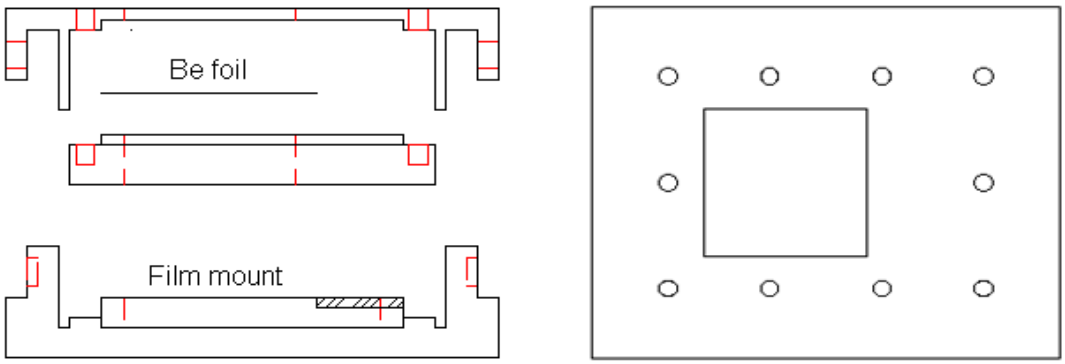

Figure 29. X-ray film cassette made with stainless steel. (Left) Side view and (right) top view. This cassette is separated from the pinhole tube and designed light-tight.

of platinum and 5% of iridium alloy was used*. Focal length was 50 mm.

The original design of pinhole camera was all-in-one type; the pinhole and film were placed in the same tube. However, because of small sizes of pinhole and x-ray source, aligning pinhole camera for every shot was a time – consuming process. To avoid it, whole camera system was mounted on the kinematics base plate and the alignment can be restored after unloading / loading films in a dark room. Improved design was separating film cassette from the tube (See Figure 24). Light-tight designed cassette made it possible to unload and load film without touching pinhole alignment (See Figure 29).

3.3.4. Von Hamos spectrometer

In the von Hamos scheme [67], Bragg crystal surface is bent into a cylindrical shape. Bragg condition of x-ray with a wavelength λ for n-th order reflection is given by

* Electron microscope aperture from Ted Pella, Inc.

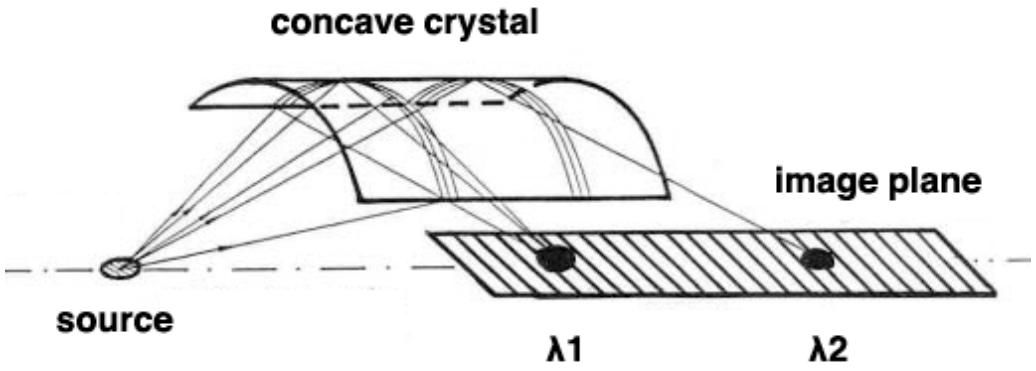

Figure 30. Schematic of the von Hamos spectrometer [68]. Both x-ray source and images are on the cylindrical axis.

$$2d\sin\theta = n\lambda \tag{91}$$

where d is the lattice spacing of crystal and θ is the Bragg angle. As described in Figure 30, both x-ray source and images lie on the cylindrical axis. Short wavelengths are imaged further from the source than long wavelength, and depending on the length of the crystal, this can cover a very wide range of spectrum.

The spatial resolution of the spectrometer is limited by the aberration due to off-axis source, e.g. source has an area. The width of the line images can be estimated by $\Delta y = 2R\Delta\alpha/\sin^2\alpha$, and generally it exceeds the source size.

For our experiments, PET crystal with 10 cm of radius curvature was equipped in the spectrometer. This crystal covers titanium $K\alpha$, $K\beta$, Heα and Heβ lines. On the imaging plane, Kodak RAR 2492 film was placed. Because of low reflectivity of crystal and low sensitivity of the film, 30 ~ 50 shots have been integrated for each configuration to ensure a good exposure.

3.3.5. Spherically bent crystal spectrometer

A spherically bent crystal spectrometer, namely focusing spectrometer with spatial 1D resolution (FSSR-1) utilizes both the focusing aspects of the spherical mirror and the Bragg diffraction of x-rays [69]. When we set a distance from object to the crystal pole p, and the crystal to detector q, and the radius of curvature R, the lens formula yields

$$\frac{1}{p}+\frac{1}{q}=\frac{2\sin\theta}{R} \tag{92}$$

where θ is the Bragg angle. In order to get a spectral resolution independent to source size, crystal is aligned on the Rowland circle and detector need to be place on it (Figure 31). The Rowland circle, also called a focusing circle is the circle drawn tangent to the

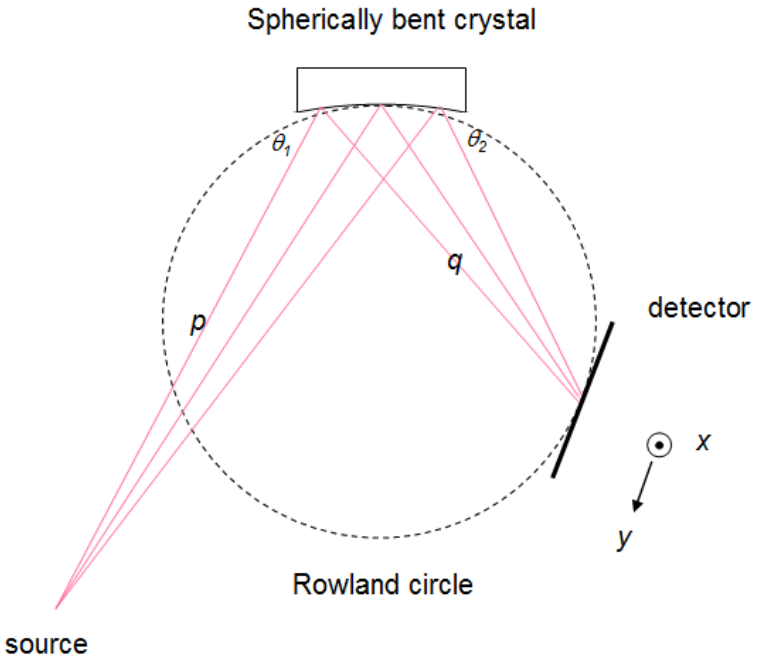

Figure 31. Schematic diagram depicting x-ray microscopy system using a spherically bent crystal.

face of a concave crystal at its midpoint and has a diameter equal to the radius of curvature of crystal. The specular beam and the dispersed beam are focused at other points on this circle. The detector and source positions are given by

$$q = R\sin\theta, \tag{93}$$

$$p = -\frac{R\sin\theta}{\cos 2\theta}. \tag{94}$$

As a result, in the plane of detector, spatial image is formed in the x-direction and spectral information is recorded in y-direction. Magnification of the one-dimensional image is $-\cos 2\theta$.

The FSSR-1 used for our experiment utilized the seventh order Bragg reflection of Mica crystal with R = 160 mm, for titanium $K\alpha_1$ (4510.8eV) and $K\alpha_2$ (4504.9eV) lines. Demagnification factor is 1.15.

3.3.6. Scintillation gamma-ray detector

Hot electrons generated from the laser-solid interaction cause a lot of bremsstrahlung radiations from the interaction region (See chapter 2.3.2). These gamma rays interact with a scintillator and produce light pulses. Lights are converted to electric signal by a photomultiplier tube (PMT), which consists of a photocathode, a focusing electrode and 10 or more dynodes. The anode and dynodes are biased by a chain of resistors. For a scintillating material, thallium activated NaI crystal is commonly used. For our experiments, NaI(Tl) crystals of which diameter of 1 inch and thickness of 1 cm were utilized. Large area of alkali halide provides a good x-ray stopping power and a small amount of thallium impurities are efficient light producers.

Responses of each detector were calibrated with a radioactive sodiumm-22 source, which gives photons of 0.511 MeV (β+, 90.6 %), 1.274 MeV (electron capture, 9.4 %) and 1.785 MeV (the sum of two). In early, Stefan Kneip calibrated detectors to response the same at 900 V [70]. Later, they had been recalibrated at 500 V. However

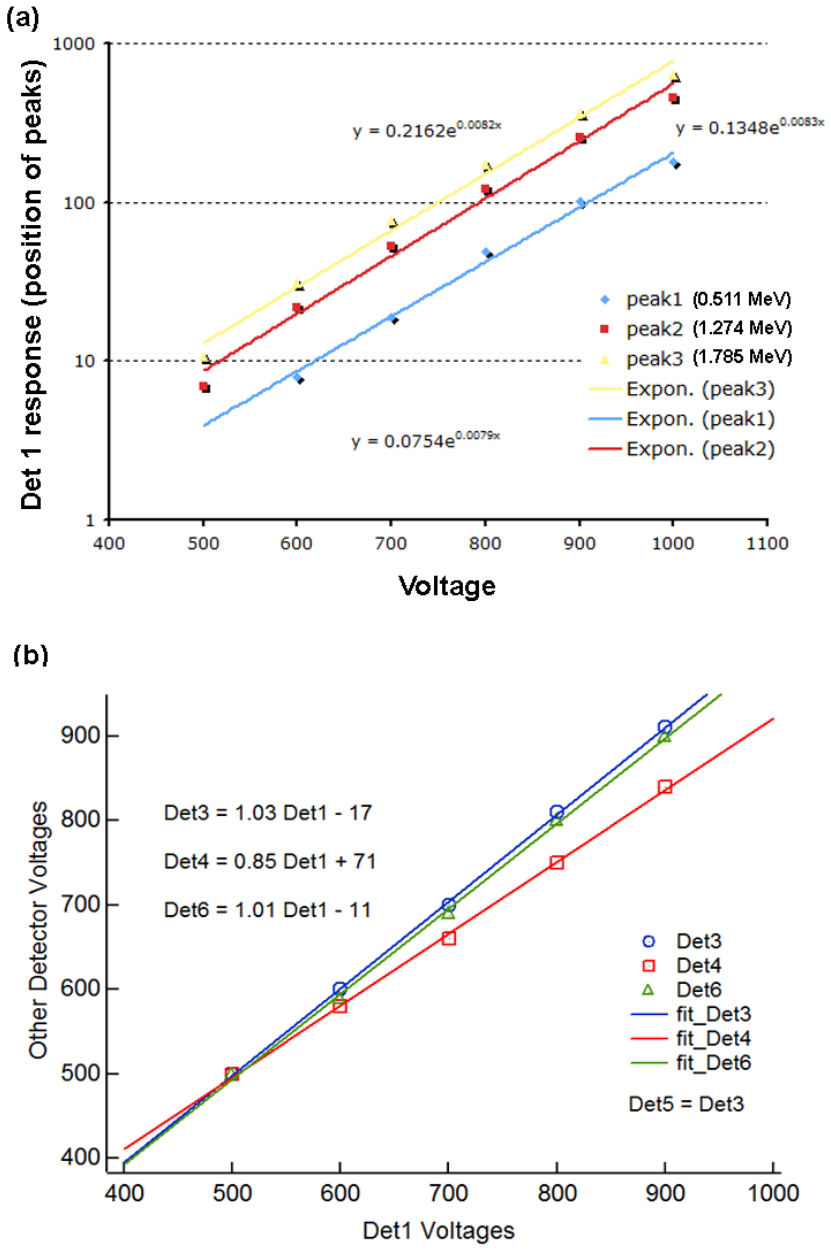

Figure 32. (a) NaI detector response at different voltage. (b) Other detector response as a function of detector 1.

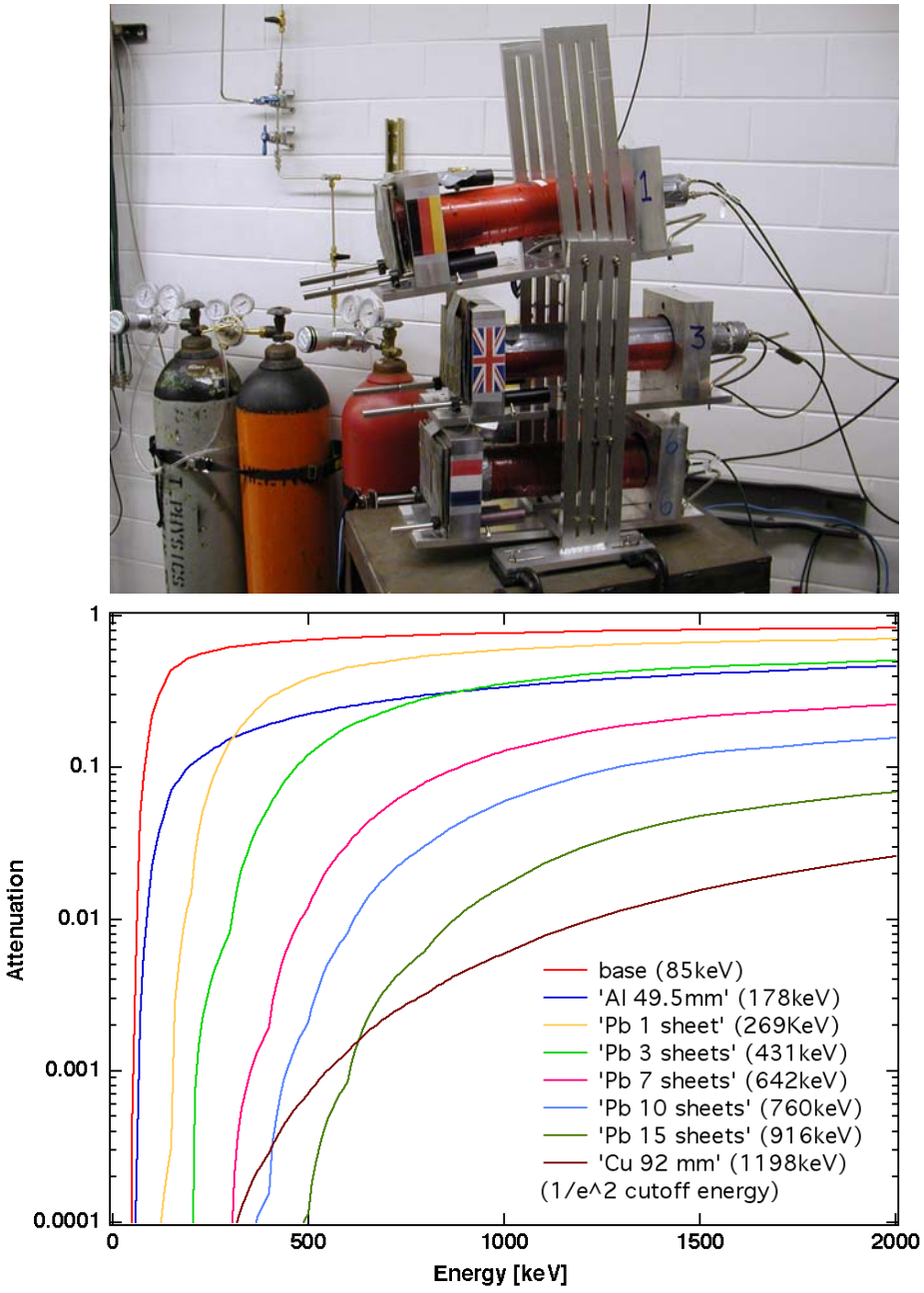

Figure 33. (Top) Photograph of gamma ray detectors. (Bottom) Transmission curves for various filters. "Base" means the baseline shielding of x-ray by the target chamber wall and the detector housing.

each detector responses differently at different voltages. Therefore detector responses were compared with respect to detector 1. Figure 32 (a) presents the position of each peak from the detector 1 at different voltage and Figure 32 (b) shows that voltages of other detectors which gave the same peak position as that of detector 1. Using these, data from all detectors could be cross-compared and normalized.

Each detector was shielded with a thick lead tube with an aperture pointing at the target. Different filters were installed in front of the detectors. Various thicknesses of lead and copper plates were chosen to measure x-ray yields in the 100 keV to 1200 keV photon energy range. X-ray attenuation is given by

$$I / I_0 = \exp\left(-\mu_\rho \rho l\right) \tag{95}$$

where μ_ρ is the energy dependent mass attenuation coefficient, ρ is material density, and l is the thickness. Attenuation of the target chamber and detector housing, and various filters are calculated using x-ray database provided by the NIST website [71]. Cutoff energy of each filter is considered as energy where transmission is $1/e^2$. Deposited x-ray energies though various filters provide information about the temperature of hot electrons producing x-rays.

3.3.7. Transition radiation imaging and spectrometer

Optical emission from the target rear surface was imaged on to a CCD camera and to a spectrometer entrance slit using a dichroic lens (f = 100 mm) set on the laser axis with a magnification of 20. Various band-pass filters such as BG39 and RG750 and neutral density filters were inserted in the beam pass to select specific bandwidth of emission and to ensure good exposures.

In order to image emissions at around 800 nm and 400 nm, we used WAT-902H* CCD cameras that equip the SONY ICX429ALL CCD sensors. This CCD has very

* Watec camera Inc.

good responses in both visible and infrared ranges. Its spectral response is shown in the Figure 34 (Top).

Transition radiations were also imaged onto the entrance slit of MicroHR spectrometer*. It is a short focal length Czerny-Turner type spectrometer fitted with a 600 grooves/mm grating blazed at 750 nm. Typical schematic of Czemy-Tuner monochromatic is presented in Figure 34 (Bottom). Radiations are imaged on the entrance slit placed at the effective focus of a collimator. The collimated lights are refracted from the grating and then collected by another curved mirror which refocuses lights on the exit slit. At the exit slit, the colors of light spread out.

In case of the MicroHR, the exit slit is replaced by a CCD camera. On a CCD, spectral information is shown in one direction and spatial image is formed in the perpendicular direction. By tuning grating angle 0 ~ 2000 nm of spectral range can be covered.

* HORIBA Jobin Yvon

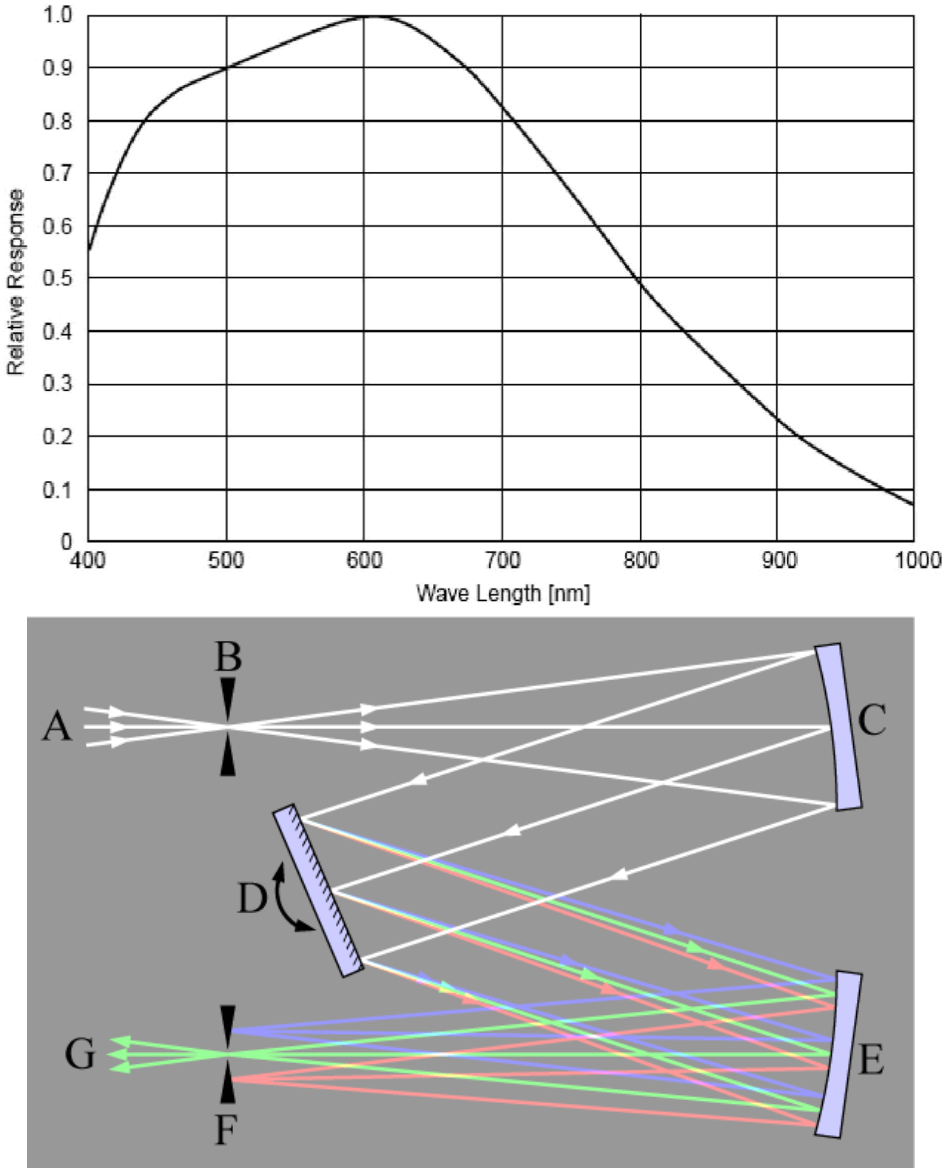

Figure 34. (Top) Spectral sensitivity characteristics of ICX429ALL.* (Bottom) Standard Czerny-Turner configuration.†

* http://www.teleskop-service.de/VideoCCD/Video/ICX429ALL.pdf.
† http://upload.wikimedia.org/wikipedia/en/e/e8/Czerny-turner.png

CHAPTER 4. SILICON TARGET FABRICATION

In this chapter, I describe the properties of silicon, MEMS techniques and target fabricating procedures using them. Most processes for silicon cone and wedge target have been done in the north clean room at Microelectronic Research Center in Pickle Research Campus. Step-by-step operating procedures for major tools in the clean room are described.

4.1. CRYSTALLINE STRUCTURE OF SILICON AND ANISOTROPIC KOH ETCHING

Silicon forms a diamond lattice consisting of two interpenetrating face-centered cubic lattices with a lattice spacing of 0.54 nm. Differing hybridized (sp^3) orbital orientation on different crystal planes causes drastic differences in chemical reaction. Normally (110) plane is the fastest etching primary surface. The ideal (110) surface has

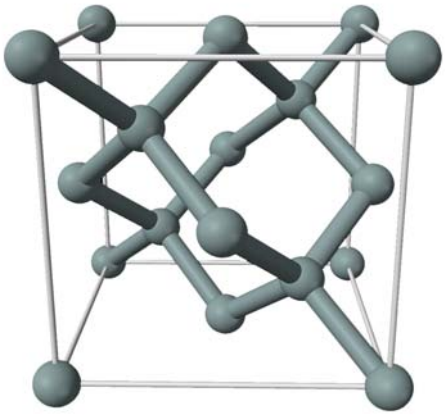

Figure 35. Diamond structure of silicon*

* http://en.wikipedia.org/wiki/Image:Silicon-unit-cell-3D-balls.png

a more corrugated atomic structure than the (100) and (111) primary surfaces. The (111) plane is an extremely slow etching plane that is tightly packed, has a single dangling-bond per atom, and is overall atomically flat. These properties of each plane are used to produce the standard anisotropically etched structure on a silicon wafer.

Several hydroxides such as KOH, NaOH, and Tetramethylammonium hydroxide (TMAH) are often used for anisotropic etching of silicon. General chemical processes can be described as following;

1. Oxidation of silicon by hydroxils to form a silicate

$$Si + 2OH^- + 4h^+ \rightarrow Si(OH)_2^{++} \quad (96)$$

2. Reduction of water

$$4H_2O \rightarrow 4OH^- + 2H_2 + 4h^+ \quad (97)$$

3. Silicate further reacts with hydroxyls to form a water-soluble complex

$$Si(OH)_2^{++} + 4OH^- \rightarrow SiO_2(OH)_2^{2-} + 2H_2O \quad (98)$$

As a results, overall redox reactions is given by

$$Si + 2OH^- + 4H_2O \rightarrow SiO_2(OH)_2^{2-} + 2H_2O \quad (99)$$

KOH is a typical and mostly used hydroxide. Its etching rates through different

Crystallographic Orientation	Etching Rate (μm/min)
100	0.797 (0.548)
110	1.455 (1.000)
111	0.005 (0.004)

Table 1. Chemical etching rate vs Silicon orientation in 70°C, 30% KOH solution.

silicon plane are shown in Table 2 [72]. Because of the lowest etching rate, the (111) family of crystallographic planes are normally the "stop" planes for etching processes, and intersection of these planes produces a standard anisotropic V-groove etching structure on (100) silicon wafers.

4.2. SILICON ON INSULATOR AND THE DESIGN OF SHADOW MASK

Silicon-on-insulator (SOI) wafer* refers a sandwiched structure; a layered silicon-insulator-silicon substrate. As an electrical insulator, silicon dioxide is commonly used. The topmost silicon layer and insulating layer vary widely with applications. For the most case of cone and wedge target fabrications described in the thesis, (100) oriented

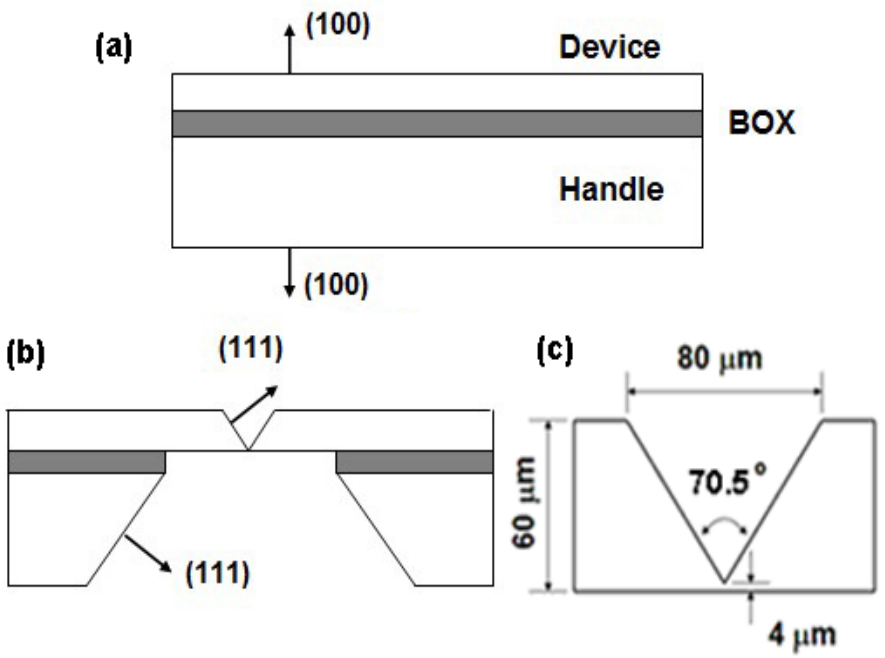

Figure 36. (a) Typical structure of SOI wafer. The topmost layer is also called device and the bottom layer is often called handle. For cone target, both (100) oriented device and handle layers are used. (b) Side view of processed SOI wafer. (c) Side view of pyramid / wedge geometry etched on device.

* Ultrasil cooperation, http://www.ultrasil.com

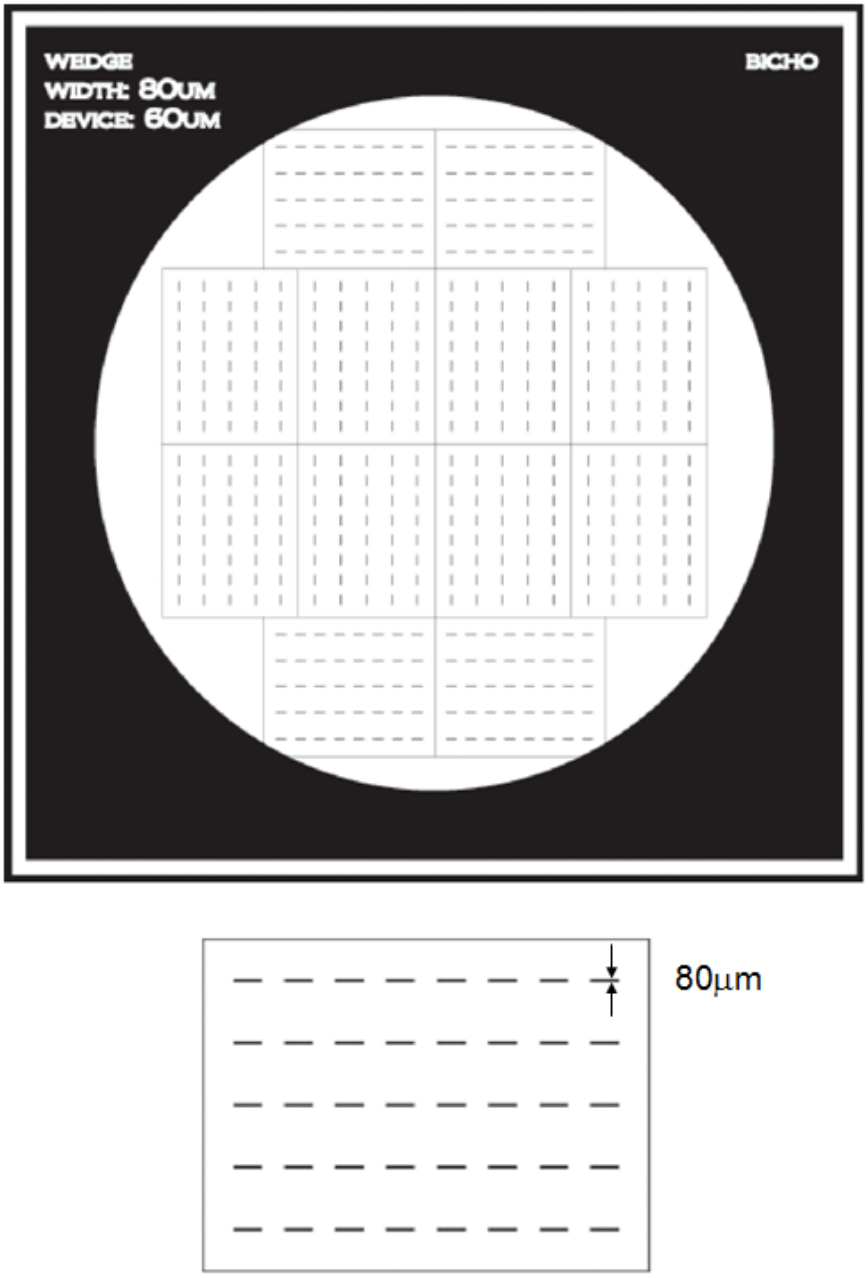

Figure 37. Mask design for the wedge. Designed pattern will be "reversely" printed. (dark → transparent, transparent → dark). Printed film is attached on 5" × 5" soda-lime glass plate. Ten pieces of targets are placed in 4 inch wafer and 40 wedges are etched in each peace.

60 μm device and 1 ~ 2 μm of buried oxide (BOX) are chosen.

A pyramidal cone (or wedge) structure could be etched through a square (or a rectangle), of which sides are parallel to <100> direction* of crystal. Since angles of pyramid are determined by a crystalline structure, i.e. the angle between (111) surfaces, the size of square (or rectangle) determined the depth. For example, 80 μm × 80 μm square results in 56.5 μm depth of pyramidal cone. So by choosing 60 μm of device layer, we could remain 3 ~ 4 μm thick material between cone tip and the rear surface of target.

A pattern with micrometer accuracy was designed using Adobe illustrator CS. For a structure in Figure 36 (b), two patterns are required, one for the pyramid (or wedge) on the device layer and the other for etching handle layer from the below. Typical pattern to etch wedges is displayed in Figure 37. It can be printed on the transparent film using high resolution laser printer (3556 dot per inch)†. Printed film is attached on soda-lime glass plate using transparent tapes. It is an easy and cheap solution but the resolution of patterns is limited by a dot size of printer, which is about 7 μm. For better quality, patterns can be etched on chrome coated glass (or quartz) plate‡. This method typically can hold the feature size within approximated +/- 2 μm, and +/- 0.5 μm of tolerance.

4.3. WAFER PROCESSING

4.3.1. Silicon nitride deposition

SOI wafers brought in the clean room should be cleaned to get rid of possible contaminations. Piranha solution is a mixture of sulfuric acid (H_2SO_4) and hydrogen peroxide (H_2O_2), and it removes most organic matter on wafer surfaces. It will also

* The [100], [010] and [001] directions in a cubic crystal are referred to as the <100> direction.
† Graphic Arts Inc., http://home.austin.rr.com/graphicartsinc/
‡ PHOTOPLOT store, http://www.photoplotstore.com

hydroxylate most surfaces, making them extremely hydrophilic (water compatible). Thus an optical HF process would be required for some processes. Hydrofluoric acid etching removes silicon dioxide which is naturally grown or formed during piranha cleaning. Piranha process in the "H14 Hood" is the following;

1. Log on.
2. Fill the cascade rinser and all containers with DI water and wait until the resistivity is at least 12 MΩ-cm. Place wafers in the holder and Teflon tweezers in the cascade rinser while rinsing.
3. Prepare the piranha solution. Mix 825 ml hydrogen peroxide and 1650 ml the sulfuric acid in the quartz tank. Allow the solution to sit for 5 minutes.
4. Place wafers and tweezers into the piranha solution for 8 minutes.
5. When piranha clean is completed, place the wafers and tweezers in the cascade rinser again and perform two 5-cycle rinses.
6. Dump cascade rinse and remove wafers unless performing the optional HF oxide etch.
7. Optional HF etch:
    a) Pour 2400 ml of DI water into the polypropylene tank and add 120 ml of 49% hydrofluoric acid.
    b) Put the wafers into the HF solution until wafer surfaces de-wets (~ 20 seconds).
    c) Place the wafers back into the full cascade tank for rinsing.
    d) Perform rinses until the resistively reaches 12 MΩ-cm.
8. Dry wafers either using N_2 gun or spin rinser dryer (SRD).
9. Aspirate piranha and HF solutions, and rinse all containers with DI water (Same as step 2).
10. Log off.

Piranha cleaned wafers are transferred to a low pressure chemical vapor deposition (LPCVD) furnace. "MRL-LPCVD Nitride" tube [Figure 38 (a)] is fully computer controlled and several deposition recipes are pre-installed. For a low stress silicon nitride film (Si_3N_4) growth, we have used the "Nitride1" recipe. At moderately high temperature (~ 900 °C) and low pressure (~ 100 mTorr), low stress nitride film is deposited with a rough rate of 40 Å/min, using dichlorosilane ($SiCl_2H_2$) and ammonia (NH_3) gases. Silicon nitride provides a robust resists against KOH (etching rate ~ 14 Å/hr). "MRL-LPCVD Nitride" operating process is the following.

1. Log on.
2. Go to the 'recipe loader 'on the MRL control computer and select the nitride furnace '5-2'.

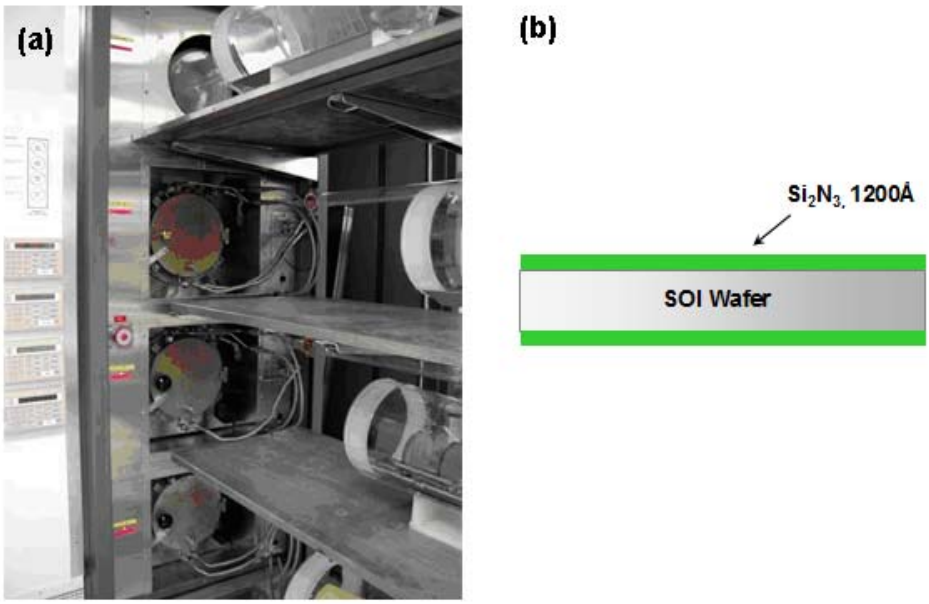

Figure 38. (a) MRL LPCVD Nitride furnace* (b) Nitride film after 30 minutes of deposition.

* http://www.mrc.utexas.edu/images/ equipment/MRL-POCI.jpg

3. Select the desired recipe (Nitride1) and deposition time (30 minutes for ~ 1200 Å).
4. Enter MRL control password and load the recipe.
5. Record run data (user, recipe, deposition time) in log book.
6. In the tube status, select nitride window and start the run.
7. Ware extra clean gloves.
8. At the load / unload step, place wafers in boat including buffer wafers to ensure uniform deposition using piranha cleaned tweezers. Transfer the boat into the furnace using a clean quartz rod.
9. Close the furnace door and release the 'hold' button on the computer.
10. Hold the furnace door closed until the system has been pumping for 5 ~ 10 seconds.
11. Wait for the deposition to run automatically and the load / unload step.
12. Ware new extra clean gloves and remove the boat from the furnace using a rod.
13. Close the furnace door and release the 'hold' again. Wait for the remaining processes completing.
14. When the recipe finishes, load the "idleLP" recipe and run it.
15. Allow the boat and wafers to cool down and measure nitride film thickness using "NANOSPEC microscope".
16. When "idleLP" is done, log off.

4.3.2. Photolithography

For photolithography, wafer need to be covered with photoresist (PR) and a clean and dry surface is desired for uniform spin coat. Generally wafers out of LPCVD furnace are considered to satisfy these conditions, however, some moisture or chemical contaminations might be presented on the wafer which had been sitting in the air for a

while, even though in the clean room. In particular, moisture reduces the adhesion of photoresist to the wafer. Thus, unless it had been transported from nitride furnace within a couple of hours, hexamethyldisilazane (HMDS) is applied on a wafer surface as an "adhesion promoter". It can be done in "HMDS oven" in the silicon litho bay.

The AZ5209E photoresist is used for the most works described in this thesis. Spin coating runs at about 3000 rpm for 30 second and produces 0.9 μm thick of PR layer on a wafer. The "L10 Hood" is designated for this process.

1. Log on.
2. Line the spinner basin with clean room wipes.
3. Choose the correct wafer chuck size (for 4 inch wafer) and push it onto the spindle.
4. Turn the spinner power on and set time (30 second), acceleration (1500 rpm/sec), and speed (3000 rpm).
5. Place a wafer centered on the chuck and turn the vacuum on to hold it.
6. Put AZ5209E photoresist in the center of wafer (2 ~ 3 dropper-fulls).
7. Push the start button to spin.
8. When spin table stops, turn off the vacuum and remove a wafer.
9. When coating is completed, take the wafer chuck off and place the PR-soaked wipes into a zip-lock bag, seal and place it in the red solvent waste can.
10. Log off.

The PR-coated wafer need be pre-baked at 90 °C for 2 minutes on a hot plate. It will drive off excess solvent in the future process. After pre-baking, photoresist is exposed to intense ultraviolet lights (360 nm, 10 mW/cm^2) through a shadow mask. Since AZ5209E is a positive photoresist, it becomes chemically less stable after exposure. It is done using "Karl Suss mask aligner" [Figure 39 (a)].

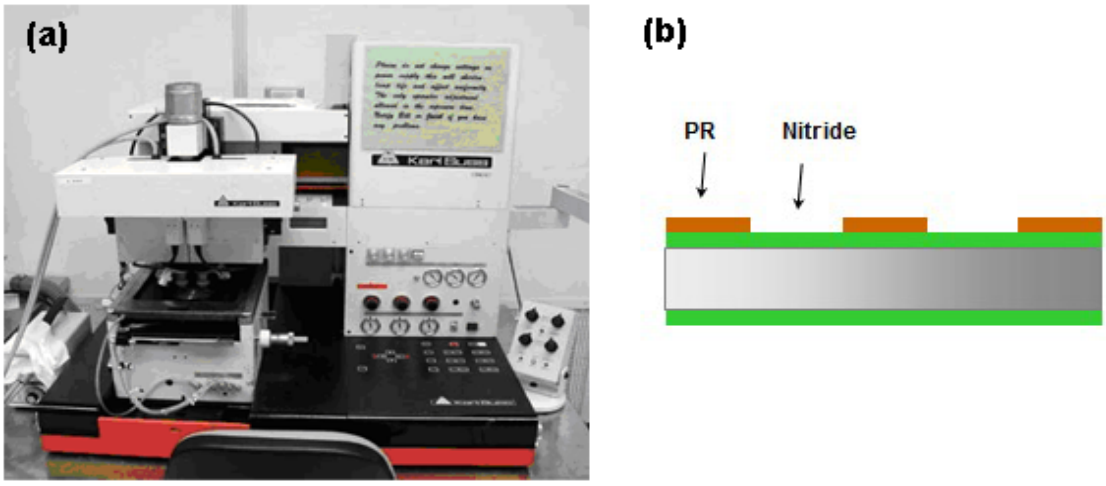

Figure 39. (a) Karl Suss mask aligner* (b) Photoresist has been developed.

1. Log on.
2. Turn on the vacuum pump and mask aligner.
3. Check to see if the filter (3rd slot from the right) is in (for quartz mask) or out (for glass mask).
4. Set the UV lamp to either the filter 'in' setting CI1 (7.5 mW/cm^2) or the filter 'out' setting CI2 (10 mW/cm^2), accordingly.
5. Press the 'load' button. This will cause the stage to move towards the exposure area.
6. Press the 'set exposure time' button and use the arrows to set exposure time (19 seconds). When the time has been entered, press the 'set exposure time' button again.
7. Press the 'align' button. This will cause the stage to move back to the optics.
8. Loosen two silver knobs on the left side of the mask holder and slide the mask holder out.
9. Place the mask onto the holder using the pins to line the mask up and turn the vacuum on. It will hold the mask securely.

* http://www.mrc.utexas.edu/images/equipment/ maskaligner-suss.jpg

10. Slide the holder back into the slot and tighten two knobs.
11. Turn on the TV monitor and the optics lights.
12. Slide the wafer chuck all the way out (vacuum for the wafer chuck turns off), and place a wafer on it lining it up with the 3 pins on the chuck. Slide the chuck back under the mask (vacuum on).
13. To put the wafer in contact with the mask, move the metal lever on the left side of the stage to the up position [The 'WEC' (wafer in contact) lights on].
14. Pull the separation lever towards user to separate the mask and wafer.
15. To align a wafer to the mask, use three micrometer knobs on the sides of the stage. They control the X, Y translations and rotation of a wafer.
16. Move and focus optics using knobs located above the optics. To control / move the view, use the arrow keys.
17. When a wafer is aligned, push the separation lever away to the zero position, so that the mask and wafer will be in contact again.
18. Press the 'exposure' button. This causes the stage to move away from you and expose the wafer.
19. After exposure, the stage will automatically move back out. Wait until the wafer chuck lowers to separate the make and wafer, and the 'WEC' light turns off.
20. Pull the wafer chuck all the way out and remove a wafer.
21. Unload the mask (reverse of the step 8 ~ 10).
22. Turn off the optics lights and TV.
23. Turn off the vacuum pump, the aligner and log off.

AZ425 developer is used to developed UV exposed photoresist AZ5209. Place the wafer in the developer and gently agitate for 1 minute. It results in removing UV exposed area of AZ5209E. Developed patterns are investigated under an optical microscope and then hard-baked in the oven at 120 °C for 30 minutes. It solidifies the

remaining photoresist to make durable protecting layer for the following plasma etching process.

4.3.3. Reactive ion etching

To get rid of silicon nitride through a patterned photoresist layer, reactive ion etching (RIE) technique is used. Chemically reactive plasma is generated under the vacuum by strong RF electromagnetic field. Then ions accelerated by electric filed attack a wafer surface and react with it. For selective etching of silicon nitride, we used mixed plasma of Trifluoromethane (CHF_3: 40 sccm) and Oxygen (O_2: 3 sccm) generated by 182 W power of RF. The etching rate is about 600 Å/min. This process is done using "790 Plasma Therm #2 RIE etcher" [Figure 40 (a)].

1. Log on.
2. Select the chamber to be used. For nitride, select the right chamber (Utilities

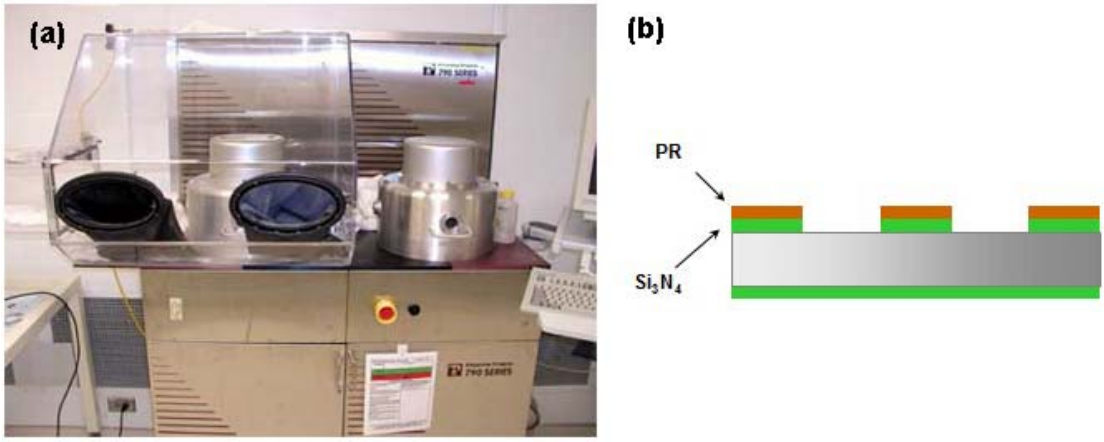

Figure 40. (a) 790 Plasma Therm #2 RIE etcher* (b) Etched nitride thru a patterned photoresist.

* http://www.mrc.utexas.edu/images/ equipment/rie-plasma2.jpg

→ Select Active Chamber → Right).

3. Vent the chamber (Utilities → Vent).
4. Clean the chamber. Wipe all walls, quartz wafer holders, and the graphite susceptor with isopropanol (IPA).
5. Hold the lid to the chamber down and evacuate the chamber (Utilities → Pump Chamber → Low Vacuum). System status will now be 'On & Stanby'.
6. Choose a 10 ~ 30 minute oxygen clean recipe (Pressure: 200 mTorr, O_2: 18 sccm, power: 300 W, Process → Load) and system status will be 'On & Ready'.
7. Run the recipe.
8. Vent the chamber and place a wafer in the chamber.
9. Pump the chamber. (Same as step 5)
10. Choose the nitride recipe (Pressure: 40 mTorr, CHF_3: 40 sccm, O_2: 3 sccm, Power: 300 W). Etching rate is about 600 Å/min.
11. Run the recipe. Slight over-etching is preferred to make sure no residue remaining.
12. Once the run is completed, vent the chamber and remove the sample.
13. Pump the chamber down again and close gate value (Utilities → Close Gates).
14. Log off.

Once RIE is done, photoresist is not necessary because it will be filled off from wafer in the following KOH etching. Piranha cleaning will remove all organic residues by PR. Optional HF cleaning is not required in this step.

4.3.4. KOH etching

As explained earlier, simple KOH solution is the most popular etchant for anisotropic etching of silicon. Typical etching recipes are 30 % of KOH at 80 °C. As shown in the Figure 41, the differences in etch rates for different KOH concentrations are

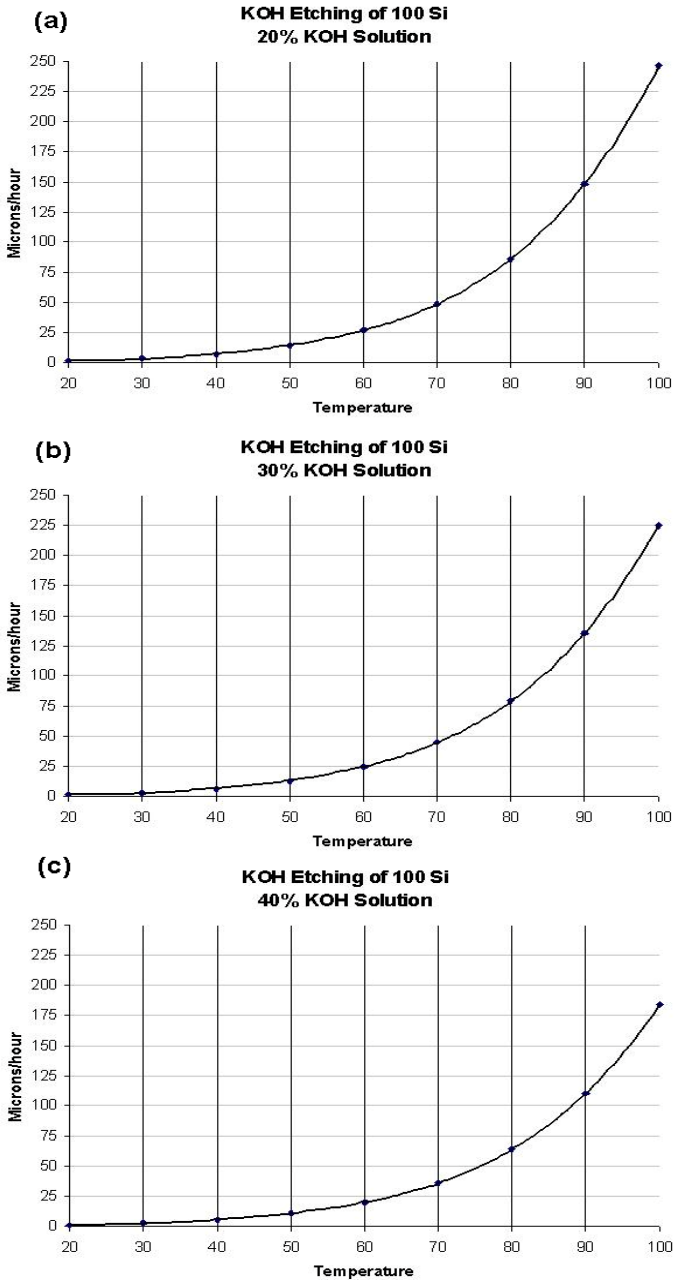

Figure 41. Etching rates of (100) Si at various temperatures in (a) 20%, (b) 30% and (c) 40% KOH solution.*

* http://www.ece.byu.edu/cleanroom/KOH.phtml

small. Thus concentration changes during several hours of process are not a serious consideration. In general, highly concentrated KOH is preferred to obtain smooth surface on low index plane. Agitation of the solution during the process helps removing bubbles, which are stuck on the surface, prevent chemical reactions, and may cause non-uniform etching results. Post KOH processed wafers are contaminated by potassium ions. Because metal / metallic ions are strongly prohibited for the most silicon processing machines, potassium ions should be removed by RCA clean for further processes. KOH etching and RCA cleaning are done in the "H18 Hood".

1. Log on.
2. Fill the cascade rinser and containers with DI water.
3. Prepare the KOH solution. Mix 1600 ml KOH (45%) and 800 ml DI water in the glass container and place it on the hot plate.
4. Put a stir magnet and a thermometer in the solution.
5. Set the temperature 80 °C and wait until the temperature stabilized.
6. Place wafers into the KOH solution. Plenty of bubbles are seen emerging from silicon while etching. Rotate a stirrer to get rid of bubbles.
7. When the etching completed, aspirate KOH solution and rinse the wafers and container for 5 minutes.
8. Prepare the RCA solution. Pour 800 ml of hydrochloric acid (HCl), 800ml of hydrogen peroxide (H_2O_2) and 800 ml of DI water into a quartz tank.
9. Place wafers into RCA solution for 20 minutes.
10. Aspirate RCA solution, and rinse wafers and all containers for 5 minutes.
11. Dry wafers using nitrogen gun.
12. Log off.

Sometimes KOH process was done in the labs in RLM. In this case, etched samples must be considered as "not clean". Therefore it should be also Piranha cleaned in "H18 Hood" before it is transferred to other places.

RCA cleaned samples can be transferred to "H14 Hood" for removing BOX layer under the device. Hydrofluoric acid or pre-mixed buffered oxide etch (BOE) is used for it. BOE is a mixture of hydrofluoric acid and ammonium fluoride (NH_3F) in a 6:1 ratio. Ammonium fluoride is added to maintain HF concentration. Overall and buffering reactions of BOE etching are following;

$$\text{Overall: } SiO_2 + 4HF \rightarrow SiF_4 + 2H_2O, \tag{100}$$

$$\text{Buffering: } NH_4F \leftrightarrow NH_3 + HF. \tag{101}$$

BOE etching can be processed in the HF container. Etching rate is about 1000 Å/min.

4.3.5. Metal deposition

Because silicon is somewhat transparent in the infrared range, thin metallic coating would be preferred to prevent leakage of laser lights to detectors or heating inside bulk materials. Aluminum is a quite common metal and has a low evaporating temperature; it is easy to deposit thin film of aluminum using a thermal evaporator. For not only aluminum, but also various metals such as chrome and gold, the thermal evaporation can be done in the physics cryogenic shop and it provides a precise control of thickness. Maximum thickness is limited by the volume of source boat equipped in the evaporation chamber. The maximum of 2000 Å thickness is thick enough for blocking leakages through cone and wedge targets. However, thicker layers would be required for other applications such as an isochoric heating experiment target. "Varian Sputter" in the Microelectronic Research Center is designated for only aluminum sputtering and has enough capacity for a few micron thick aluminum depositions in several hours. Sputtered aluminum thickness is measured with "Tencor Alpha-Step surface profiler".

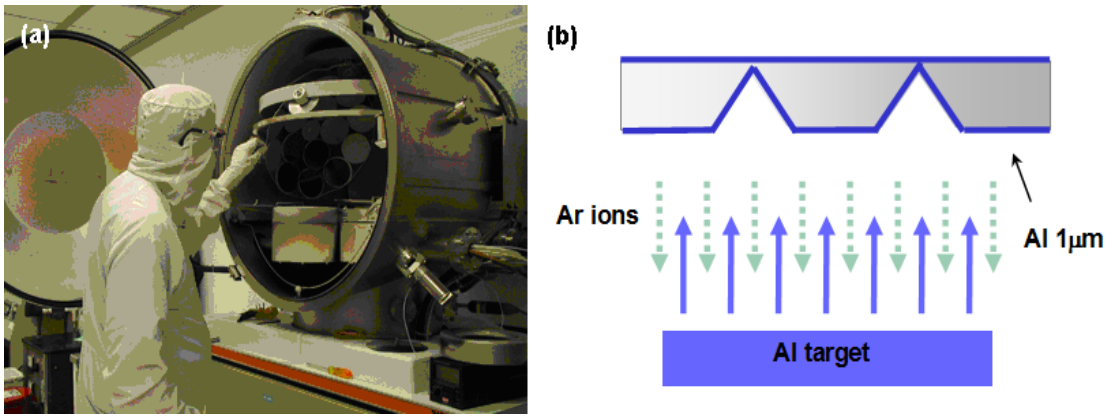

Figure 42. (a) Photograph of Varian Sputter.* (b) Illustration of argon sputtering. Separate runs are required for coating both sides.

1. Log on.
2. Turn on liquid nitrogen. Flip switch up on the back of electronics cabinet.
3. Pull down 'standby' lock in the panel.
4. Rotate knob to 'vent' and wait until system is vented
5. Wear clean gloves and unload the planet.
6. Slip wafers in the planet.
7. Replace planet and spin to make sure wafers remain in place.
8. Rotate knob to 'pump' and push in and up on the door until system begins pumping down.
9. Wait several hours until system is at less than 5×10^{-7} Torr
10. Turn three black valves and the argon valve on in access corridor.
11. Turn fixture drive to 'manual' and slowly increase the drive knob to 90%.
12. Turn on micro-controller pressure gauge.
13. Turn orifice from 'maximum' to 'control'.
14. Turn on backfill 2.

* http://www.mrc.utexas.edu/equipment/sputter-varian.html

15. Micro-controller should read 3 mTorr, tweak the knob on system slightly if pressure needs to be adjusted.
16. Turn on three power supplies (voltage and current) in corridor.
17. Make sure all three lights for electron guns are on, turn all three guns on and increase control of three guns to 48%.
18. Make sure targets are on A-1, B-2, C-3.
19. Wait several minutes to start sputter.
20. Open shutters A-1, B-2, C-3.
21. After deposition, close shutters.
22. Turn currents down and switch guns off.
23. Turn backfill 2 off and turn orifice to 'maximum'.
24. Reduce fixture drive and switch it to 'auto'.
25. Turn off power supplies, three black valves and the argon valve.
26. Vent the chamber and unload samples.
27. After pumping the chamber down again, wait 30 minutes to switch system to 'standby'.
28. Turn off liquid nitrogen.
29. Log off.

After target processing is complete, samples can be inspected under optical microscope and/or scanning electron microscope (Figure 43).

Up to now, I have reviewed step-by-step procedures for major equipments for silicon target fabrication. Using these techniques in this chapter, not only cone and wedge targets but also various targets for other experiments, such as isochoric heating experiment [16] and silicon shock experiment [61], have been also produced. Depending on target geometries and required characteristics for applications, work sequence may be altered and some steps need to be repeated.

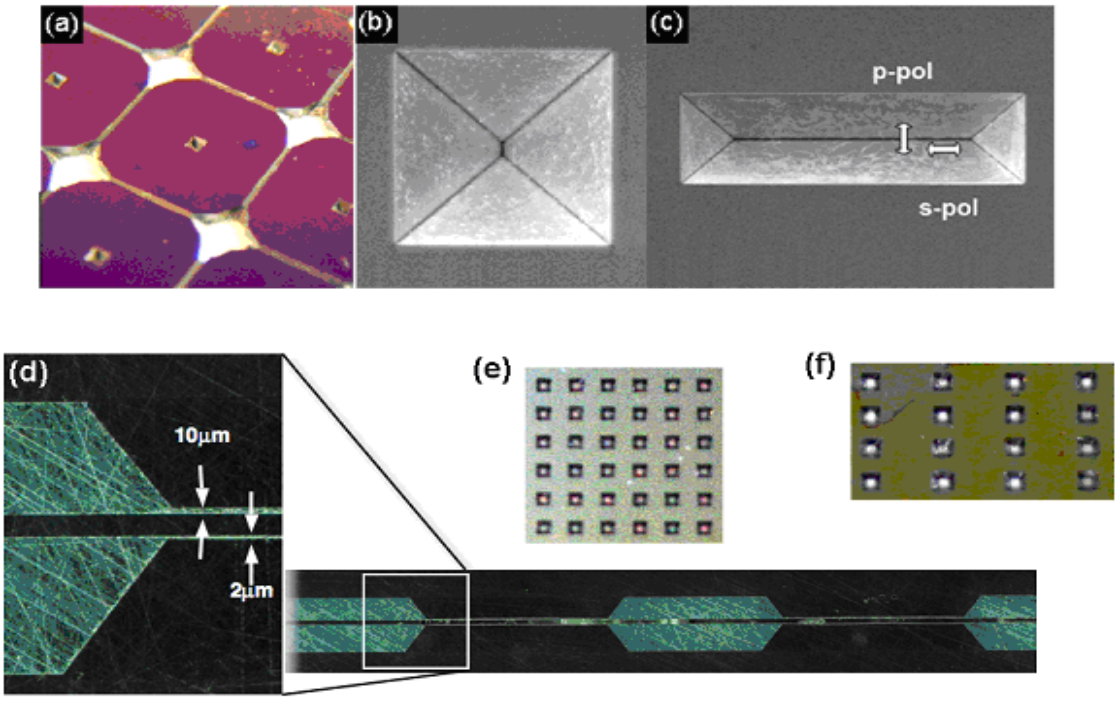

Figure 43. (a) Photo of pyramidal targets. SEM images of (b) pyramidal cone, (c) wedge, (d) side cut of double layered target for isochoric heating experiment, (e) silicon shock experiment target (10 μm thick), and (f) aluminum reflectivity measurement target (100 nm thick).

CHAPTER 5. HOT ELECTRON GENERATION FROM MICRO-TIPPED CONE AND WEDGE TARGETS

In this chapter, it will be discussed the results of experiment for x-ray spectroscopy in laser – cone target interactions. We have explored hot electron production in re-entrant targets etched into silicon wafers by measuring the $K\alpha$ and hard x-ray emission from these targets, some of which have been combined with a $K\alpha$ converter layer. It was found that there exists the target and polarization configuration that maximizes high-energy electron and hard x-ray production, when $K\alpha$ yield is minimum. These results are consistent with two-dimensional PIC simulations, which suggest that radiation pressure compression can be important at the tip of a cone in enhancing $K\alpha$ yield. Comparing the experimental results with simulations we conclude that, for the rather large opening angle cones used in our studies, electron guiding is not important in these structures. Instead hot electron production variation with target and incident polarization can be explained through standard collisonless heating models such as vacuum heating, resonance absorption, and $\boldsymbol{j} \times \mathbf{B}$ heating.

5.1. TARGET CHAMBER SETUP

Figure 44 is schematics of a clamshell target chamber in a THOR laser target room. Laser pulse of 600 mJ, 35 fs were focused into the re-entrant targets with an F/#2.8, 45° off-axis parabola with a peak intensity of $2 \pm 0.5 \times 10^{19}$ W/cm^2. Flat titanium foil, cone and wedge targets were irradiated. For direct comparisons, titanium foil is attached on the back surface of silicon cone and wedge target. The THOR does have some low level pre-pulse, however, previous angle scan measurements of hard x-ray production have been performed, and we have determined, through comparison with the usual resonance absorption formulas, that the pre-plasma scale length is of the order of

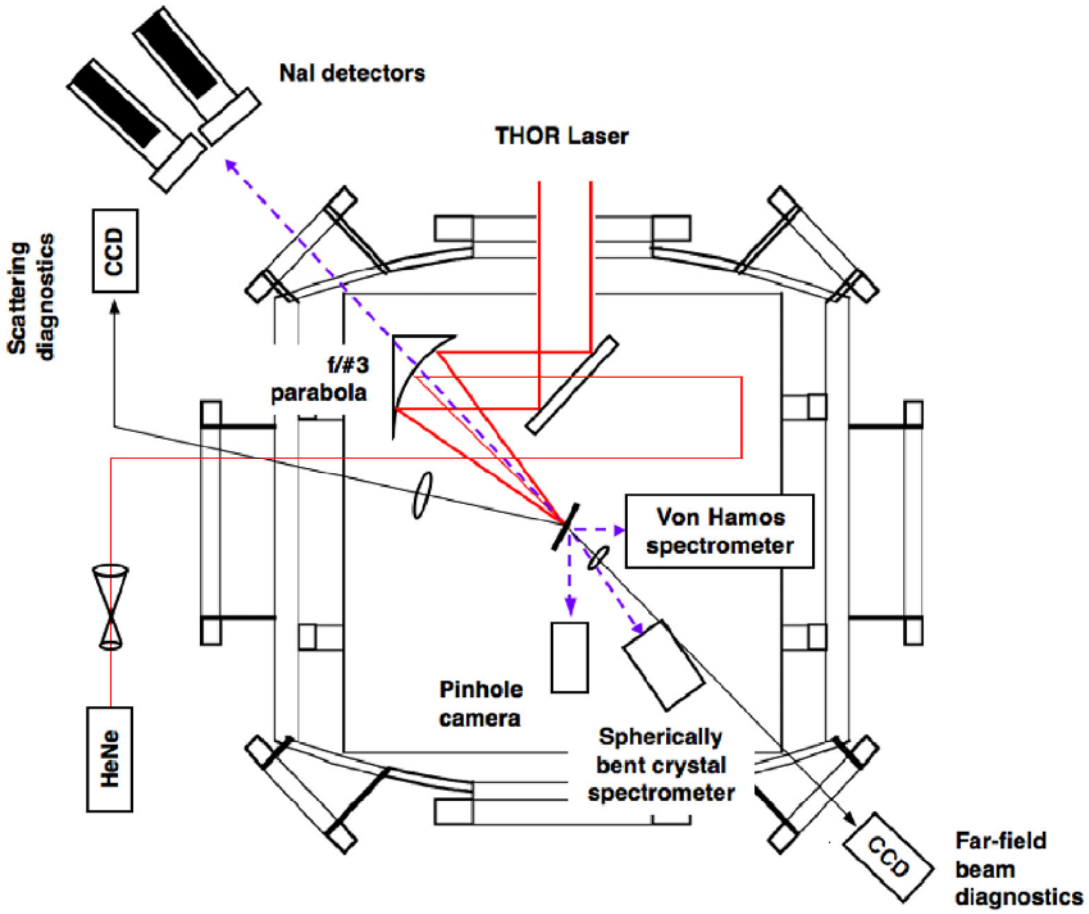

Figure 44. Solid target chamber setup. Microscope objected lens is used for the far-field beam diagnostics. It is mounted on the mechanical arm of a vacuum feed-thru and can be out of the beam pass while the laser is firing.

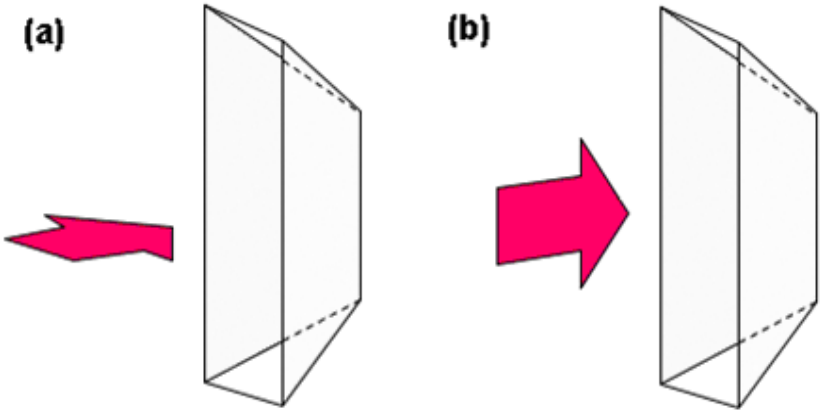

Figure 45. Wedge orientation with linear polarized laser light. (a) *p*- and (b) *s*-wedge. In the experiments, target orientation is rotated instead laser polarization.

2 ~ 3 μm. We therefore concluded that the geometry of our micron-scale cone and wedge targets survives largely intact up to the time of arrival of the main pulse. For precise target alignment and ensuring reproducibility in the electron production, HeNe beam was set coaxial to the main laser beam. By monitoring scattered and back reflected HeNe lights using a scattering diagnostic and removable screen, precise *z* and *x*-*y* target positions respect to the laser focal spot is accomplished.

Inside the target chamber, a pinhole camera and a spherically bent crystal was installed to image the spatial extent of K_α emission from the rear side of the target. Pinhole camera equipped 20 μm of pinhole and a beryllium filter to block photon below 2 keV energy. A spherically bent crystal was oriented to reflect the seventh-order Bragg reflection of 4.5 keV and Kodak RAR 2492 film was located on the focal plane of the crystal and demagnification was 1.15. A Von Hamos spectrometer was also installed to measure the integrated yield of the titanium *K*-shell line emission. The crystal reflectivity was calibrated at a synchrotron [73], so the absolute number of photons could be derived using the calibration table of the Kodak RAR 2492 film employed as the detector [74]. To detect bremsstrahlung x-rays produced by the hot electrons, we placed three NaI x-ray detectors outside the target chamber at 45° from the target back surface

normal. Three different filters were installed in front of the detector; 3.2 cm and 4.8 cm thick lead and 9.5 cm thick copper filters were chosen to measure x-ray yield in the 700 ~ 1200 keV photon energy range. These x-ray diagnostics served to probe two distinct energy ranges of electrons. Based on *K*-shell ionization cross sections, electrons in the range of 50 ~ 300 keV are responsible for the $K\alpha$ signal from titanium. Hotter electrons in the range of ~ 1 MeV are responsible for producing the bremsstrahlung seen by the hard x-ray detectors.

5.2. SILICON CONE AND WEDGE TARGET DATA

5.2.1. $K\alpha$ source imaging

A typical x-ray film image is presented in Figure 46 (Top). Because of a low reflectivity of crystal, 15 ~ 20 shots had been accumulated to ensure a good exposure on the film. Horizontal axis gave spectral information of radiation, so the left and right dots represent titanium $K\alpha_1$ and $K\alpha_2$, respectively. Vertical axis represents one-dimensional spatial extents of source.

The film is digitized using a 16 bit Konica Minolta DiMage Scan Dual IV film scanner. From the scanned image, a line-out in vertical direction is taken. The spatial profile of titanium $K\alpha_1$ emissions from cone and *p*-polarized wedges are plotted in Figure 46 (Bottom). For comparison, spatial profile of $K\alpha$ emission from flat titanium foil is also presented. In flat targets we observe side peaks which are ~35% of the central spot amplitude surrounded by a millimeter size of plateau of signal. Since electrons escaping target creates strong sheath fields on surfaces, low energy electrons that hardly overcome this potential return back to cold material and contribute $K\alpha$ emissions. These processes are illustrated in Figure 47.

This apparent fountaining of electrons in flat targets is absent from both cone and wedge targets. However, the central $K\alpha$ feature is comparably sized when either flat

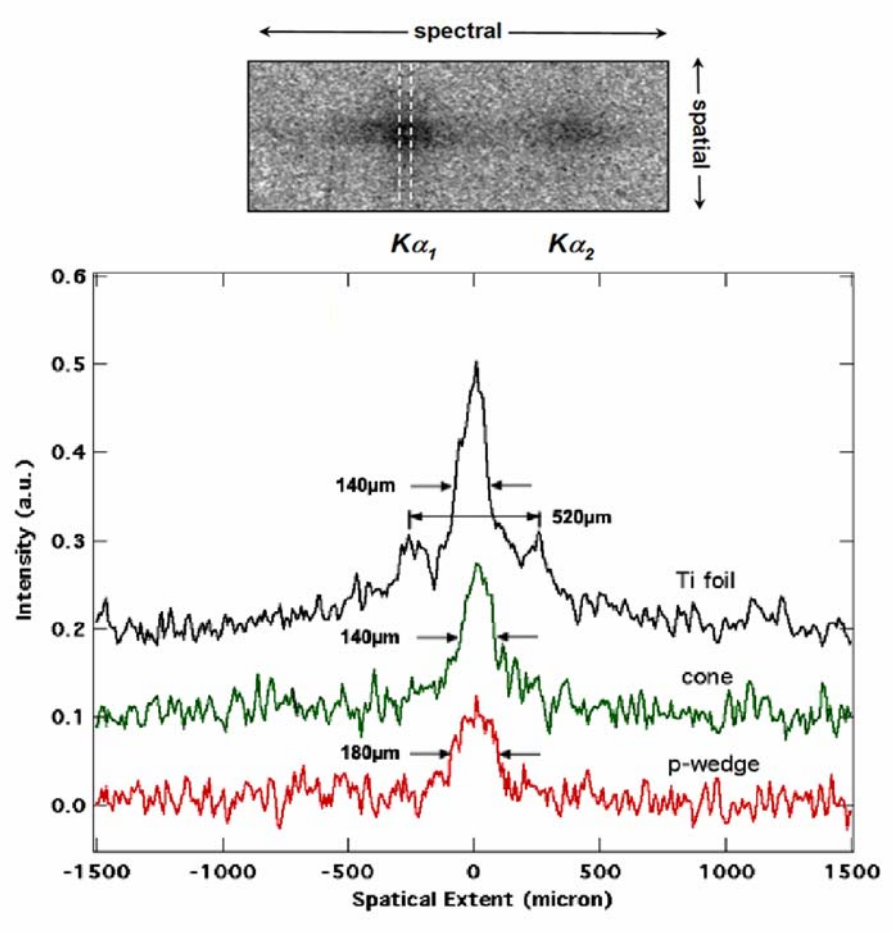

Figure 46. (Top) Typical image of scanned x-ray film. Titanium $K\alpha_1$ and $K\alpha_2$ source were recorded. Spatial extents for $K\alpha_1$ are given by vertical lining out white regions. (Bottom) Comparison of x-ray output from wedge and cone targets. Spatial profiles of $K\alpha_1$ emissions from flat titanium foil, cone and *p*-polarized wedge.

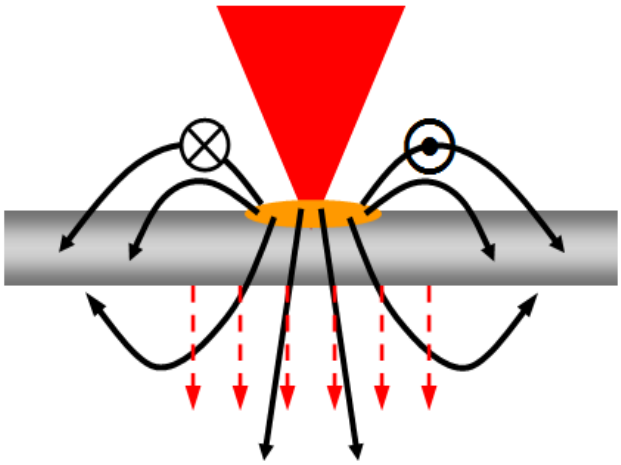

Figure 47. Illustration of electron fountaining effects. Solid lines represent electron trajectories and red dotted lines are quasi-static electric field created by charge separation.

foil or cone targets are irradiated. The full widths at half maximum of central peaks are roughly 140 μm. $K\alpha$ source size distribution with and without pre-plasma had been studied earlier [9]. Existence of pre-plasma increase source size and it is a factor of about 10 times larger than laser spot. It should be noted that the THOR laser does have some low level pre-pulse and the pre-plasma scale length is of the order of 2 ~ 3 μm [63]. Considering a 10 μm laser spot size, x-ray source size is consisting with previous studies. The *p*-polarized wedges appear to exhibit about 30% larger central feature (~ 180 μm). It implies that *p*-wedge more spreads out electrons of which energy effectively producing vacancies in the titanium *K*-shells. This difference in source size may be attributable to the difference in heating mechanisms in each case, as discussed in the later sections.

5.2.2. $K\alpha$ yield measurement

A typical x-ray film image from the Von Hamos spectrometer is presented in Figure 48 (Top). To ensure to exposure in overall spectral region covered by spectrometer, 40 ~ 50 shots were accumulated.

Analyzing this film requires more attentions to get quantitative information about the number of x-ray photon numbers. It is possible due to a previous calibration of the crystal reflectivity [73] and x-ray film [74]. From the digitized image, a horizontal line-out is taken and converted into optical density (OD). Horizontal axis is converted into wavelength (or photon energy). It is linearized using density exposure relation and the backgroup is subtracted. After considering filter transmission, crystal reflectivity and solid angle of each wavelength, optical density is converted into the absolute number of photon per shot, solid angle and wavelength interval.

Titanium $K\alpha$ spectra yield from cone and wedge targets of both polarizations are obtained by lining out between dotted area and plotted in Figure 48 (Bottom). *S*-polarized wedges yield the strongest titanium $K\alpha_1$ and $K\alpha_2$ signals, while *p*-polarized wedges very clearly give the weakest. The $K\alpha$ yields from the cones were intermediate to those of the two polarizations in wedge targets. Integrating over the 1/e width of the $K\alpha_1$ peak yielded 3.3×10^9 photons/shot/srad, 0.9×10^9, photons/shot/srad, and 2.4×10^9 photons/shot/srad for *s*-, *p*-polarized wedge and cone targets respectively.

These data suggest that the hottest electron temperatures are produced in the *p*-wedges but that this target configuration is not optimum for producing electrons in the 50 - 300 keV range. This result initially appears to be contradictory, as one would expect that if resonance absorption dominates in the *p*-wedge case, both $K\alpha$ and bremsstrahlung signals should be highest in that configuration.

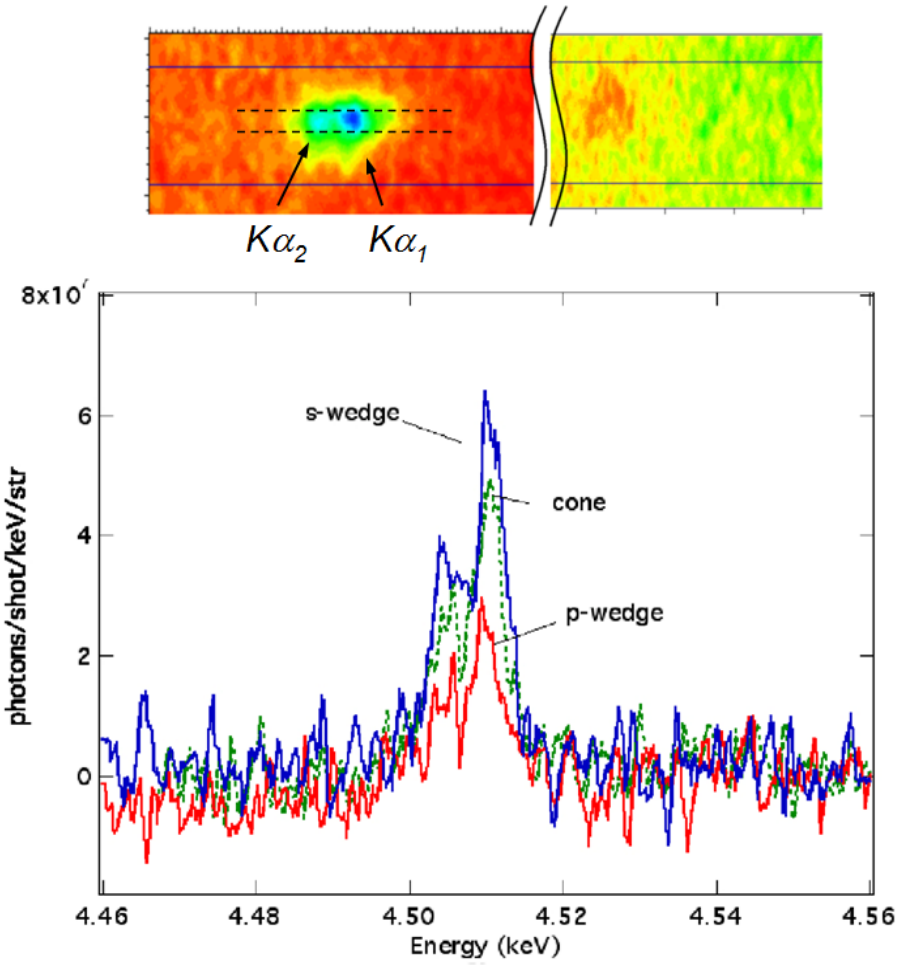

Figure 48. (Top) Typical image of scanned x-ray film. Titanium $K\alpha_1$, $K\alpha_2$ and $K\beta$ source were recorded. (Bottom) $K\alpha_1$ and $K\alpha_2$ emission peaks are lined out.

5.2.3. Hard x-ray yield measurement

Abundant hard x-ray emission was also observed by the NaI detectors. X-ray yield data from these three detectors are plotted in Figure 49. Here the total deposited x-ray energy in the detector per shot is plotted versus the cut-off energy of each filter. In contrast to the $K\alpha$ measurements, the hard x-ray yield observed from *p*-wedges was about three times higher than from *s*-wedges and twice as high as that from the cones. It is clear that in the *p*-polarized wedges, significantly more energetic electrons are heated and contribute to hard x-ray production than in the *s*-polarized wedges. The error bars arise from the standard deviation of signal from multiple shots. The larger error bars in the *p*-wedge data most likely result from an increased sensitivity to pointing for these targets.

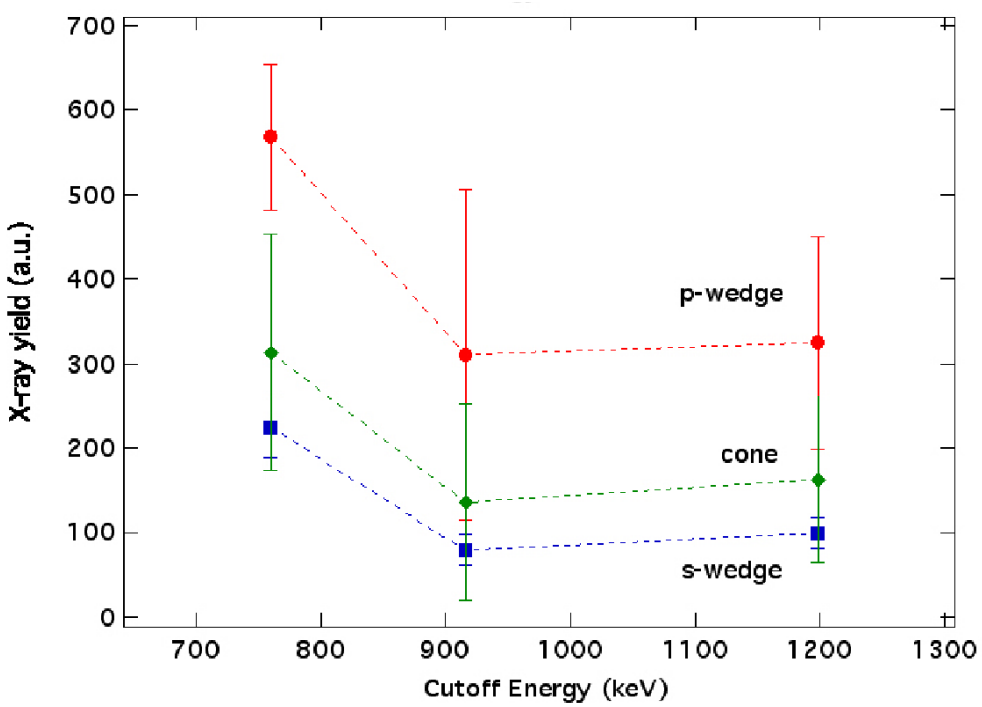

Figure 49. Deposited x-ray photon energy on the filtered NaI detectors. 3.175 cm Pb ($1/e^2$ transmission cutoff: 760 keV) and 4.76 cm Pb (916 keV) and 9.5 cm Cu (1198 keV) filters are used.

$K\alpha$ and bremsstrahlung x-ray data suggest that the hottest electron temperatures are produced in the *p*-wedges but that this target configuration is not optimum for producing electrons in the 50 ~ 300 keV range. This result appears to be contradictory, as one would expect that if resonance absorption dominates in the *p*-wedge case, both $K\alpha$ and bremsstrahlung signals should be highest in that configuration.

5.3. PARTICLE-IN-CELL SIMULATIONS

5.3.1. PICLS simulation

To understand this apparent discrepancy of x-ray spectra in the different energy ranges, we conducted particle-in-cell simulations of these reentrant target configurations. Experimental conditions were simulated using PICLS, a 2-dimensional particle-in-cell (PIC) code with a fully relativistic collision model and a Monte Carlo calculation of bremsstrahlung [19] by Yasuhiko Sentoku at the University of Nevada at Reno. The target is modeled as a wedge-shaped dip in a 6 μm-thick slab of target material consisting of fully-ionized deuterium of density $n_0 = 4 \times 10^{22}$ cm^{-3}. Simulations conditions were chosen to coincide to the experimental conditions; laser light with a peak normalized laser vector potential of $a_0 = 2$ is incident from the left hand side and centered on the wedge. As in the experiment, the wedge angle is 71º.

The simulation was run for both *s*- (perpendicular to plane) and *p*- (parallel to plane) polarization configurations. We find that the principal hot electron absorption mechanisms are vacuum heating [3], in which electrons are pulled from the surface of a target by *p*-polarized light and returned during the laser cycle back to the overdense plasma with energy comparable the laser ponderomotive energy, and $\boldsymbol{j} \times \mathbf{B}$ heating [2], which results from electrons accelerated forward into a target by a combination of their transverse electric field driven motion and the forward motion created by the strong magnetic field of the high intensity light pulse.

The energy density ($\varepsilon\, n/n_0$) of hot electrons 60 fs after pulse arrival (i.e. 20 fs after 40 fs of laser irradiation ends) for each case is plotted in Figure 50. Very distinct results are predicted for the two polarizations. In the case of *p*-polarization [Figure 50 (a)], hot electrons escape the interaction region and stream through the target material both normal to the wedge wall planes and parallel to these planes, heating the background material along their path. Most electrons are accelerated into the target bulk [denoted region II in Figure 50 (a)], normal to the wedge surface, which is a consequence of the vacuum heating and resonance absorption mechanisms. These energetic electrons mainly contribute to the generation of abundant bremsstrahlung x-rays from the *p*-polarized wedges. In addition, the PIC simulation indicates that a small fraction of the hot electrons are guided toward the tip along the wedge surfaces (region III). Compared to region I, where no electron stream is observed, it is clear by tracking electron trajectories

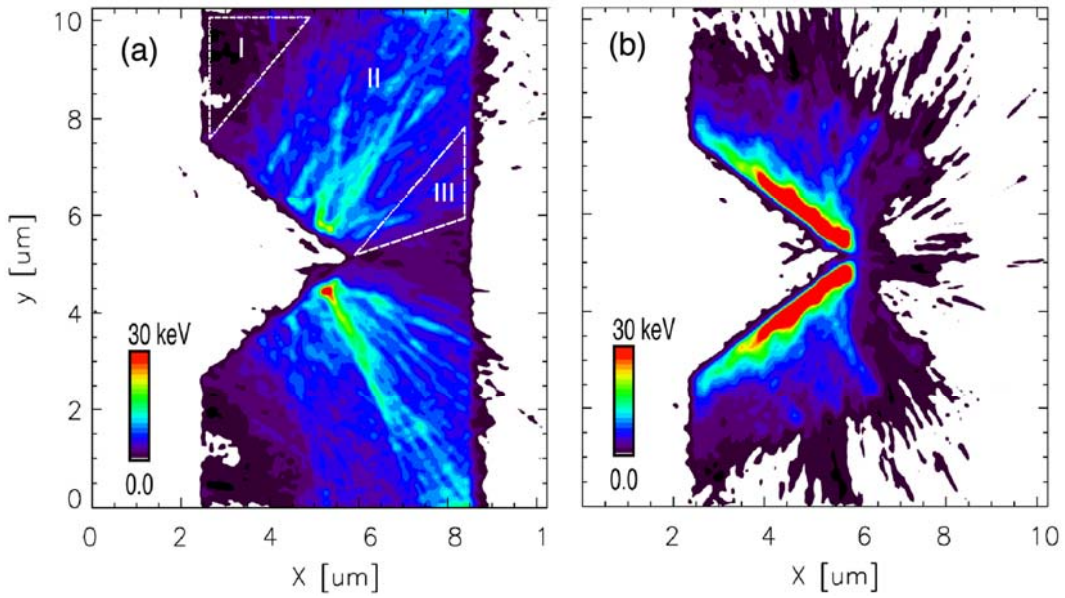

Figure 50. Results of PICLS simulation for (a) *p*-polarized and (b) *s*-polarized wedge targets. For both, plasma energy density ($\varepsilon\, n/n_0$) at 60 fs after pulse arrival is depicted. Number of energetic particle is normalized by initial number of particles. The initial target extends from 2.5 μm to 8.5 μm and white indicates regions of zero energy density, either through lack of material or lack of excitation.

in the simulation that region III is heated by some electrons guided along the wall of the opposite wedge surface. In other works, the angle of incidence at which surface guided electrons are inferred [75] or predicted [5, 76] to dominate is larger than our fixed 55º angle of incidence, so this small fraction of focused electrons in our case does not necessarily contradict those earlier works.

In the case of *s*-polarization [Figure 50 (b)], overall coupling of laser energy to the target is greatly reduced, resulting in less laser energy being coupled into hot electrons. Compared to the *p*-polarized wedge, no significant electron stream is observed toward the target bulk (produced in the *p*-polarized case by vacuum heating) or along the wedge surfaces (a result of $\boldsymbol{j} \times \mathbf{B}$ heating). This is consistent with our hard x-ray yield measurement. The absence of $\boldsymbol{j} \times \mathbf{B}$ heating by the current accelerated along the wedge surfaces is also consistent with a previous simulation, which showed almost no magnetic field normal to the laser polarization plane [19]. However, a high energy density is produced near the wedge tip by another effect. Because of the low laser energy absorption in the *s*-wedges, the wedge surfaces reflect more laser light and result in higher radiation pressure on the target surface. The simulations show that this compresses and heats the region near the tip, leading to a higher energy density there. We find in the simulations that a sizable fraction of the electrons near the *s*-wedge tip are in an optimal energy range (< 200 keV) for generating *K*-shell vacancies in titanium.

Hot electron spectra from *p*- and *s*-wedges generated from the PIC simulations are presented in Figure 51 (a). Because of the high laser intensity and short pulse duration used in our simulation, we expect a small scale-length of plasma and that the absorption will occur within a sharp boundary. The electron oscillation energy in the transverse field of this incident relativistic laser pulse is given

$$\varepsilon_p = (\gamma_t - 1) m_0 c^2 \qquad (102)$$

where $\gamma_t = \left(1 + I\lambda^2 / 1.37 \times 10^{18}\right)^{1/2}$, can be used to estimate roughly the characteristic heated electron temperature [2]. For our simulation condition, ε_p = 630 keV.

Calculated hot electron temperatures from the electron spectra for p wedges are higher than in *s*-wedges, 900 keV and 650 keV respectively. The yield of hot electrons above 1 MeV is significantly lower when *s*-polarization is employed. The higher temperature and higher hot electron yield for the *p*-wedge results from the predominance of the two heating mechanisms described. Using the built-in Monte Carlo code in the PICLS, a bremsstrahlung spectrum from each target is also calculated and presented in Figure 51 (b). The simulation shows quantitative consistency with our experimental data, predicting a 3 to 4 times higher hard x-ray yield around 1 MeV from the *p*-wedge than the *s*-wedge.

Also evident in Figure 51 (a) is a range of electron energies (75 keV ~ 500 keV) over which the *s*-wedge target produces significantly more electrons than the *p*-wedge case. This feature of the simulated spectra fully predicts the higher level of titanium $K\alpha$ photons observed in experiment. Electrons in this energy interval have a range of from several tens to several hundreds of microns [76], and cross sections for $K\alpha$ production from equal to several times greater than electrons of higher energy [77]. Thus the greater energy absorption in the *p*-wedge case is "wasted," from the standpoint of $K\alpha$ generation, on overly energetic electrons. This explains the apparently contradictory experimental data that *s*-wedges give the strongest $K\alpha$ signal but the lowest hard x-ray signal.

Furthermore, absorption mechanisms associated with *p*-polarization, such as vacuum heating or resonance absorption; tend to accelerate electrons normal to the front target surface. In the case of a wedge geometry, this leads to hot electrons fanning out more from the central region, as seen in Figure 50 (a). This seems to be corroborated by the spatial profile data of Figure 46. Although spatially resolved x-ray data of the *s*-wedge targets were not taken, the $K\alpha$ generation of the cone targets is expected to give intermediate conditions between *s*- and *p*-wedges, and the spatial extent of $K\alpha$ for the cones is indeed less than that of the *p*-wedges. It is also important to note that the several micron thickness of silicon and 25 μm thickness of titatnium, together with the

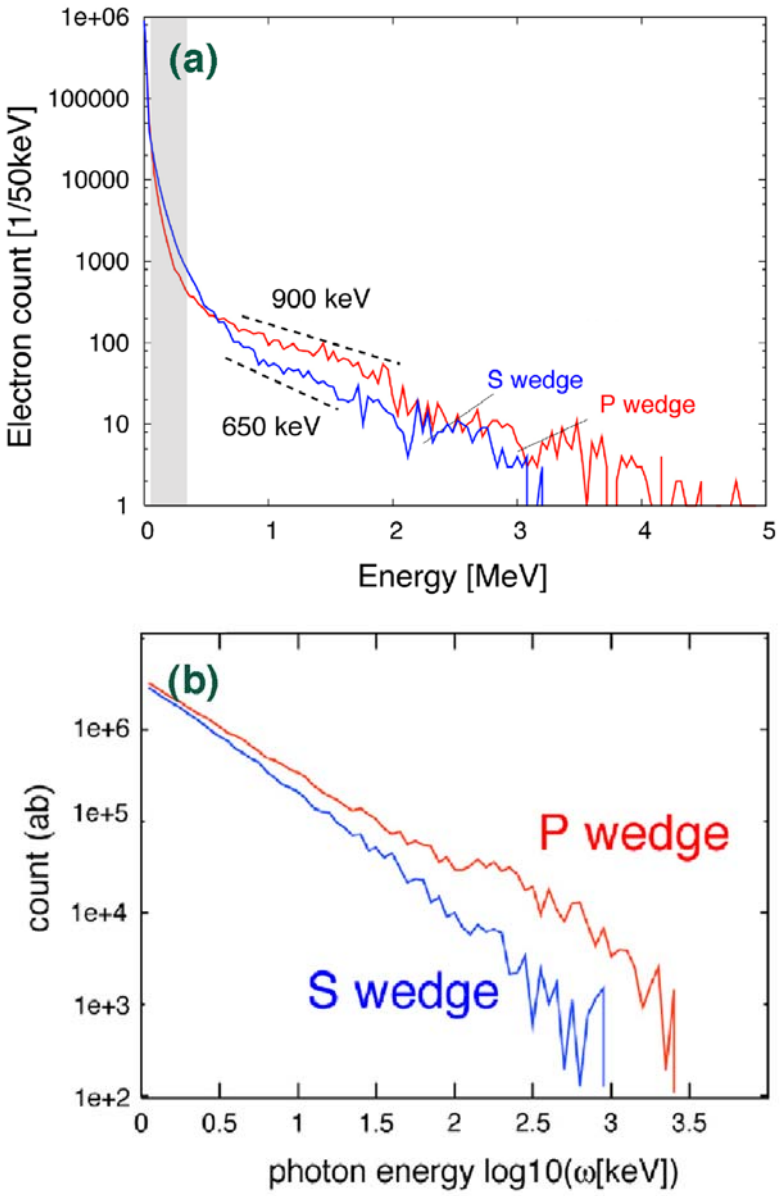

Figure 51. (a) Simulated hot electron spectrum from *p*- and *s*- wedges. The region of energies responsible for enhanced K_α emission in the *s*-wedge case is highlighted. (b) Bremsstrahlung spectra at 45º from target rear surface normal predicted from built-in Monte Carlo simulation

long range of >100keV electrons imply that the K_α generated in the target will have a spatial extent much greater than the few microns of the simulation area, regardless of wedge orientation.

5.3.2. OOPIC simulation

It should be noted that our estimated pre-plasma scale length of 2 ~ 3 μm was not included in the PICLS simulations. Such a pre-plasma is unsuitable for the vacuum heating mechanism, favoring instead resonance absorption. However, the two mechanisms are similar in that both accelerate electrons normal to the surface along the plasma gradient, and both are active only in the case of *p*-polarization [2]. However, to ascertain if pre-plasma formation did affect the qualitative nature of our modeling results, we performed a series of complementary PIC simulations using the PIC code OOPIC [78] in which we examined the effects of pre-plasma. This 2D code permitted us to perform a series of runs to look at the qualitative effects of pre-plasma in a 2D cone, i.e. a

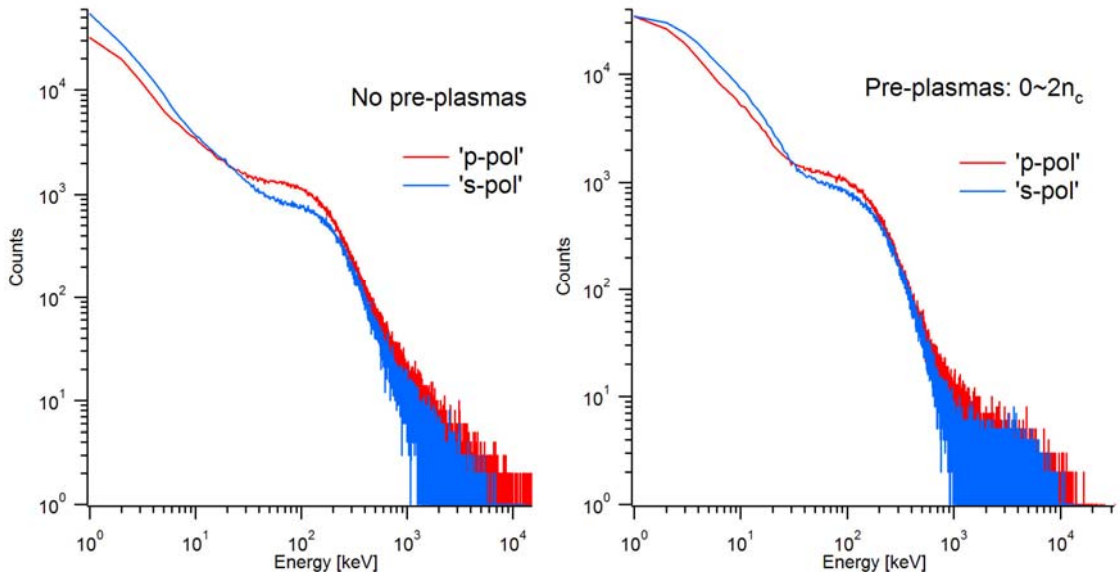

Figure 52. Simulated hot electron spectra in wedge targets (left) without and (right) with pre-plasma.

wedge, for the two polarizations. We modeled a simple cone, as was done with PICLS and we modeled the same cone geometry with a 10 μm linear plasma scale length in the cone, rising from 0 to $2n_{crit}$ in the cone tip. The cone itself was composed of hydrogen plasma of density $8n_{crit}$. We find that the qualitative predictions are the same between this code and the more extensive PICLS runs in the case of no pre- plasma. The *s*-polarized spectrum had more electrons at the mid energy range while the *p*-polarized electron spectrum was more pronounced at higher energy. When the simulation included the pre-plasma, the results turned out to be quite similar, though the crossing point in the electron spectrum between *s*- and *p*-polarization was at a somewhat higher electron energy. From these simulations we have concluded that the findings of the PICLS simulations are most likely applicable to our experimental conditions, which had a lower level of pre-plasma than simulated with OOPIC.

5.4. UNR GOLD CONE DATA AND SIMULATION

5.4.1. Pinhole camera imaging

X-rays from free standing 10 μm gold pyramid targets made in University of Nevada at Reno (see Figure 22), were imaged using a pinhole camera with 20 μm diameter pinhole. To block scattered lights and optical emissions from the plasma, 100 μm of beryllium foil was equipped as a filter. This foil provides a transmission cutoff at around 2 keV. Because of limited number of targets, we could not integrate much signal on DEF film as silicon targets. Instead, we utilized Kodak Biomax MS (BMS) film and intensifying screen. BMS film itself is quite sensitive at blue lights and the intensifying screen behind the film converts x-rays into blue photons. Energy difference in x-ray and visible light allows a single x-ray photon generates many blue photons. As a result, BMS film / screen provides a great sensitivity and a couple of shot accumulation are required for good exposure. However, the resolution of image is limited by the thickness of film (~ 0.5 mm).

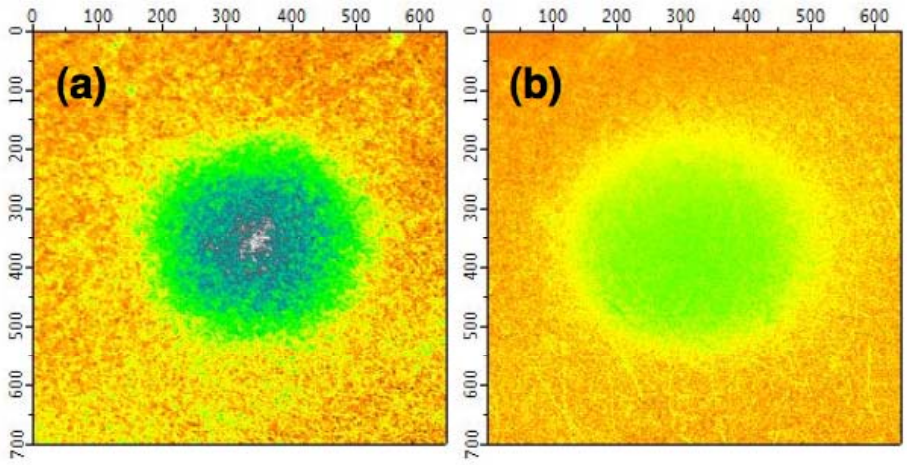

Figure 53. X-ray pinhole camera images for (a) 10 μm free-standing gold pyramidal cone and (b) 10 μm gold foil.

Figure 53 depicts pinhole camera data from gold pyramidal cone and the flat foil with the same thickness. The FWHM diameters are 341 μm and 600 μm and total x-ray yield and peak intensity of the cones are about 4 times and 2 times of the flat, respectively. One should be noted is that x-rays recorded on this film were filtered with only a low cutoff energy beryllium foil and all photon above 2 keV were presented on it. Since there is no energy dependent calibration data for the film, it was hardly extracting quantitative analogies for specific wavelength of x-ray spectra. However, qualitatively, it is quite obvious that the data indicate that a cone creates hotter plasma and produce greater x-ray photons in more confined region comparing to flat target.

5.4.2. PICLS simulation

PICLS simulations for gold targets were also done by Yasuhiko Sentoku. Initial conditions ($n_0 = 4 \times 10^{22}$ cm^{-3}, $a_0 = 2$) were the same as the wedge cases. Energy densities for the cone and flat targets at 60 fs are shown in the Figure 54. It is clear that for the cone target, the higher density energy regime is created at around the tip. The

high concentration of laser produced hot electrons around the center in the case of the micro-shaped target. On the other hand, in the flat target, the hot electrons quickly spread in the flat target, resulting in a low average energy, but entire materials in the simulation box are quite uniformly heated up. The maximum temperature is about three times higher in the shaped target than that of the flat, and the higher temperature is continuing in a longer time scale. These results are very consisting with the pinhole camera data; brighter x-rays from the cone and bigger emission diameter for the flat.

5.5. SUMMARY

We have studied relativistic laser interaction with reentrant wedge and cone targets produced by anisotropic etching of silicon. Around and over 1 MeV energy range, *p*-wedges produced higher x-ray yield than *s*-wedges, however in keV ranges, the opposite was observed. These results are quite consistent with the predictions of 2D PICLS simulations. These experimental and simulation results support also anisotropic heating, which was observed in 3D-PIC simulation of cone focusing. X-ray output from the square-based cone targets for both the keV and MeV photon energy ranges fell between that of *s*- and *p*- wedges, suggesting that this type of cone combines the effects of the two 2D cases. Experiment and simulation for free-standing cone target showed a potential to create higher energy and density plasma at the center of this type of target.

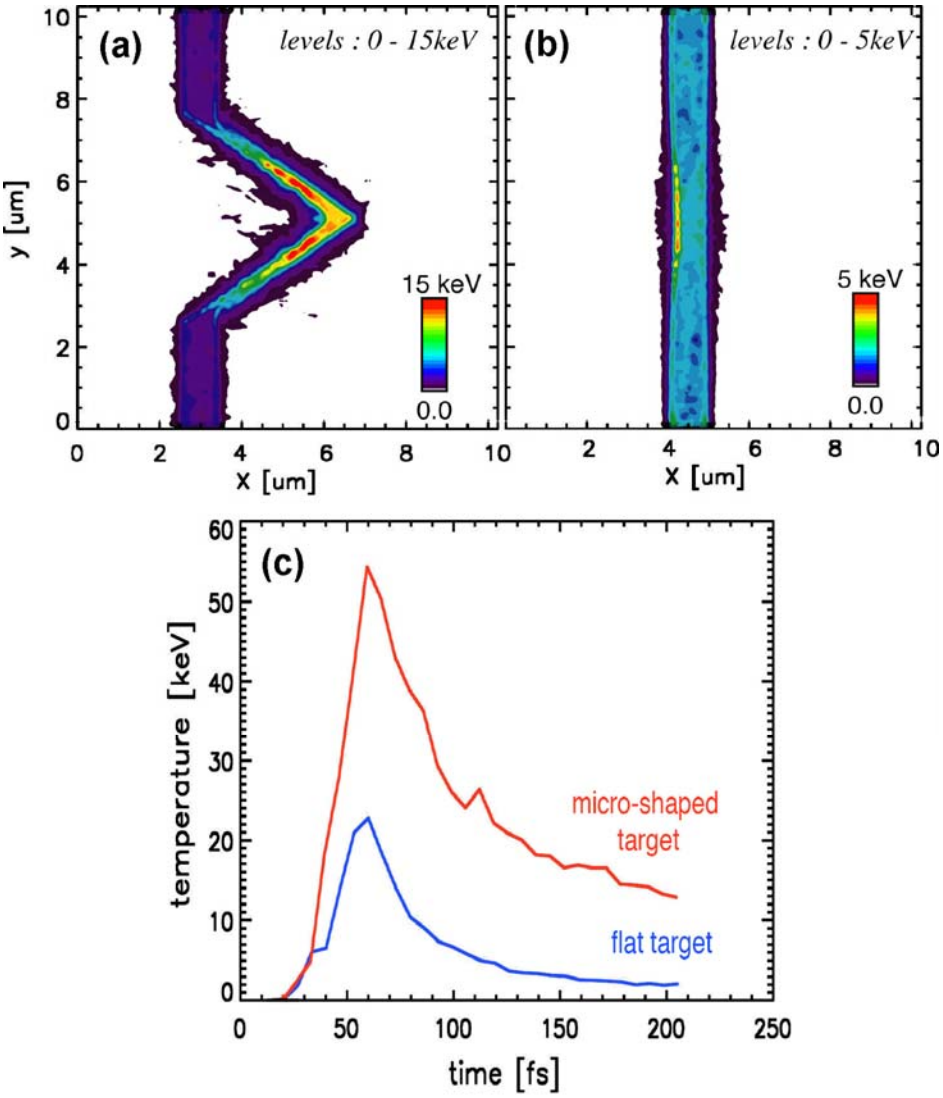

Figure 54. Electron energy density ($\varepsilon\, n/n_0$) [keV] for (a) the cone and (b) the foil targets at 60 fs. (c) Time history of average electron energy at the target center.

CHAPTER 6. OBSERVATION OF ELECTRON TRANSPORTS IN VARIOUS TARGETS USING COHERENT TRANSITION RADIATION

In this chapter, I will discuss that observation of transition radiation at the target boundary to study details of fast electrons acceleration, transportation, and dephasing [34, 35, 38, 61]. First part of chapter present recent experimental results on 800 nm coherent transition radiation and bremsstrahlung x-ray data from planar aluminum targets and compare these measurements with theoretical calculations. We find that electron micro-pulses with about 300 keV electron temperature accelerated by resonance absorption were injected to the target once per laser cycle. These hot electrons are transported through the target in a very small beam, of order of the laser spot size, with limited divergence. We also examined CTR from targets composed of silicon pyramid / wedge shaped targets copper cone targets. From these targets, we observe strong effects from the quasi-static electromagnetic fields created on target surfaces on the electron transport near the tips of the micro shaped targets. CTR from the tip of conical targets showed that focusing the laser light at the entrance of the cone mitigates high level of pre-plasma and enables the cone target to actually do what it is predicted to do. It also allows for the laser to spread on a longer surface possibly enhancing the surface guiding of the electrons towards the tip of the cone.

In the second part of chapter, we present measurements of 400 nm CTR emission from the rear surface of aluminum foils. We observe two distinct lobes emerging simultaneously in the CTR emission pattern, which we attribute to resonance absorption and $\boldsymbol{j} \times \mathbf{B}$ heating. Previously, some evidences for multiple hot electron beams from solid targets have been reported. Santala *et al.* observed indirect evidence for these two mechanisms by measuring gamma ray generation from solid targets [23]. More recently Ter-Avetisyan *et al.* observed two distinct beams of Cerenkov radiation from hot

electrons traversing a transparent layer on the backside of their solid target [24]. However, by observing CTR, we found more detailed information about each electron beams. Along with ballistic electron transport model, we have revealed the relative efficiency of these two heating mechanisms, finding that about one order of magnitude more hot electrons were driven by resonance absorption than by $\boldsymbol{j} \times \mathbf{B}$ heating, and that the hot electron temperatures of each population were 1 MeV and 1.5 MeV respectively. Experimental findings are also confirmed by three dimensional PIC simulations.

6.1. EXPERIMENTAL CHAMBER SETUP

Figure 55 shows an optical layout of a solid target chamber in a THOR laser target area. The THOR laser pulse of 700mJ and 40fs was focused on target using an

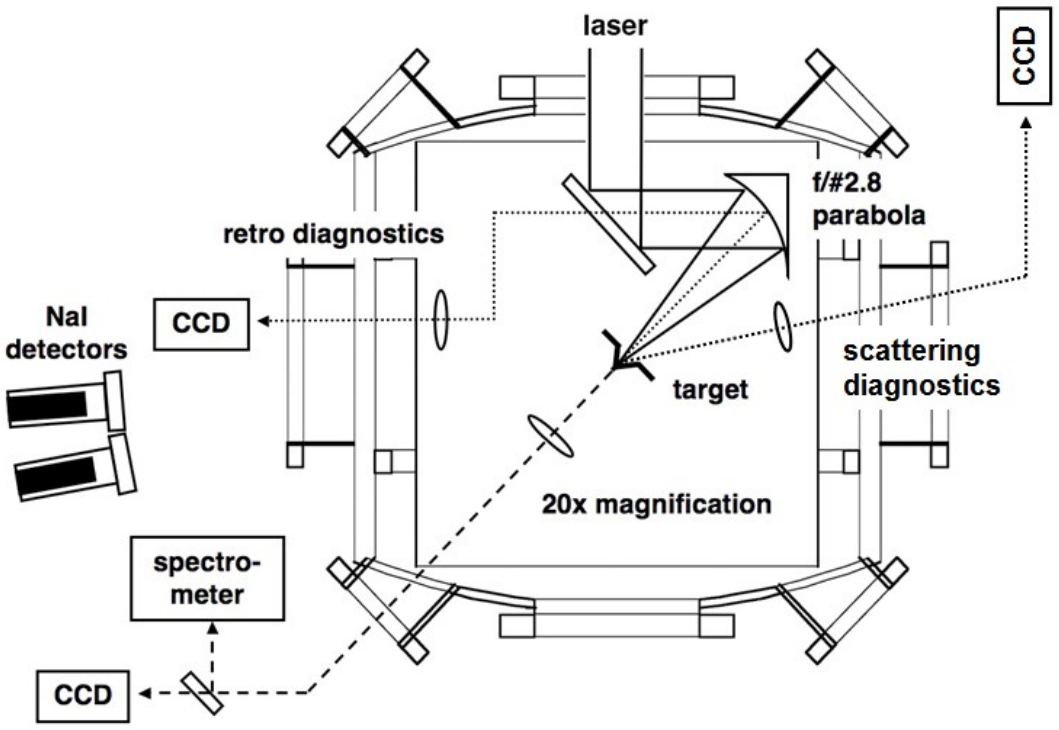

Figure 55. Schematics of the experimental setup.

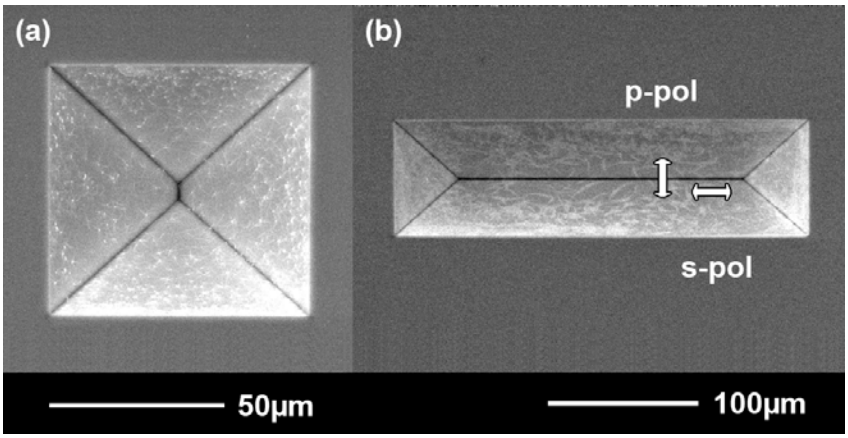

Figure 56. SEM images of a reentrant (a) pyramidal cone and (b) wedge from the anisotropic etching of silicon wafer. Arrows represent the linearly polarized electric field directions of the laser.

F/#2.8, 45º off-axis parabola. Focal spot size was 7 μm (FWHM) in diameter and a corresponding peak intensity was $2 \pm 0.5 \times 10^{19}$ W/cm^2. The low level (10^{-4}) pre-pulses created an under-dense plasma with scale length of the order of 3 μm at the front of the target [63].

Various thicknesses of aluminum foils, reentrant silicon wedges and pyramid like cones, and copper cone targets from University of Nevada at Reno were irradiated. Aluminum foils were irradiated with *p*-polarized light with an incident angle of 10º ~ 45º. The dimensions of the opening square and depth of the cone were 80×80 μm^2 and 56 μm respectively. The wedge length along the long direction was 200 μm and the other dimensions were the same as that of the cone. These cone and wedge shaped silicon surfaces were coated with 1 μm thick aluminum to permit reasonable comparison with the planar foil targets. SEM images of these kinds of targets are illustrated in Figure 56 along with the polarization configurations just described.

The size of UNR copper cone targets was 250 microns at the base while its height was 200 ~ 250 μm depending on the opening angle. The tallest cone had a long tip extending further from the sharp cones. Opening angle (20° ~ 60°) is the full angle

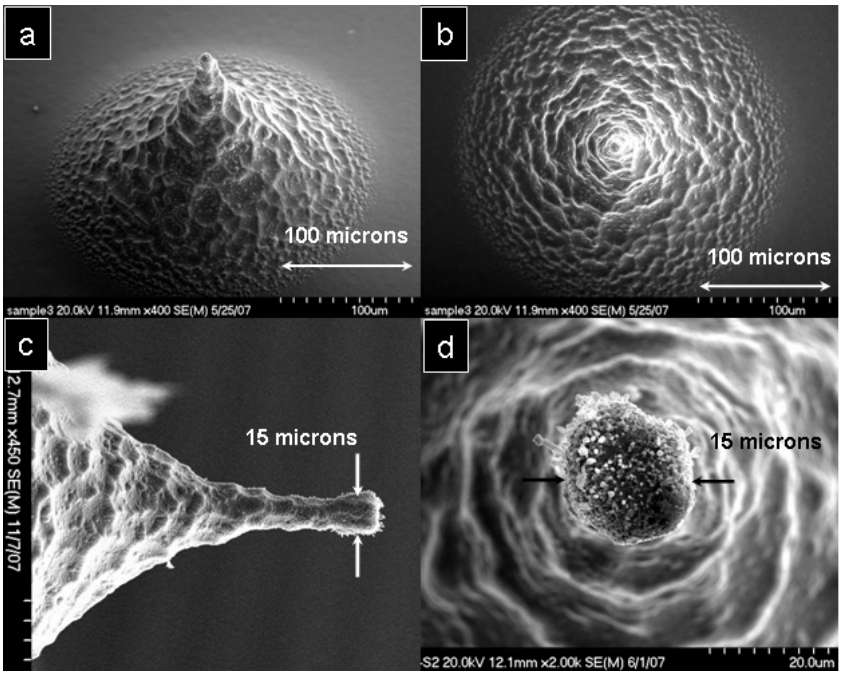

Figure 57. SEM images of typical copper cone targets. (Courtesy of Nathalie Renard Le Galloudec) (a) The base diameter is ~ 250 μm while the bumps on the surface are of the order of 15 ~ 20 μm. (b) Inside view of a cone (what the laser sees). (c) A typical long tip cone target. (d) The top view of the outer tip.

measured from one side to another. These 10 μm thick copper cones of different opening angles were put in the chamber along with 10 μm flat copper targets.

For precise target alignment and ensuring reproducibility in the electron production, scattering diagnostics and retro-imaging diagnostics were set for precise target alignment for cone and wedge targets (chapter 3.3.2).

Optical emission from the target rear surface was imaged on to a CCD and to a spectrometer entrance slit with a magnification of 20. A spectrometer fitted with a 600 grooves/mm grating blazed at 750 nm was employed. Neutral density filters and band-pass filters (RG750 or BG39) were inserted in the light path to select wavelengths around 800 nm or 400 nm and ensure good exposure. Bremsstrahlung x-rays were also monitored with NaI scintillating detectors. X-rays were observed through the 5 mm

thick stainless steel vacuum chamber wall and the detector aluminum housing, provided a baseline shielding ($1/e^2$ cutoff energy: 85 keV) for every detector. In addition, 0.31 cm, 0.95 cm and 4.8 cm of lead plates were used as filters for $1/e^2$ cutoff energies of 269, 413 and 916 keV respectively. As a result, we obtained hard x-ray spectra from 100 keV to 1 MeV for each shot.

6.2. 800 NM, ω_0 CTR MEASUREMENTS

6.2.1. Plane target data

Typical images of the 800 nm CTR light emitted from the rear surface of various aluminum foils are illustrated in Figure 58. These data were remarkably reproducible on a shot to shot basis. The CTR spot size observed from the electrons produced in the 10 μm target was 6 μm (FWHM) at the backside of the foil. This spot is comparable to the laser focus and suggests a remarkable of degree of electron collimation given that the electrons have had to propagate through nearly 10 μm of material.

We then measured the CTR spot size as a function of target thickness (Figure 59). These data indicate that the electrons responsible for the CTR emission process are strongly collimated, diverging with an overall opening angle of about 6°. It should be

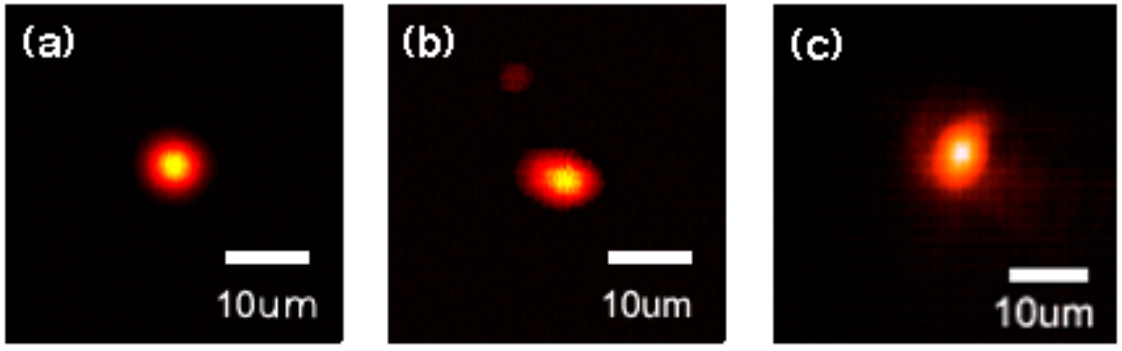

Figure 58. Image of optical emission from the rear side of (a) 10 μm, (b) 25 μm, and (c) 40 μm aluminum foil targets.

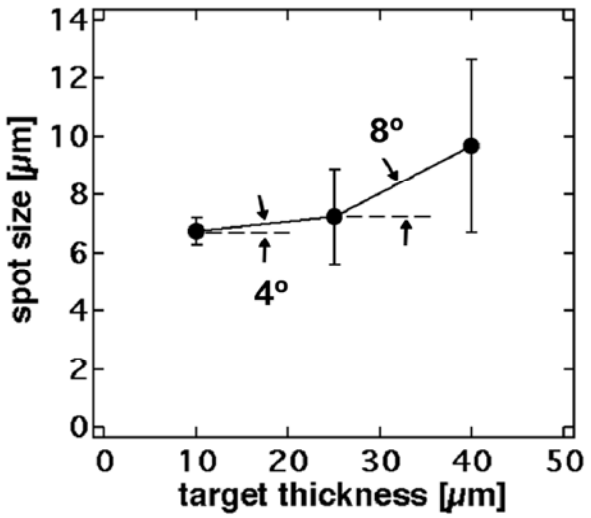

Figure 59. Emission sizes (FWHM diameter) from 10, 25, 40 μm of aluminum foils. Electron beam divergences correspond to spot size variations are 4º between 10 μm and 25 μm and 8º between 25 μm and 40 μm.

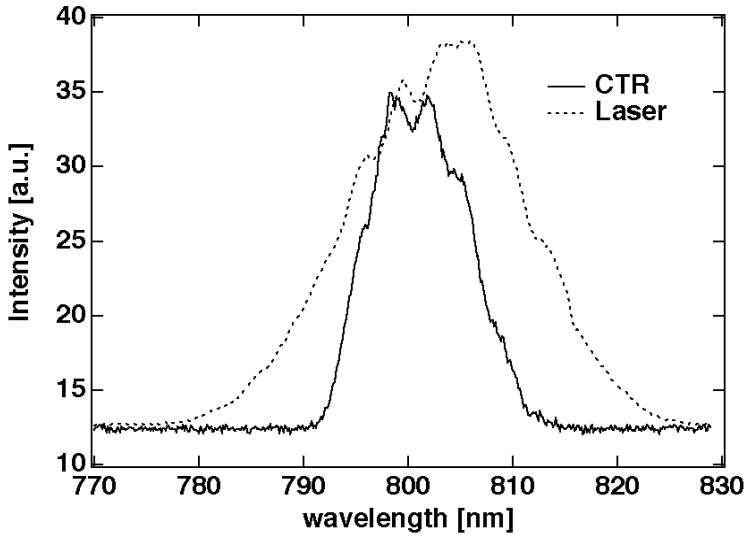

Figure 60. Typical spectrum of CTR emission from the 10-μm target (solid line) overlaid with the spectrum of the Ti:sapphire laser (dotted line).

noted that incoherent emission from electrons produces a much lower signal so it is possible that there is a much broader halo of lower energy electrons round this small CTR spot. This is confirmed when the *K*-shell emission is observed. We have previously examined the spatial profile of *K*-shell emission from these kinds of targets and found that the electrons responsible for that emission have a divergence 10 times that of the much hotter electrons producing the CTR [32]. This difference is attributable to the fact that the electrons responsible for the K_α emission in those experiments are an order of magnitude less energetic (i.e. ~ 30 keV) [77] than those responsible for the CTR we observe (as we will show below). This large degree of collimation in the CTR electrons can perhaps be understood as a consequence of the magnetic self-focusing of the electron beam [79]. Strong magnetic fields generated by such an energetic electron flow keep the stream collimated tightly. We do see, though, that the collimation of the electrons weakens as they propagate. Figure 59 shows that between 10 and 25 μm, electron beam divergence was about 4° and between 25 and 40 μm, it appears to broaden around 8°.

A typical spectrum of this CTR radiation is shown in Figure 60. This light was peaked at around 800 nm which is the same as the central wavelength of laser, and no significant broad-band emission in the infrared range was observed. One we should note is that a very low-level emission at around 400 nm is observed. However it is a couple of order weak signal comparing to 800 nm, therefore we do not pay too much attention on it in this section and it is discussed separately in the section 6.2.

Integrated CTR intensities from various experimental conditions are presented in Figure 61. The CTR intensities from the 25 μm thick slab targets were two orders of magnitude lower than that from 10 μm targets.

Bremsstrahlung x-ray yields measured with NaI detectors are presented in Figure 62. Here each data point represents integrated x-ray yields above the cutoff energy. To determine the electron temperature from these data, we calculated bremsstrahlung spectra $f(E_\gamma)dE_\gamma$ from electrons traveling in the solid, which have a single temperature Maxwellian energy distribution (See chapter 2.3.2). E_γ is the photon energy. After

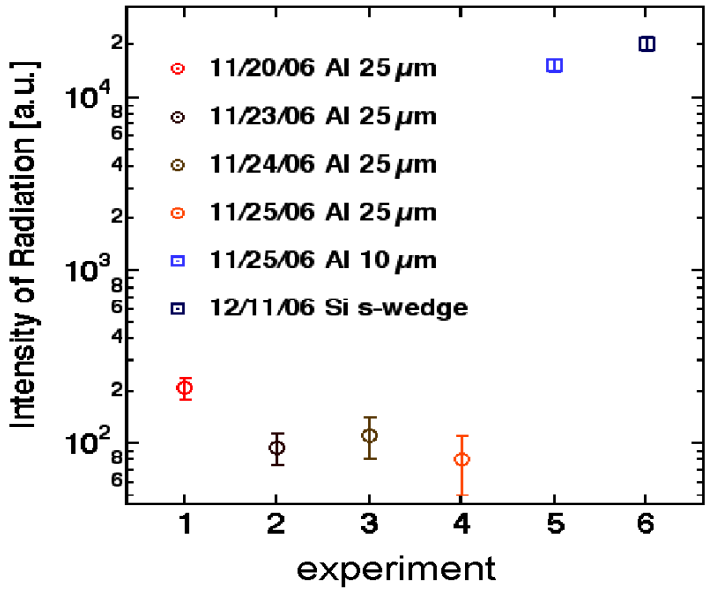

Figure 61. CTR intensities measured in different experiments.

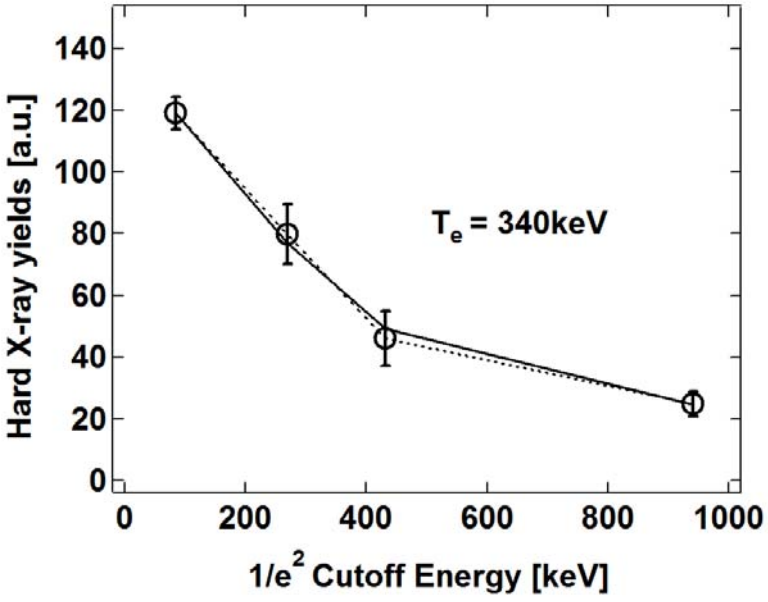

Figure 62. Bremsstrahlung measurement. The dashed line connects the data and the solid line represents the best fit.

convolution with the x-ray transmission of the filters $T(E_\gamma)$, the results $\int E_\gamma T(E_\gamma) f(E_\gamma) dE_\gamma$ were compared and fitted to experimental data, using a least square analysis by varying initial electron temperature. The best-fit is presented in Figure 62, which suggests that the corresponding electron temperature was ~ 340 keV.

Because both CTR and the laser have ~ 800 nm wavelength and we did not use time-gated detector for imaging them, it need to be justified that our data did not affected by post-pulses of laser (See Figure 20). Therefore *z*-scan of the target around the best focus of the laser was performed and the signal intensities were measured. If the source of our image was a leakage of post-pulse, it should come after the main pulse blew off the whole target material (over 10 μm of aluminum). In this case the signal levels from such a post-pulse should be the constant regardless of the target *z*-position, at least within the Rayleigh range of the laser. That is, within the Rayleigh length the laser intensity

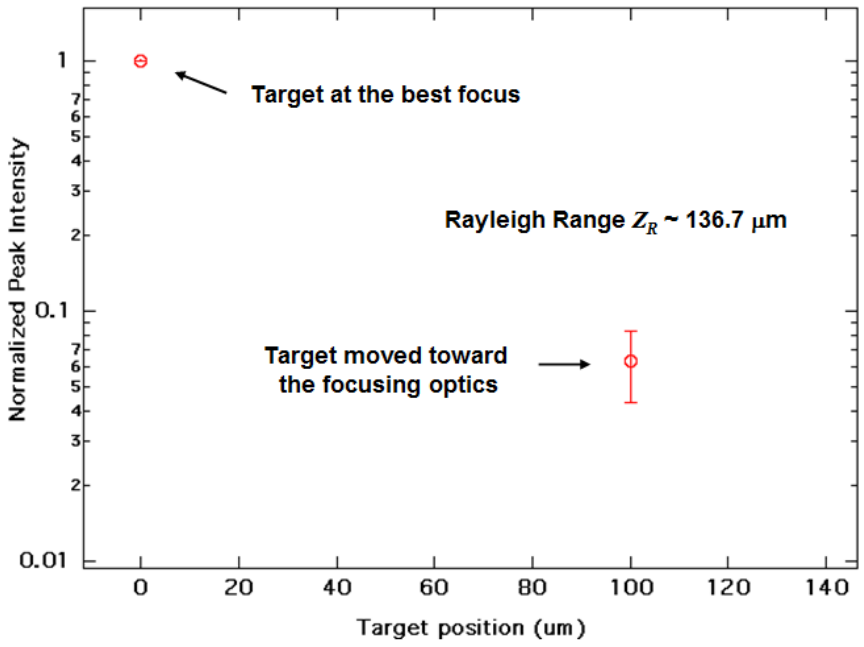

Figure 63. CTR intensity from 10 μm aluminum foils at different *z*-positions. Within the Rayleigh range, it drops by an order of magnitude.

changes only by factor of 2 and is still ~ 10^{19} W/cm^2 so it is reasonable to expect that material blow-off resulting from the main pulse are not so different from the best focal case. However, we found that signal intensities were very sensitive to the target z-position, for example at z = 100 μm, we observed signal dropping by an order of magnitude in comparison with z = 0 case. Therefore, we conclude that our signals were not coming from post-pulses and they were ω_0 CTR from the target rear side.

6.2.2. Analysis using 1D electron transport model

The well-peaked CTR spectrum that we observe is consistent with the published theory of coherent transition radiation (CTR) [34, 38]. In contrast to the broad spectrum of incoherent optical transition radiation, whose strength is proportional to the number of electrons N, when the transition radiation from individual electron bunches add coherently, CTR power is proportional to the square of the electron number N^2, and the spectrum peaks at the harmonics of the electron bunching frequency. Our observed spectrum is peaked at the laser wavelength (Figure 60), indicating that this light is predominantly generated by one electron micro-pulse per laser cycle. This phenomenon is expected for some heating mechanisms, e.g. resonance absorption [80] and vacuum heating [3].

The spectrum of the coherent transition radiation is directly related to the temporal variation of electron flux at the rear surface of target. For an analytical analysis of the CTR we used a 1D ballistic model, which is described in the chapter 2.4, to simulate electron transport in the target. In addition, for both resonance absorption and Brunel's heating, electrons move along target normal direction, we set $\theta = 0°$ and further simply the model.

In the simplified model, a total of M = 15 electron micro-pulses corresponding the 40 fs pulse duration were injected into target normal direction at the front side. The delay between two adjacent micro-pulses is $\delta T = \lambda_L/c$ = 2.67 fs corresponding to the 800

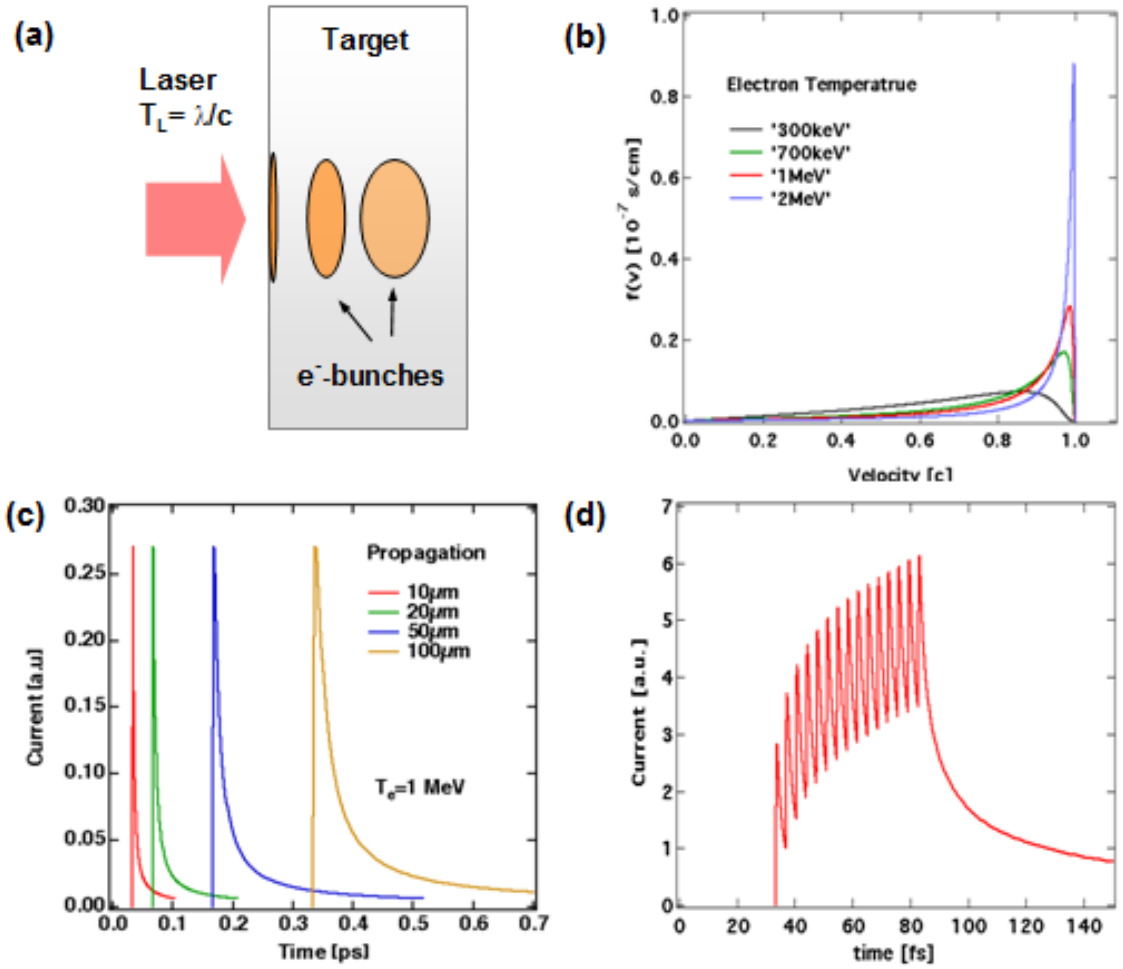

Figure 64. (a) Illustration of electron bunch generation and dephasing. (b) Maxwellian velocity distribution with different temperatures. (c) Dispersion of electron bunch (T = 1 MeV) as it propagates. (d) Current at the target rear side. (T = 1 MeV, d = 10 μm, M = 15, δt = 2.33 fs)

nm laser wavelength. Each bunch consists of a number P of hot electrons with a Boltzmann energy distribution with temperature T,

$$f(v)=\frac{1}{kT_e}\exp\left[\frac{m_e c^2}{kT_e}\left(1-\left(1-\frac{v^2}{c^2}\right)^{-1/2}\right)\right]m_e v\left(1-\frac{v^2}{c^2}\right)^{-3/2}. \quad (103)$$

Due to the velocity dispersion, each electron bunch broadens during propagation and overlaps each other. Therefore electrons number in time passing through a target rear surface is given as Figure 64 (d) and coherent radiation by the collective motion of electrons at the rear surface of target at frequency ω is given by [27]

$$I_{CTR}(\omega)=\eta(\omega)P^2\left|j(\omega)\right|^2\frac{\sin^2(M\omega\delta T/2)}{\sin^2(\omega\delta T/2)} \quad (104)$$

where $\eta(\omega)$ is a light intensity due to a single electron, and $j(\omega)$ is a Fourier transform of

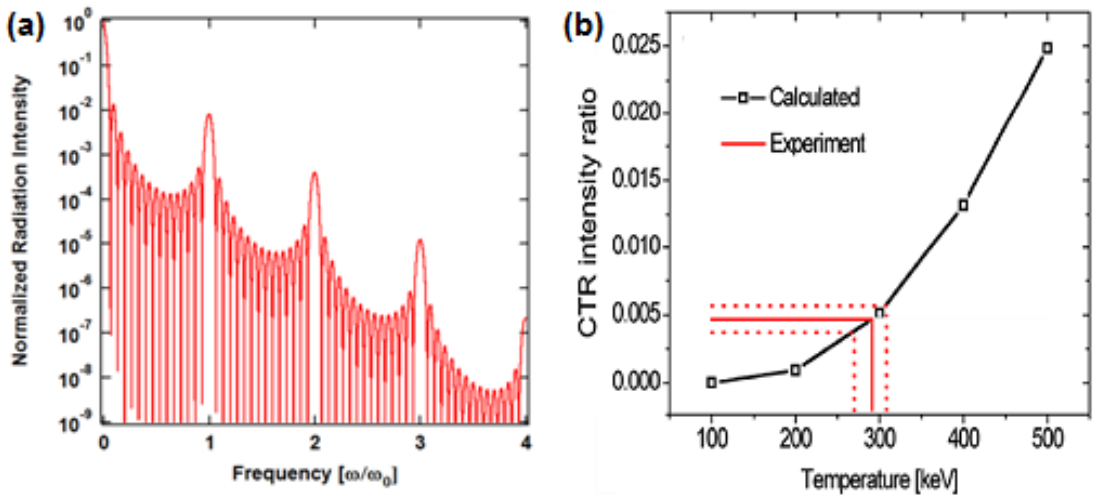

Figure 65. (a) CTR spectrum. (b) Black squares are a calculation of CTR ratios from 10 and 25 μm of aluminum targets for different electron temperature. Horizontal solid and dotted red lines are the measured ratio and the errors in the experiment, respectively. Vertical lines present the corresponding temperatures.

the electron current density at the rear surface of the target.

Dramatic reduction of CTR intensity from thicker target (Figure 61) results from the broadening of each electron micro-bunch as a result of its broad velocity distribution as it propagates through the target. The velocity dispersion broadening reduces the oscillation amplitude of the electron current after propagating a certain distance. Because the CTR intensity is a function of the Fourier transform of electron flux, the reduction in the oscillation amplitude corresponds to a reduced CTR intensity.

Using Eq. (104), we calculated CTR intensities from 10 μm and 25 μm aluminum foils with our 1D ballistic model assuming various electron temperatures. Calculated ratios of the CTR radiation intensities from the two target thicknesses are plotted in Figure 65 (b) as a function of hot electron longitudinal temperature. These calculated ratios were compared to radiation intensities from our experiment, 4.68×10^{-3}, which is depicted by the horizontal solid red line in Figure 65 (b). This analysis suggests a hot electron temperature of 290 keV. This result is in remarkable agreement with the temperature measured from the bremsstrahlung hard x-ray data.

As previously noted, the CTR spectrum indicated that hot electrons were accelerated into the target at the frequency of laser, suggesting that resonance absorption or vacuum heating were the principal candidates for the heating mechanism. As we discussed above, pre-plasma with a few microns of scale length was formed before the main pulse arrived, and it was larger than the quiver amplitude ($eE/m_e\omega^2 < 1$ μm) of the electrons in a laser intensity of 10^{19} W/cm^2. Since vacuum heating becomes dominant only when a plasma scale length is smaller than an electron quiver radius, resonance absorption would be the main heating process in our experiment. The electron temperature due to resonance absorption can be estimated by

$$T_{res} = k \cdot (I_{17}\lambda_{\mu m}^2)^{1/3} \text{ keV} \qquad (105)$$

where k is a constant about 30 ~ 100 [3, 79] and I_{17} is the laser intensity in units of 10^{17} W/cm^2 and $\lambda_{\mu m}$ is the laser wavelength in microns. Our laser intensity 2×10^{19} W/cm^2 suggests an electron temperature between 150 ~ 500 keV.

6.2.3. Silicon cone and wedge data

The spatial profile of CTR emission from the silicon cone and wedge targets is dramatically different than the emission from planar slabs. The spatial CTR emissions from the wedge and cone targets are presented in Figure 66. As with the aluminum slabs, the spectrum was peaked at 800 nm indicating that the electrons were bunched at the laser frequency. Again this implies that these were electrons heated by resonance absorptions. However, the emission shapes are clearly different from the planar targets exhibiting significant structure. In all cases, there appears to be bright CTR emission emanating from the region of the tip surround by emission which appears to result from electrons traveling into the target normal to the surfaces of the wedge or four walled cone. This clearly suggests two populations of electrons, those directed normal to the cone / wedge walls and those directed down into the tip. It should be noted that the brightness of the feature near the tip is, at least in part, a result of the fact that the electron traveling toward the tip traverse less material to reach the back side. Nonetheless, these images are very reproducible and clearly illustrate at least two electron propagation directions. In addition, the emission from electrons coming out near the tip of both *p*- and *s*-polarized wedges is elongated along the crease. In the *p*-wedge emission normal to the walls is very weak compared to the tip emission. The cone target exhibits very bright emission from the tip surrounded by four distinct features corresponding to the four cone walls.

As discussed by Yasuhiko Sentoku *et al*. [19], in the ICF-type cone targets irradiated by ultra intense laser, strong magnetic fields are formed only on the laser polarization plane and they play an important role in confining hot electrons on the cone

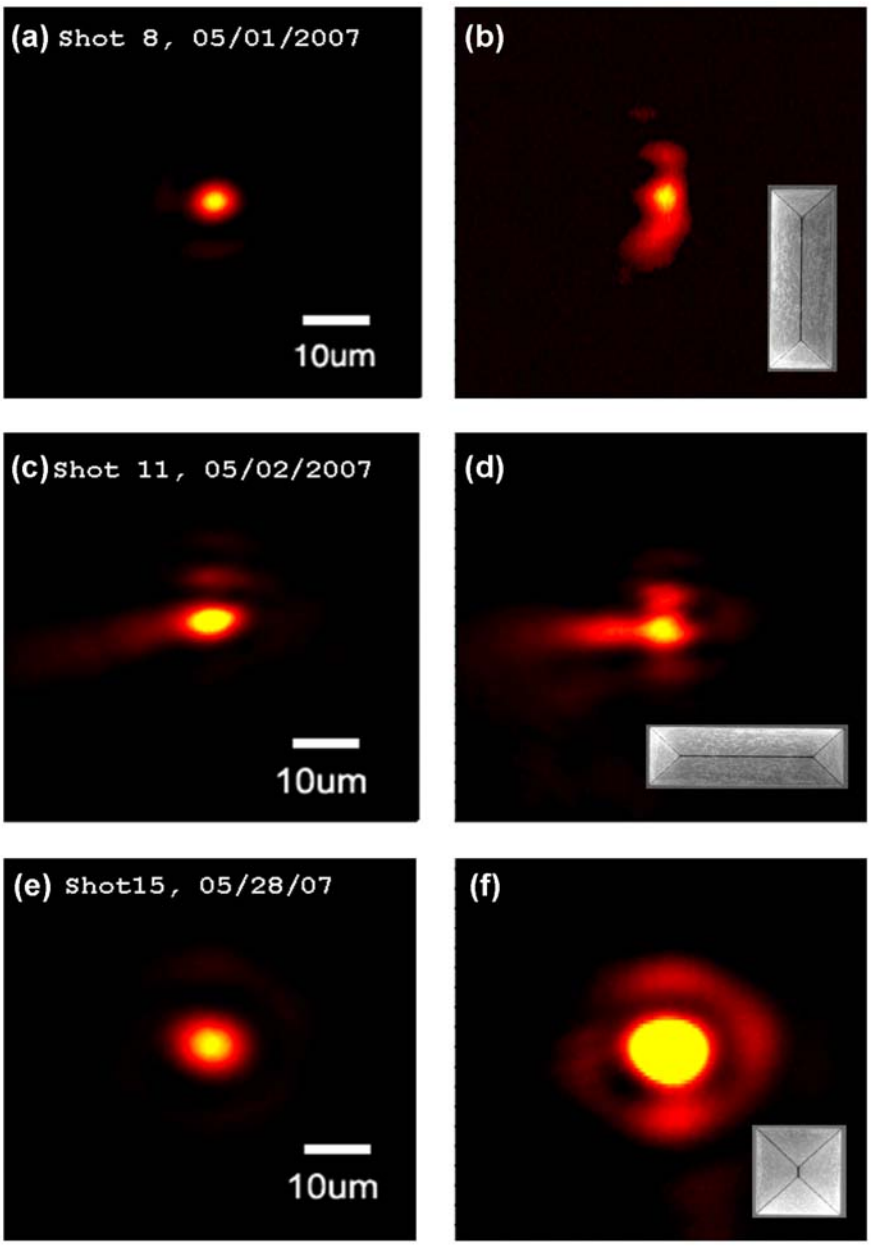

Figure 66. Emission patterns from (a, b) *p*-wedge, (c, d) *s*-wedge and (e, f) cone targets. All images have the same scale and irradiated lasers were linearly polarized in horizontal direction for all cases. The color scales have been adjusted in each image to emphasize the side structures. Image (f) is false-contrasted for clear view of side lobes and central spot is overexposed. Central spot size from well exposed image is about 8 μm (FWHM) diameter.

surface. The difference in *p*- and *s*-wedge images can perhaps also be understood as a consequence of anisotropic quasi-static electromagnetic fields being generated on the wedge surfaces. For *p*-wedges, surface currents moving toward the wedge crease can be excited by the reflected electric fields and electron motion normal to the surface were reflected by strong magnetic fields parallel to the wall. In contrast, for *s*-wedges, electric fields can be parallel to the wall and have no component contributing to electron flow toward the center. Electrons that were accelerated into the target also could not be confined by magnetic fields because reflected magnetic fields and electron motions had the same directional component.

We observed a four-lobe pattern from the pyramidal silicon cone target as well. Figure 66 (c) was renormalized to emphasize these side patterns. The side structure had four lobes which correspond to the position of four walls. Since the opening angle of our cone is rather large for effective cone guiding, some electrons were accelerated into the target bulk. The ballistic electron transport model we used for the planar target, however, was not complex enough to describe these geometrical effects. For a quantitative understanding of these results, we would require PIC simulations that model the current density over the whole time scale of the electron bunches leaving the target rear surface.

6.2.4. CTR data from UNR cone target

We also observed 800 nm CTR from the copper cone targets from the University of Nevada, Reno. Figure 67 shows a typical CTR image from the tip of the cone. Figure 67 (b) is an overexposed, however, it clearly shows the electron guiding nature of the cone. Due to a shot-to-shot pointing instability of the laser, though a precise target alignment with alignment beam, some laser pulses heat off-center of the cone. Left region is the wall the laser pulse directly irradiated and where hot electrons are generated. Right round spot is where the tip of the cone is located. Emission are originated by the

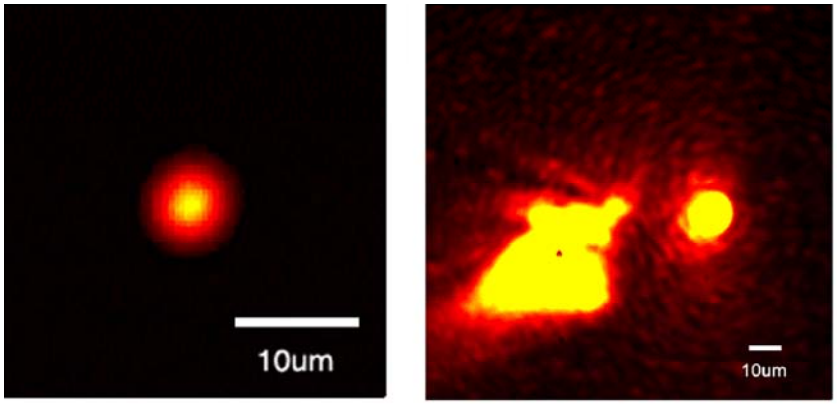

Figure 67. Typical CTR images from various copper cones. (a) Well exposed image from 30° cone. (b) Overexposed image from 40° cone.

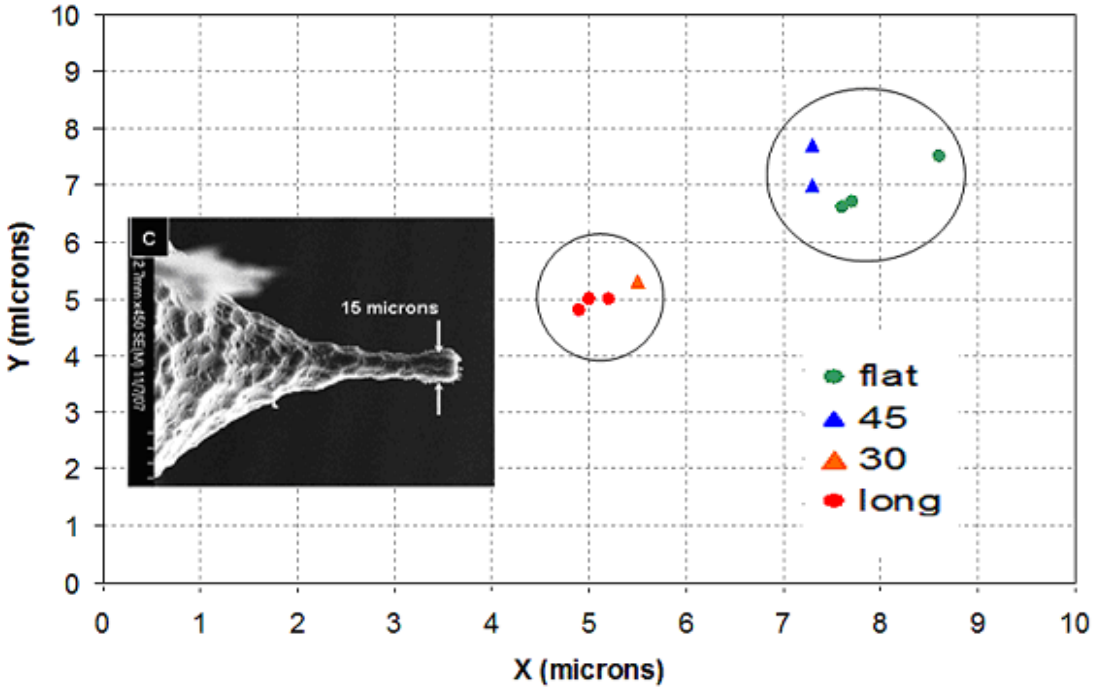

Figure 68. Size of CTR emission for flat copper targets along with several copper cones of different opening angles. (Inset) SEM image of long-tip cone target. Its outer diameter is 15 µm. (Courtesy of Nathalie Renard-Le Galloudec)

electrons generated from the left area were guided along walls and emitted from the tip. FWHM diameters of radiations are measured for cone targets with various opening angle and 10 μm copper foils for the comparison (Figure 68). For the 45° cones and the flat target, emission spot sizes are 7 ~ 8 μm which is of the order of the focal spot. In contrast, the emission from the 30° cones and long tip cones is about 5 μm and it is smaller than the laser focus. We also note that the radiation from the long-tip cones is about smaller than the outer tip size. These measurements confirm several aspects about experimental and theoretical studies published by other groups [19, 81], namely the focusing of the light into the tip of the cone and the guiding of the hot electrons.

We also measured CTR intensity as a function of *z*-position of laser focus. As shown in the Figure 69, CTR intensity is maximized when the focus is located at the entrance of cone target. The interface of the cone material and the laser is ~ 150 μm

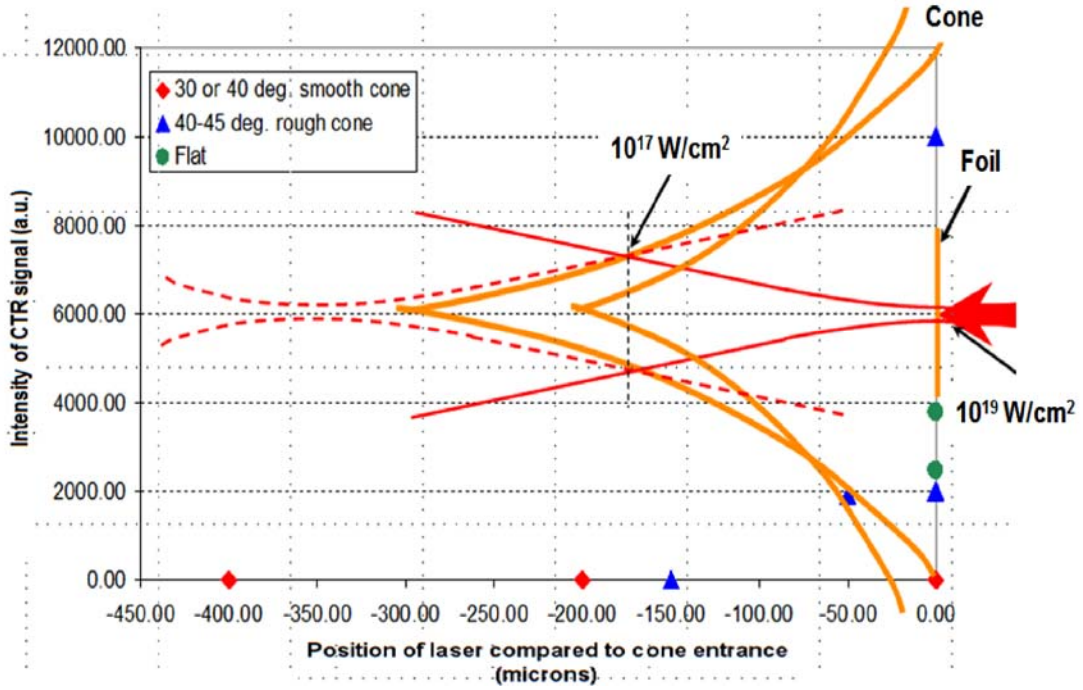

Figure 69. CTR intensities when the laser is focused at different plane. Roughly scaled laser beam and cone targets are also added for comparison. (Courtesy of Nathalie Renard-Le Galloudec)

further down the axis, the equivalent main pulse intensity is ~ 10^{17} W/cm^2. By the same manner, pre-pulses are also defocused and their intensities also down by factor of 2 comparing to flat target. Therefore, scale length of pre-plasma generated by less intense pre-pulses would be also reduced. When the laser is focused more toward the tip, for example z = - 200 µm, the main pulse enters the cones with a large pre-plasma. This pre-plasma might prevent the main beam going further and producing more hot electrons, and in turn produce less CTR productions. If there is less pre-plasma (z = 0), the main pulse could interact better with the target geometry, and cone effects could produce more CTR emissions. Though a less laser intensity, the cone geometry might counter balance it and yield the similar CTR signals.

Finally, we also compare CTR production from different surfaces qualities. We had 10 smooth cones shots and only one gave a saturated signal. All cone CTR signals

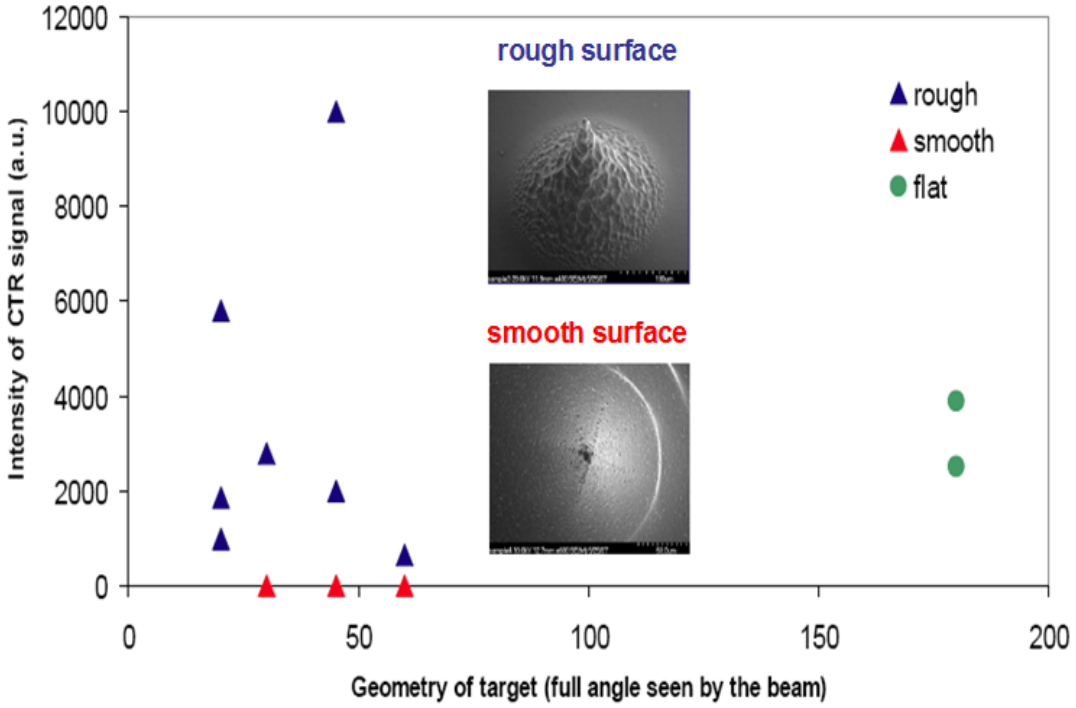

Figure 70. CTR intensities from rough / smooth cone and flat targets. (Courtesy of Nathalie Renard-Le Galloudec)

shown above are from the rough surface cones. Therefore, though small number of shots for smooth surfaces, we conclude the smooth targets did not perform as good as rough cones. Until now, there is no reasonable explanation about this observation. Initial attempt to understand this difference was done by E. D'Humieres at Ecole Polytechnique using 2D PIC simulation, but it did not show a substantial difference in the electron population from the different surface cones.

6.3. 400 NM, $2\omega_0$ CTR MEASUREMENTS

6.3.1. CTR imaging and spectrum data

For this experiment, aluminum foils with 10 μm and 20 μm thickness had been shot. Optical signals from the target rear were filtered with BG39 glasses and neutral density filters.

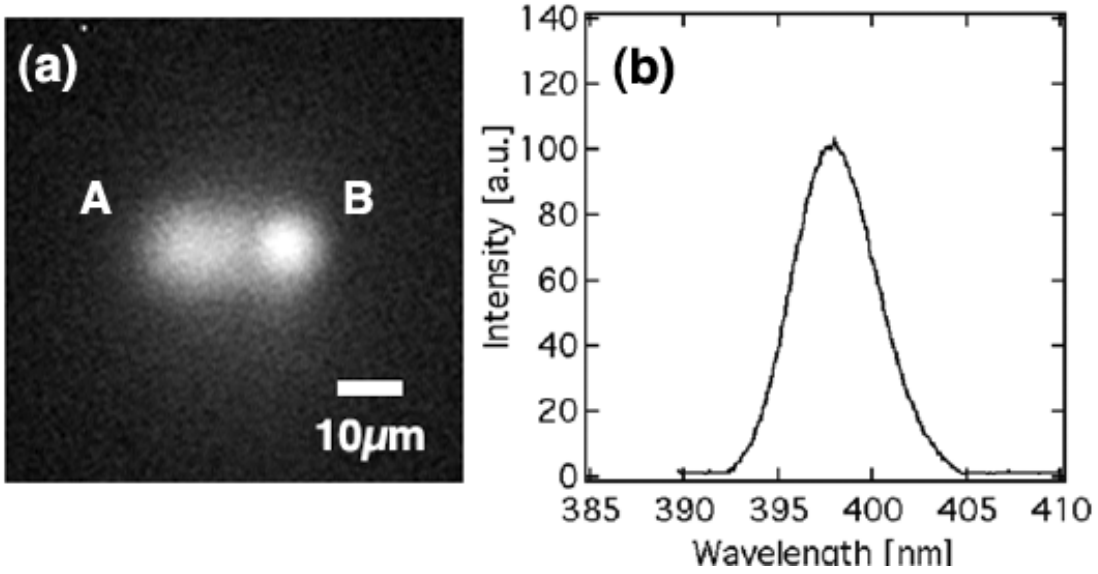

Figure 71. Typical (a) image and (b) spectrum of optical emission from the rear side of 10 μm aluminum foil. Two emissions in the images are denoted by spot A, which is elliptical and spot B, which is circular.

A typical CTR image at 400 nm and spectrum of optical emission from the 10 μm thick aluminum foil are shown in Figure 71. The narrow-band spectrum around 400 nm, which is the half of the laser wavelength, confirms that this emission was CTR from micro-bunched electrons. Two bright spots which are designated A and B in Figure 71 (a), were observed at the same time, with spot A arising from an electron beam propagating normal to the target surface and spot B arising from an electron beam traveling along the axis of laser direction. Emission from spot A is 25 μm in diameter and light in spot B is 10 μm. We also observe strong CTR emission at 800 nm, the laser. When the CTR at 800 nm is imaged, only one spot is observed arising from an electron beam propagating normal to the target surface [33]. We attribute the emission from lobe A with electrons bunched at the laser frequency consistent with resonance absorption and emission in lobe B to arise from electrons bunched predominantly at twice the laser frequency indicating $\boldsymbol{j} \times \mathbf{B}$ acceleration. Electrons from resonance absorption exhibit a greater divergence than the $\boldsymbol{j} \times \mathbf{B}$ driven hot electrons, which emerge from the backside with a size nearly the same as that of the laser focal spot.

In order to characterize these two electron beams, we measured the peak intensity of each CTR signal from 10 μm thick Al targets as a function of on-target laser intensity, which is changed by varying laser energy, results which are presented in Figure 72. We observed a sharp increase in CTR signal from both lobes as intensity increased, with stronger scaling in lobe B, which is from electrons emitted along the laser axis. We fitted the scaling of CTR signal in spots A and B to $\sim I^{\alpha}$, finding that $\alpha = 4.6 \pm 0.3$ and 5.4 ± 0.2, for A and B respectively.

6.3.2. Analysis with ballistic transport model

To understand the distinction in the two emission spots, CTR spectra were calculated using formulae developed by Zheng *et al.* [30] (chapter 2.4). We assume that electrons move ballistically on a line, which is placed in the *z-x* plane and has an angle of

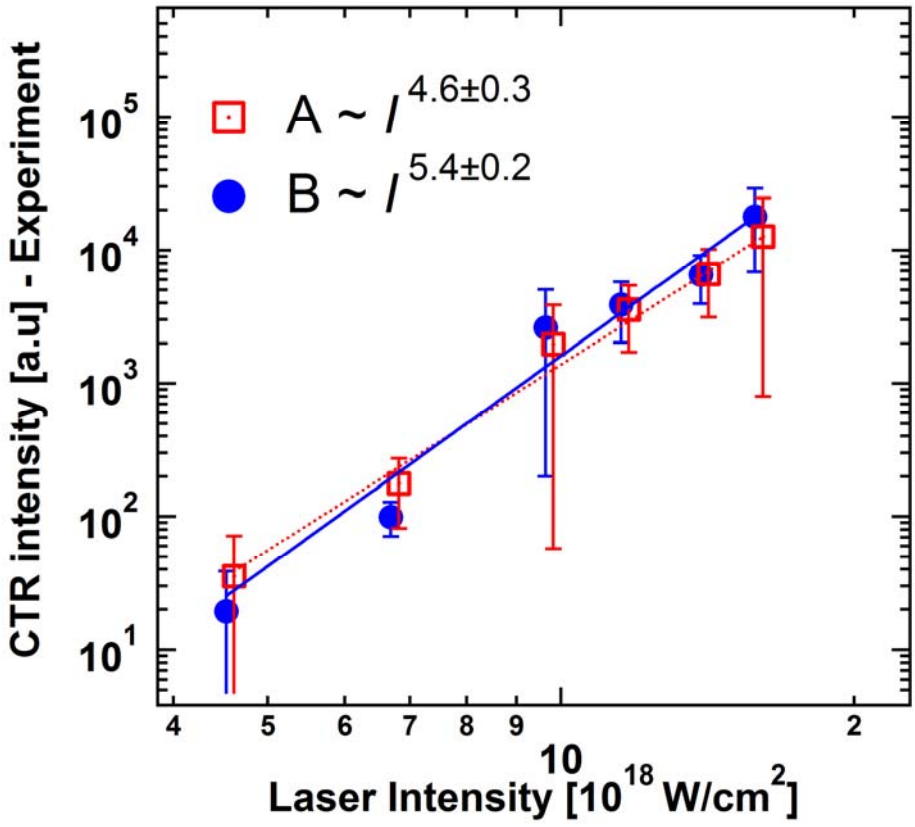

Figure 72. Dependence of CTR intensity around 400 nm on laser intensity: experimental data. The Error bars represent the standard deviations of measurement. For easy reading, data positions for A and resonance absorption have offset of + 0.1 in *x*-axis and data for B and $\boldsymbol{j} \times \mathbf{B}$ heating have an offset of - 0.1.

Θ between *z*-axis. The configuration for calculation is depicted in Figure 73. The differential CTR radiance, ε_{CTR} is given by

$$\frac{d^2\mathcal{E}_{CTR}}{d\omega d\Omega} \sim N_b^2 \left| \int d\tau d\beta e^{i\omega\tau} \sum_{n=1}^{\Lambda} \delta(\tau - \tau_n - t_0/\beta) \times \frac{\beta\cos\Theta(\sin\theta - \beta\sin\Theta) f_v(\beta)}{\left[(1-\beta\sin\theta\sin\Theta)^2 - \beta^2\cos^2\theta\cos^2\Theta\right]} \right|^2 \tag{106}$$

where N_b is the electron number in each electron bunch, Λ is a total number of electron bunches, θ is angle of observation, t_0 is the time when the fastest electron reaches the target rear side, τ_n is the time when *n*-th electron bunch is generated, β is speed of electrons in the units of *c*, and $f_v(\beta)$ is the electron velocity distribution. We assume that hot electrons in each electron bunch have a relativistic Boltzmann velocity distribution with temperature *T*

$$f_v(\beta) = \frac{\beta}{T(1-\beta^2)^{3/2}} \exp\left[-\frac{1}{T}\left(\frac{1}{\sqrt{1-\beta^2}} - 1\right)\right]. \tag{107}$$

In addition, the number of electron passing through a target rear surface at time τ is given by

$$N(\tau) = \frac{N}{\Lambda T} \sum_{n=1}^{\Lambda} \frac{\left(t_0/(\tau-\tau_0)\right) \exp\left[-\frac{1}{T}\left(\frac{1}{\sqrt{1-\left(t_0/(\tau-\tau_0)\right)^2}} - 1\right)\right]}{t_0\left[1-\left(t_0/(\tau-\tau_0)\right)^2\right]^{3/2}}. \tag{108}$$

In Figure 74, $N(\tau)$ (or can be called as current) and radiation spectra are plotted for two cases with electron temperature of 1 MeV. The amplitude of these oscillating currents determines the radiation at corresponding frequencies.

The scaling of CTR emission at the second harmonic frequency of the laser with laser intensity have been calculated for the two lobes and presented in Figure 75. For

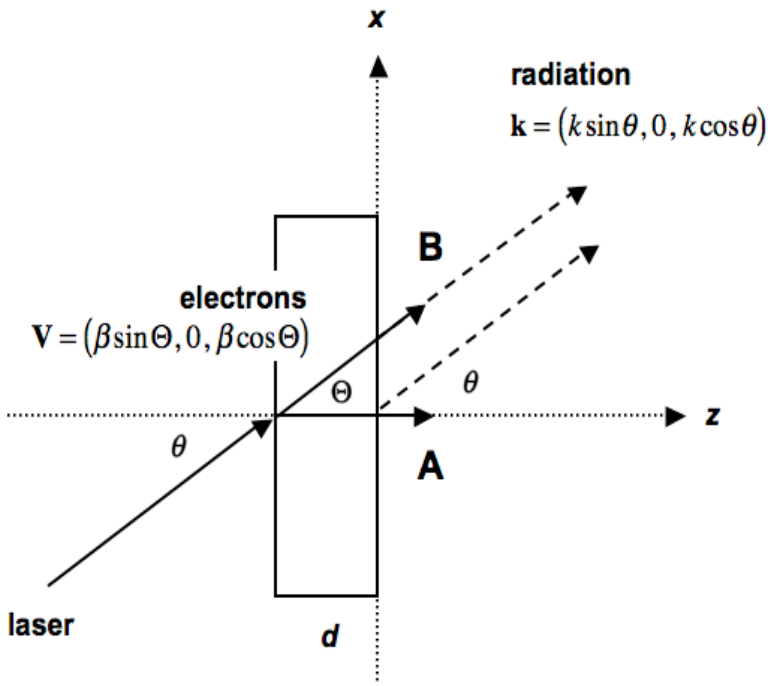

Figure 73. 2D configuration of the CTR calculation. Electron velocity and observation vector are given by $\mathbf{V} = (\beta\cos\Theta, 0, \beta\sin\Theta)$ and $\mathbf{k} = (k\cos\theta, 0, k\sin\theta)$ respectively. Target thickness d = 10 μm, laser incidence angle and observation angle θ = 45°. For the case A or resonance absorption, angle of electron beam propagation Θ = 0° and for the case B or $\boldsymbol{j} \times \mathbf{B}$ heating, Θ = 45°.

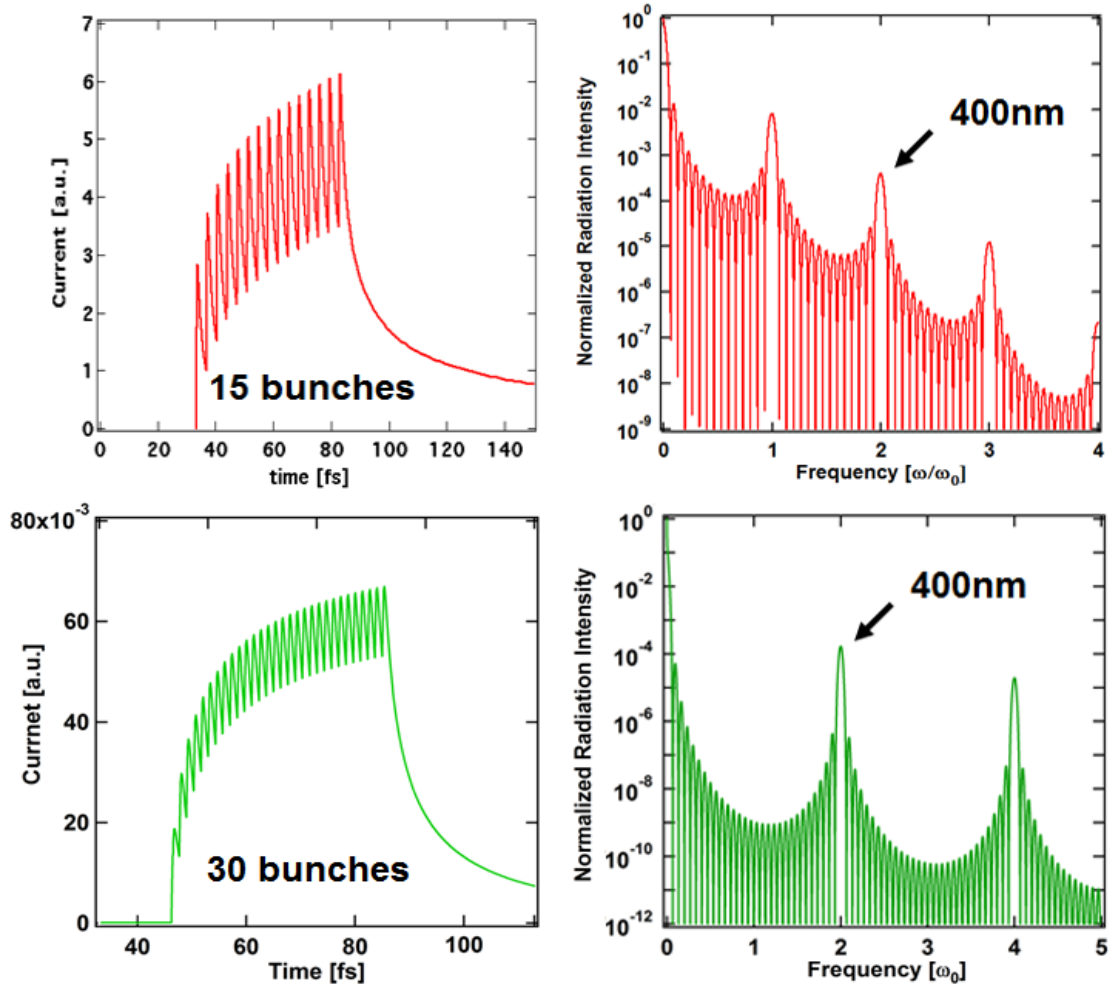

Figure 74. Electron current densities (left column) and CTR powers (right column) by electron beams driven by resonance absorption (upper row) and $\boldsymbol{j} \times \mathbf{B}$ heating (lower row). T_{hot} = 1 MeV for both cases

both cases, N_b is scaled with I and θ is set at 45°. To calculate the intensity scaling of the resonance absorption each electron bunch is spaced one per laser cycle and is assumed to have a temperature given by the empirical formula advanced by Beg *et al.* [7]

$$T_{res} = 0.1\left(I_{17}\lambda_{\mu m}^2\right)^{1/3} \text{ MeV} \qquad (109)$$

where I_{17} is the laser intensity in units of 10^{17} W/cm^2 and $\lambda_{\mu m}$ is the laser wavelength in μm. Λ is set to 15 for the ~ 40 fs laser pulse employed in the experiment. Using this theory, we calculated the CTR spectrum and find, consistent with our data, that it is dominant at the laser frequency, ω_0, but also has significant radiation at $2\omega_0$. To estimate the electron temperature arising from $\boldsymbol{j} \times \mathbf{B}$ heating, where two electron bunches per laser cycle are injected along the laser propaxgating direction (Θ = 45°), we use the ponderomotive formula of Wilks [2]

$$T_{pm} = 0.511\left(\sqrt{1 + I_{17}\lambda_{\mu m}^2/11.3} - 1\right) \text{ MeV} \qquad (110)$$

and set the number of bunches, Λ, to 30 which is twice the number of optical cycles in our pulse. In this case, there is no significant radiation at the fundamental laser frequency and it is also consistent with our experimental observation. Calculated values were fitted to the scaling I^{α} and yield exponential indices of 4.5 for resonance absorption and 5.7 for $\boldsymbol{j} \times \mathbf{B}$ heating, remarkably close to those found experimentally for the two lobes, lending strong evidence that lobe A arises from resonance absorption and lobe B arises from $\boldsymbol{j} \times \mathbf{B}$ heating.

When the electron number N_b is set the same for both cases, the calculated CTR emission for the resonance absorption lobe is about two orders of magnitudes lower than from the $\boldsymbol{j} \times \mathbf{B}$ emission lobe. As shown in the experimental data, the peak emission strength of the two signals have the same value at a laser intensity of ~ 8×10^{18} W/cm^2. We therefore conclude that 8.5 times more electrons are required in a single bunch from the resonance absorption mechanism to match our data, indicating that our laser interaction drives up to an order of magnitude more hot electrons by the resonance

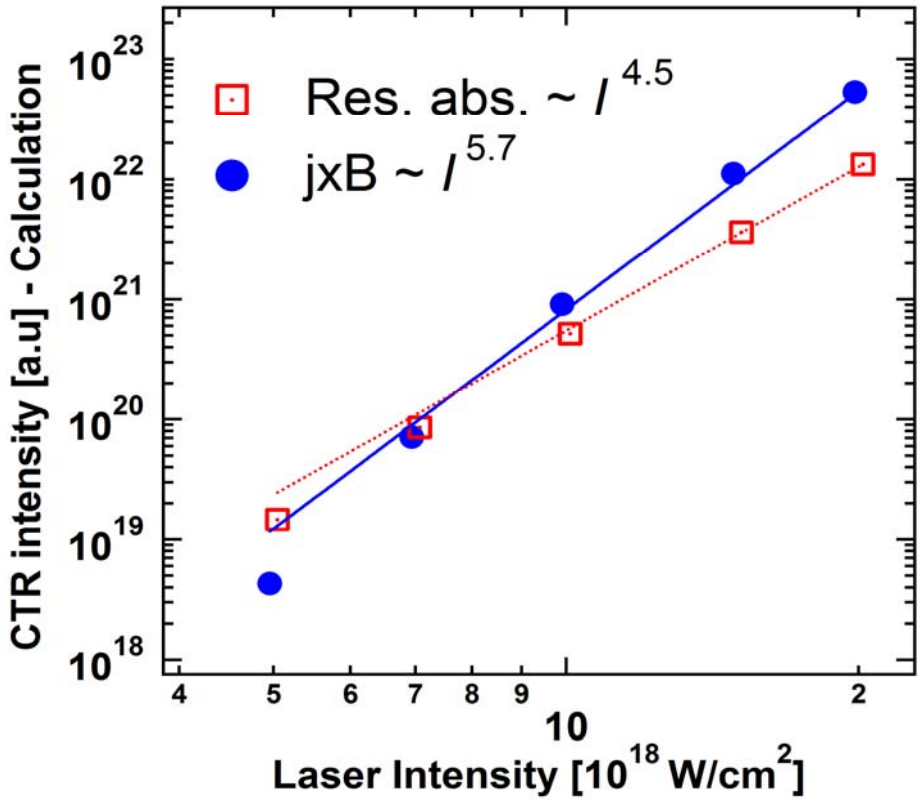

Figure 75. Dependence of CTR intensity around 400 nm on laser intensity: theoretical calculations, where 10 μm Al foil was irradiated with incidence angle of 45°. For easy reading, data for A and resonance absorption have offset of + 0.1 in *x*-axis and data for B and $\boldsymbol{j} \times \mathbf{B}$ heating have an offset of - 0.1.

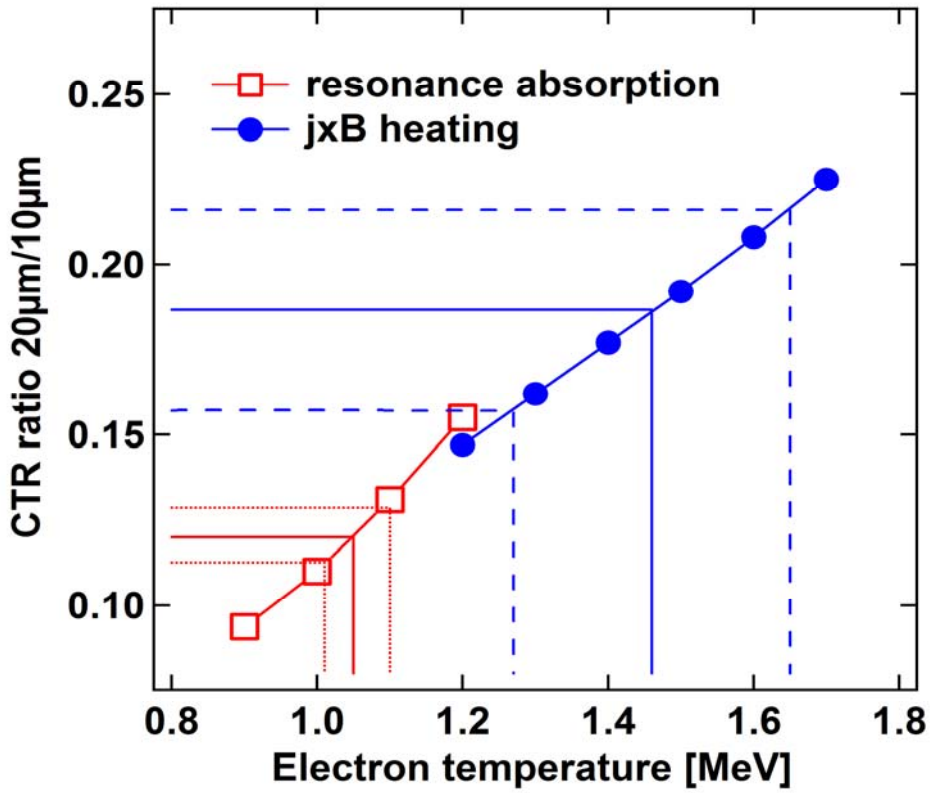

Figure 76. $2\omega_0$ CTR ratios from different thickness of targets, 10 μm and 20 μm. Square and rounds are calculated values for resonance absorption and $\boldsymbol{j} \times \mathbf{B}$ heating. The solid horizontal lines depict measured ratios for spot A and B in the experiment and the verticals represent corresponding electron temperatures. Dotted lines are the errors in the experiments.

absorption mechanism than by $\boldsymbol{j} \times \mathbf{B}$ acceleration. Our finding is qualitatively similar to the findings of Ref. [23] which indicated that resonance absorption with electrons emitted normal to the target surface dominated when the plasma scale length was under 10 μm (the situation in our experiment).

In order to determine the temperature of each electron beam experimentally, the peak intensities of the two radiation spots from both 10 and 20 μm thick aluminum foils were measured and compared. The CTR emission amplitude will decrease as electrons propagate further since velocity dispersion of the finite temperature bunches cause a spread of each bunch. Therefore a drop in CTR intensity with increasing target thickness can be used to determine the hot electron temperature. For spots A and B at the highest laser intensity, peak CTR emission from 20 μm thick targets was 0.120 and 0.186 times that from 10 μm thick targets respectively. Predicted CTR intensity ratios (20 μm / 10 μm) as a function of temperature for the two electron beams were calculated using Eq. (106) and (107), and are plotted in Figure 76. These calculations are compared with our measured ratios, which are depicted by the horizontal lines in this figure. This analysis indicates that the electron beam generated by resonance absorption had a temperature of 1.0 ± 0.1 MeV while the $\boldsymbol{j} \times \mathbf{B}$ beam exhibited a slightly higher temperature of 1.5 ± 0.2 MeV. At a laser intensity of 2×10^{19} W/cm^2, electron temperatures predicted by Eq. (109) and (110) are 0.5 MeV for resonance absorption and 1 MeV for $\boldsymbol{j} \times \mathbf{B}$ heating roughly consistent with our experiment. The slightly higher observed temperatures might be the consequence of an intensity increase from relativistic channeling in the underdense pre-formed plasma [82].

6.3.3. Virtual Laser Plasma Laboratory simulation

As a final confirmation of the interpretation of our data, 3D-PIC simulations of hot electron generation from solid target plasmas with our experimental conditions has been performed using the parallelized relativistic code Virtual Laser Plasma Laboratory

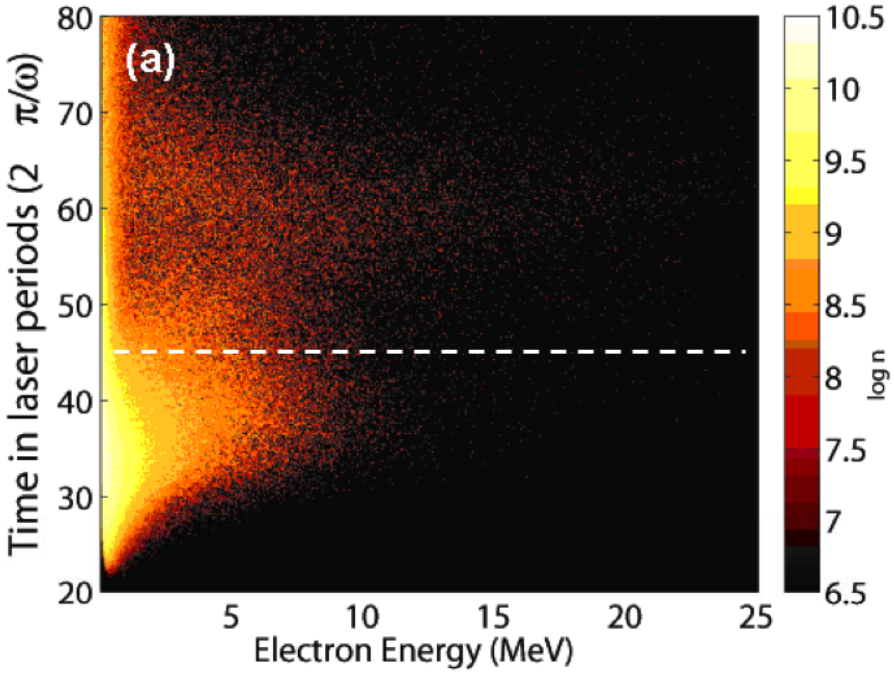

Figure 77. Energy phase spectrum of the hot electron coming out of the target rear surface.

(VLPL) by Alex Pukov and Apunam Karmarka in Heinrich-Heine-Universität Düsseldorf [83]. In this simulation *p*-polarized laser pulses of wavelength 800 nm with peak intensity of 5.4×10^{19} W/cm^2 were obliquely incident at 45° on an overdense plasma layer of 9 μm thickness. The target density was ramped from 0 to 20 times critical density over 3.5 μm (simulating our pre-plasma). The laser pulse was simulated as Gaussian in space and time with a duration of 30 fs and spot radius of 6.7 μm. The entire simulation box was sampled with a grid of 250 × 237 × 20 cells with 8 particles per cell. The temporal variation of the electron energy spectrum emerging from the target back surface is plotted in Figure 77. This shows hot electrons emerging in two different streams coming out in two different times, separated by ~ 40 laser periods. Hot electrons emerging at the earlier time are greater in number but have lower maximum energies than the electrons coming later.

Parameters	Time (20~40)	Time (40~80)
Number of electrons	3.81835×10^{14}	8.40426×10^{13}
Temperature	1.4 MeV	3.3 MeV
Maximum energy	12 MeV	22 MeV
Angular peak	163°	125°

Table 2. Characteristics of electron populations in two time domains.

The angular divergence of these two streams of electrons, illustrated in Figure 78 (a), shows that these two bunches emerge in two distinct angular cones, one along the target normal on the rear surface and the other along the laser propagation direction, though at two different times. This distribution is remarkably similar to the experimental findings in Figure 71. In Figure 78 (b) we have plotted the energy spectrum in each electron emission cone, integrated over the time of the full simulation. The electrons following the laser propagation direction have electron temperature or 3.3 MeV, which is about twice as high as the temperature of electrons emitted normal to the target surface (where T_{hot} = 1.4 MeV), and are about four times as numerous as 2the normal direction electrons. These trends are in good agreement with the experimental findings.

6.4. SUMMARY

We have observed CTR emission from various targets irradiated by 800 nm pulses at intensity above 10^{19} W/cm^2. This emission is predominantly at the fundamental laser frequency and also observed at second harmonic frequency though its level is low. The narrow band spectrum of the emission at both 800 nm and 400 nm

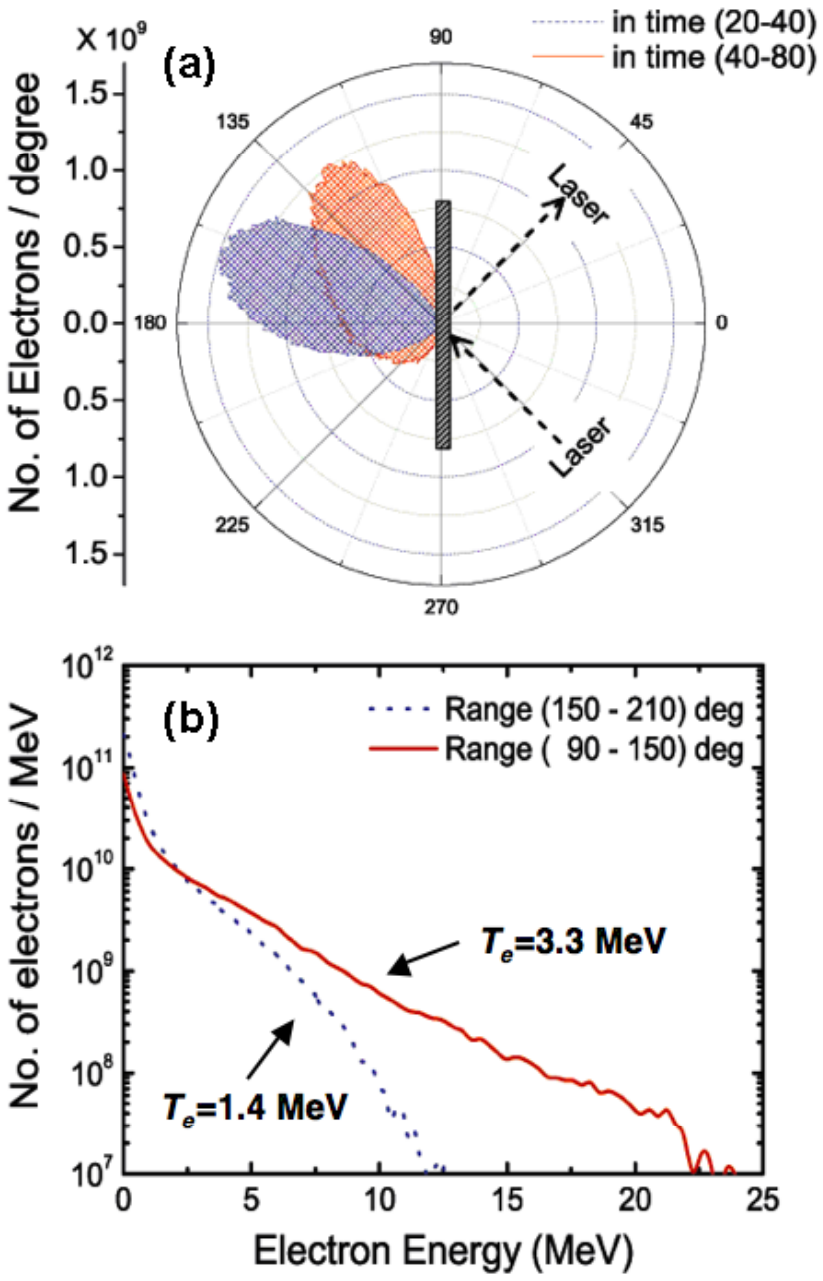

Figure 78. (a) Angular divergence of the hot electrons. (b) Energy spectra of the two streams of electrons.

gives evidence for electron micro-pulses generated by resonance absorption. Small 800 nm emission spots from a series of foil thicknesses indicate the hot, CTR producing electron beams were initially on the order of the laser focal spot size and are strongly collimated with divergence under 10°. The electron temperature obtained by comparing the emission ratio from different target thicknesses with theoretical calculation was also consistent with bremsstrahlung measurements and the scaling law of electron temperature contributed by resonance absorption.

In addition, interesting emission patterns from wedges and cones were observed. These can be understood by the laser polarization dependencies in the cone target discussed in earlier simulations [19]. CTR from wedge and cone targets suggest that quasi-static electromagnetic fields created on the target surfaces affect strongly the hot electron transport. We also compared CTR from the tip of conical targets of different opening angles. Smaller emission sizes from the narrower angle cones are good evidences for the focusing of light by the conical geometry and the guiding of the electrons. The CTR emission size determined by the sharpness of the cone may offer the potential for creating larger areas of increased energy density and particle fluxes relevant to a set of applications.

CTR emission pattern at the second harmonic of the laser frequency reveals two populations of electron beam. Comparing experiment data with analysis indicates that the two emission lobes are correlated with resonance absorption and $\boldsymbol{j} \times \mathbf{B}$ heating. Electrons accelerated by resonance absorption are bunched once per laser cycle and propagate in target normal direction. Otherwise electrons by $\boldsymbol{j} \times \mathbf{B}$ heating are bunched twice per laser cycle in laser propagation direction. Resonance absorption dominates the hot electron production by about an order of magnitude, though with a temperature which is about two thirds that of the electrons in the $\boldsymbol{j} \times \mathbf{B}$ peak. These findings appear to be completely consistent with three dimensional PIC simulations of the experiment.

CHAPTER 7. SUMMARY AND CONCLUSION

The goal of these works has been experimentally studying fast electron acceleration and their transport in various geometry of target irradiated by ultra short and ultra intense laser pulses. To achieve this goal, we had two experimental campaigns; x-ray spectroscopy experiment and CTR experiment. For both, we have utilized various experimental tools and techniques. First of all was the THOR laser, a Ti:sapphire based CPA system and produces 600 mJ, 38 fs pulses at 10 Hz. Focused intensity over 10^{19} W/cm^2 could be achieved. Secondly, several micro-structured targets have been developed. Using a special characteristic of silicon, of which crystalline structure allows anisotropic chemical reaction with hydroxides, we could massively produce small and sharp pyramidal cones and wedges. Based on these, Nanofabrication group at University of Reno also developed free-standing gold and copper cones and provided them for our experiments. Finally, various diagnostics for x-rays and transition radiations in different energy / wavelengths were utilized.

7.1. X-RAY SPECTROSCOPY

X-ray spectroscopy data from the pyramidal cone and wedge targets along with PICLS simulations showed the different laser energy absorption and hot electron generation processes in the different plane of polarization. In the plane of polarization *p*-wedge case, various heating mechanisms come into play including resonance absorption and $\boldsymbol{j} \times \mathbf{B}$ heating along the cone surfaces, resulting in the highest MeV electron production and hard x-ray yield. On the other hand, in the normal plane of polarization *s*-wedge case, less energy absorption leads to higher light pressure on the plasma and energy concentration around the tip of the cone, enhancing the K_α yield in a metallic under-layer.

7.2. CTR MEASUREMENTS

We have observed CTR emission that reveals the nature of the fast electron transports in the target. CTR spectrum has predominant peak at the fundamental laser frequency, which is an evidence for electron micro-pulsing by resonance absorption. Small emission spot over a range of foil thickness indicates a tightly collimated hot electron beam with divergence under 10°. The electron temperature obtained by comparing the CTR intensity ratio from different target thicknesses with that determined theoretically was also consistent with bremsstrahlung measurements and the scaling law of electron temperature contributed by resonance absorption.

In Addition, interesting emission patterns at 800 nm were observed from wedges and cones. These can be understood by the laser polarization dependencies in the cone target. CTR from wedge and cone targets suggest that quasi-static electromagnetic fields created on the target surfaces affect strongly the hot electron transport. CTR emission from the various angles of cones made in University of Nevada showed an evidence of hot electron flows guided by cone geometry, i.e. size of radiation is defined by the inside sharpness of the tip. This result suggests a potential for creating higher energy density and particle fluxes relevant to a variety of applications.

Transition radiation around $2\omega_0$ frequency has also been observed. Though the amount was very small compared with the fundamental frequency, this observation showed a clear evidence for the existence of multiple hot electron beams. At the narrow spectral range, around the half wavelength of the laser, CTR image from the target rear surface showed two distinct lobes in the emission spots. Analysis indicates that the two emission lobes are correlated with resonance absorption and $\boldsymbol{j} \times \mathbf{B}$ heating. We find that resonance absorption dominates the hot electron production by about an order of magnitude, though with a temperature which is about two thirds that of the electrons in the $\boldsymbol{j} \times \mathbf{B}$ peak. Three dimensional PIC simulations (VLPL) with the same parameters showed complete agreement with these experimental findings.

7.3. CONCLUSIONS

In conclusion, we had created fast electrons by irradiating ultra intense laser on the solid target with various structures. Through x-rays and optical emissions measurements in various spectral ranges along with theoretical analysis and computer simulations, we could expand our understandings about hot electron acceleration and transports dynamics in the relativistic energy regime. They are significant of our abilities to create and control higher energy and density plasmas, where we believe lot of interesting basic physics and applications lies within.

APPENDICIES

APPENDIX A. CTR - MATHEMATICA CODE

CTR caculation

J. Zheng, et al, Phys. Plasma. 10, 2994 (2003)

■ Constants

```
c = 3 * 10^8; (* m/s *)
```

■ Input Parameter

```
kT = 283; (* keV *)
d = 10; (* Target Thickness, micron, incidence Angle *)

index = 1; (* resonance Absorption → 1, jxB → 2 *)
θ = 45 * 2 Pi / 360; (* Degree *) (* Laser incidence angle,
Observation Angle *)
θ = 0 * 2 Pi / 360; (* e-beam moving angle, Degree *)


Nt = 100 000; (* Total number of step *)
Nb = 10; (* number of data points in single cycle *)

M = 15 * index; (* 40fs, resonance Absorption → 1,
jxB → 2 bunches per cycle *)
lamda = 800; (* wavelength nm *)
dt = (lamda * 10^-9 / c) / index // N; (* electron bunching cycle *)
w0 = 2 Pi * c / (lamda * 10^-9) // N; (* laser frequency *)
deltat = dt / Nb; (* Time step sec *)
deltaf = 1 / (Nt * deltat) // N; (* Frequency step size *)
```

■ Time and Frequency Table

```
TimeTable = Table[deltat * i, {i, 0, Nt - 1}];
fsTimeTable = TimeTable * 10^15;

FreqTable = Table[2 Pi * deltaf * i, {i, 0, Nt - 1}];
NFreqTable = FreqTable / w0;
```

■ t0 when the fastest electron reaches rear side of the target

$$t0 = \frac{d * 10^{-6}}{\text{Cos}[\theta]} \Big/ c \;//\; N; \quad (* \text{ sec } *)$$

$$\text{step} = \text{Round}\left[\frac{t0}{\text{deltat}}\right] + 1; \quad (* \text{ Number of time steps before t0 } *)$$

■ Eq. (37)

$$\beta[t\_] := \frac{t0}{t} \quad (* \text{ e}^- \text{ speed } *)$$

$$g[t\_] := \frac{\beta[t]^2 \text{Cos}[\theta]\,(\text{Sin}[\theta] - \beta[t]\,\text{Sin}[\theta])\,\text{Exp}\left[-\frac{511}{kT}\left(\left(1-\beta[t]^2\right)^{-1/2}-1\right)\right]}{\left((1-\beta[t]\,\text{Sin}[\theta]\,\text{Sin}[\theta])^2 - \beta[t]^2\,\text{Cos}[\theta]^2\,\text{Cos}[\theta]^2\right)\left(1-\beta[t]^2\right)^{3/2}}$$

```
SinglegTable = Join[Table[0, {step}],
   g[Take[TimeTable + 10^-24, -Nt + step]]] ;

gTable = Table[0, {Nt}];
For [i = 1, i ≤ M, i++,
  gTable += Join[Table[0, {Nb * (i - 1)}],
     Take[SinglegTable, Nt - Nb * (i - 1)]];
 ];

(* ListPlot[Transpose[{fsTimeTable,gTable}],
 PlotRange→{{t0*10^15,(t0+2M*dt)*10^15},All},Joined→True]
*)
```

■ $\text{Exp}[-q^2 a^2]$, where $q = (\omega / c)\,\text{Sin}[\theta]$, a=beam radius

```
qaTable = Exp[-NFreqTable^2 * Sin[θ]^2];
```

■ Fourier Transform of g[t]

```
CTR = 1/t0^2 * 1/kT^2 * qaTable * Abs[Fourier[gTable]]^2;

(* ListLogPlot[Transpose[{NFreqTable, CTR/CTR[[1]]}],
 PlotRange→{{0,3},{10^-12,1}},Joined→True]
*)

Print["T= ", kT, " keV , d= ", d, " micron"];
```

```
T= 283 keV , d= 10 micron
```

```
NFreqTable[[10001]]
```

```
1.
```

```
CTR[[10001]]
```

```
3.56521×10^18
```

```
NFreqTable[[20001]]
```

```
2.
```

```
CTR[[20001]]
```

```
1.48538×10^16
```

■ Eq. (40)

$$\text{Num}[t\_] := \frac{1}{kT}\,\frac{\beta[t]\,\text{Exp}\left[-\frac{511}{kT}\left(\left(1-\beta[t]^2\right)^{-1/2}-1\right)\right]}{t0\left(1-\beta[t]^2\right)^{3/2}}$$

```
SingleNumTable = Join[Table[0, {step}],
   Num[Take[TimeTable + 10^-24, -Nt + step]]];
NumTable = Table[0, {Nt}];
For [i = 1, i ≤ M, i++,
  NumTable += Join[Table[0, {Nb * (i - 1)}],
     Take[SingleNumTable, Nt - Nb * (i - 1)]];
 ];|

ListPlot[Transpose[{fsTimeTable, NumTable/Max[NumTable]}],
 PlotRange → {{t0 * 10^15, (t0 + 2 * M * dt) * 10^15}, All}, Joined → True]
```

APPENDIX B. KERR LENS MODE-LOCKING - MATHEMATICA CODE

KLM

– V. Magni, J. Opt Soc. Am B 12 (476)

```
(*
length dimension: mm
distance bet. M1( output coupler) to the M3( subresonator mirror):L1
distance
         bet. M4( high reflector) to the M4
   ( the other subresonator mirror):L2
distance bet. M3 to the interface of the crystal:a
crystal length:l
total path length  of the beam in the subresonator:b
angle at M3 :θ1              angle at M4 :θ2
focal length of subresonator mirrors:f
refractive index:n
*)
```

■ Input paramters

```
L2 = 653; L1 = 1297; l = 2; θ1 = 10 * Pi / 180; θ2 = 10 * Pi / 180;
f = 25;
n = 1.76;
```

■ Calculation of ABCD matrices

```
M1 = {{1, L1}, {0, 1}};(* Propagation of L1 *)
M2 = {{1, L2}, {0, 1}};(* Propagation of L2 *)
M3 = {{1, a}, {0, 1}};
(* propagation from M3 to the interface of the crystal *)
M4 = {{1, b - a - l}, {0, 1}};(* Propagation from the other interface to M4 *)


(* propagation in the medium *)
M5 = {{1, ξ}, {0, 1}};
M6 = {{1, (l - ξ)}, {0, 1}};
```

```
(* at mirror M3 *)
M7 = {{1, 0}, {-1 / f / Cos[θ1], 1}};(* tangenitial *)
M8 = {{1, 0}, {-1 / f * Cos[θ1], 1}};(* sagittal *)


(* at mirror M4*)
M9 = {{1, 0}, {-1 / f / Cos[θ2], 1}};(*tangenitial*)
M10 = {{1, 0}, {-1 / f * Cos[θ2], 1}};(*sagittal*)


(* incident Brewster interface tangenitial *)
M11 = {{n, 0}, {0, 1 / n^2}};
(* refractive Brewster interface tangenitial *)
M12 = {{1 / n, 0}, {0, n^2}};
(* incident Brewster interface sagittal *)
M14 = {{1, 0}, {0, 1 / n}};
(* refractive Brewster interface sagittal *)
M15 = {{1, 0}, {0, n}};
(* total path of the crystal *)
M13 = {{1, l}, {0, 1}};
```

■ ABCD matrices, T: tangential, S:sagittal

```
(* Each side of the crystal;to the left A, to the right B *)
AT = M1 . M7 . M3 . M12 . M5;
AS = M1 . M8 . M3 . M15 . M5;
BT = M2 . M9 . M4 . M12 . M6;
BS = M2 . M10 . M4 . M15 . M6;


(* Round trip *)
RT = M5 . M11 . M3 . M7 . M1 . M1 . M7 . M3 . M12 . M13 . M11 . M4 . M9 . M2 . BT;
RS = M5 . M14 . M3 . M8 . M1 . M1 . M8 . M3 . M15 . M13 . M14 . M4 . M10 . M2 . BS;

(* From M1 to M2 *)
TT = M2 . M9 . M4 . M12 . M13 . M11 . M3 . M7 . M1;
TS = M2 . M10 . M4 . M15 . M13 . M14 . M3 . M8 . M1;
```

▪ Kerr lens sensitivity at M1

```
Sx[a_, b_] := TT[[1, 1]] * TT[[2, 2]] + TT[[1, 2]] * TT[[2, 1]]
```

```
Sy[a_, b_] := TS[[1, 1]] * TS[[2, 2]] + TS[[1, 2]] * TS[[2, 1]]
```

```
Simplify[Sx[a, b]]
```

$$0.\,a^2 + a\left(-8.52651\times10^{-14} + 3.55271\times10^{-15}\,b\right) + 4.21606\,(-52.5391 + b)\,(-51.446 + b)$$

```
term1 = %[[3]]
```

$$4.21606\,(-52.5391 + b)\,(-51.446 + b)$$

```
Simplify[Sy[a, b]]
```

$$9.73702\times10^{-32}\,a^2 + a\left(6.50339\times10^{-14} - 1.24957\times10^{-15}\,b\right) + 3.96758\,(-52.5573 + b)\,(-51.4303 + b)$$

```
term2 = %[[3]]
```

$$3.96758\,(-52.5573 + b)\,(-51.4303 + b)$$

▪ Find the stability region

```
Solve[term1 == 1, b]
```

```
{{b → 51.2605}, {b → 52.7246}}
```

```
Solve[term1 == -1, b]
```

```
{{b → 51.7444}, {b → 52.2406}}
```

```
Solve[term2 == 1, b]
```

```
{{b → 51.2391}, {b → 52.7485}}
```

```
Solve[term2 == -1, b]
```

```
{{b → 51.738}, {b → 52.2497}}
```

▪ Kerr lens sensitivity

```
It = 50;
```

```
δx = δy = IdentityMatrix[It];
```

```
BADx[a_, b_, ξ_] := (Abs[RT[[1, 2]] / RS[[1, 2]]])^0.5 *
  D[BT[[1, 2]] * BT[[2, 2]] / RT[[1, 2]], ξ]
```

```
BADy[a_, b_, ξ_] := (Abs[RS[[1, 2]] / RT[[1, 2]]]) ^ 0.5 *
  D[BS[[1, 2]] * BS[[2, 2]] / RS[[1, 2]], ξ]

Timing[
 For [i = 1; q = 23; dq = (27 - 23) / It, i <= It, q += dq; i ++,
   For[j = 1; r = 51; dr = (53 - 51) / It, j <= It, r += dr; j ++,
     α = Sx[a, b] /. {a -> q, b -> r};
     β = Sy[a, b] /. {a -> q, b -> r};
     η = BADx[a, b, ξ] /. {a -> q, b -> r};
     μ = BADy[a, b, ξ] /. {a -> q, b -> r};

     If[ α < 1 && α > -1 && β < 1 && β > -1,
      ϕ = NIntegrate[η, {ξ, 0, 1}, Compiled -> True];
      φ = NIntegrate[μ, {ξ, 0, 1}, Compiled -> True];
      δx[[i, j]] = 1 / 2 / n * ((1 - β^2) / (1 - α^2)) ^ (0.25) * ϕ;
      δy[[i, j]] = 1 / 2 / n * ((1 - β^2) / (1 - α^2)) ^ (-0.25) * φ,

      δx[[i, j]] = 0; δy[[i, j]] = 0
     ];
    ];
  ];
]
δx = Transpose[δx];
δy = Transpose[δy];


ListContourPlot[δx, AxesLabel -> {"x", "y"}]

ListContourPlot[δy, AxesLabel -> {"x", "y"}]
```

APPENDIX C. WEDGE SIMULATION - OOPIC INPUT FILE

```
laser_solid.inp
{

This is a modification of original 'laser-solid.inp' file to simulate wedge targets.

Pulse with transverse half-sine profile and z polarization is launched from the left boundary.

We use Cartesian (2-D slab) geometry.
The bulk of target is a solid-density pre-ionized electron plasma and a stationary background of H+ ions.

Pre-plasma is ramping up linearly.    It can be turned on or off on purpose.

}

Variables
{
// General numerical parameters
   PI = 3.14159

// ***********************************************************************
// General physical parameters
// ***********************************************************************

   electronMass = 9.1094e-31
   electronCharge = -1.6022e-19
   permit = 8.8542e-12
   speedLight = 2.9979e8
   speedLight2 = speedLight*speedLight
   electronCharge2 = electronCharge*electronCharge
   qOverM = electronCharge/electronMass

   ionCharge = -electronCharge
   unitMassMKS = electronMass / 5.48579903e-04
   hydrogenMassNum = 1.00797
   hydrogenMass = unitMassMKS * hydrogenMassNum


// ***********************************************************************
```

```
// Plasma parameters
// ***********************************************************************
//     Here, we specify a zero plasma density, because we launch the laser
//     pulse into a vacuum region.    Down below, we define the parameters
//     used for loading the initial electron plasma into the simulation.

   elecPlasmaDensity =    0.0
   elecPlasmaFreq = sqrt(electronCharge*qOverM*elecPlasmaDensity/permit)


// ***********************************************************************
// Laser pulse parameters - z polarization
// ***********************************************************************
//     We are modeling a laser pulse with wavelength of 0.8 micron and
//     FHWM pulse length of ~40 fs, and a peak intensity of ~10^19 W/cm^2
//
//     We are using a half sine function for the longitudinal shape of
//     the pulse and Gaussians for the transverse directions with the
//     same standard deviations sigma_r, same as waistSize below.
//
//     The energy of the pulse is ~600 mJ.
//
//     In terms of the energy of the pulse [J], called here "energyOfPulse",
//     the FHWM pulse length [s] "pulseLengthFWHM" and the transverse
//     width "waistSize" [m], the peak laser intensity is given by:
//
//     Ipeak = (2*energyOfPulse)/(1.5*pulseLengthFWHM*PI*waistSize^2)
//               ~ 4e23 W/m^2
//               ~ 4e19 W/cm^2

   energyOfPulse =      600.0e-03          // [J]
   pulseLengthFWHM =    40.0e-15           // [s]
   waistSize =                3.5e-06      // [m]
   laserWavelength =      0.8e-06          // [m]
   laserFrequency = 2.*PI*speedLight/laserWavelength
   peakElectricField                                                    =
sqrt(8.*energyOfPulse/(1.5*permit*speedLight*pulseLengthFWHM*PI*waistSize*waist
Size))

// ***********************************************************************
// More laser parameters:
// ***********************************************************************
// We model the laser pulse envelope as a Gaussian (nPulseShape=1).
// or a half sine shape (nPulseShape=2)
```

```
   nPulseShape = 1
   pulseLength    = 1.5 * pulseLengthFWHM * speedLight

// Here we specify Rayleigh length, etc.
// These parameters are for a pulse with z-polarization.

   angFreq = laserFrequency
   angFreq2 = angFreq * angFreq
   waveVector = sqrt( (angFreq2-elecPlasmaFreq*elecPlasmaFreq) / speedLight2 )
   rayleighLength = waistSize * waistSize * waveVector / 2.
   waistLocation = numZeroCells * dx *(19/8)


// ************************************************************************
// Grid parameters
// ************************************************************************
// We must resolve the laser wavelength

   numGridsPerWavelength = 16
   dx = laserWavelength / numGridsPerWavelength
   Nx =32 * numGridsPerWavelength
   Lx = Nx * dx

   gridSizeRatio = 1
   dy = dx * gridSizeRatio
   Ny = 32 * numGridsPerWavelength / gridSizeRatio
   Ly = Ny * dy

   d = 1. / sqrt( 1./(dx*dx) + 1./(dy*dy) )
   timeStep = 0.99 * d / speedLight


// ************************************************************************
// Plasma parameters
// ************************************************************************
// An electron density of 1.736e+27 m^-3 leads to a plasma wavelength of 0.8 microns.

//    plasmaDensityMKS = 1.736e+27
//    plasmaDensityMKS = 14*1.736e+27
   plasmaDensityMKS = 8*1.736e+27
   preplasmaDensityMKS = 2*1.736e+27

   numZeroCells       =      8 * numGridsPerWavelength
```

```
   numSlabCells_H    =    16.0 * numGridsPerWavelength

   numPlasmaCellsX = numSlabCells_H
   numPlasmaCellsY = Ny
   numPlasmaCells    = numPlasmaCellsX * numPlasmaCellsY

   totalNumElectrons    = plasmaDensityMKS * dx * dy * 1.0 * numPlasmaCellsY *
numPlasmaCellsX
   numPtclsPerCell       = 8
   totalNumMacroPtcls = numPtclsPerCell * numPlasmaCells
   np2cRatio                  = totalNumElectrons / totalNumMacroPtcls

}


Region
{

Grid
{
   J = Nx
   x1s = 0.0
   x1f = Lx
   n1 = 1.0
   K = Ny
   x2s = 0.0
   x2f = Ly
   n2 = 1.0
   Geometry = 1
//    PeriodicFlagX2 = 1
}

Control
{
   dt = timeStep
   initPoissonSolve=0
}

// Define the electron macro-particles
Species
{
   name = electrons
   m = electronMass
   q = electronCharge
```

```
}

// Define the H+ species (no macro-particles will be generated).
Species
{
   name = Hydrogen
   m = hydrogenMass
   q = ionCharge
}

// Load the plasma electrons over a solid region within the grid, covering the H.
Load
{
   speciesName = electrons
//    density = plasmaDensityMKS
  analyticF                =                plasmaDensityMKS*(1-step(x2-(1/4*Ny*dy)-(x1-
numZeroCells*dx)*0.713)*step(-x2+(3/4*Ny*dy)-(x1-(numZeroCells)*dx)*0.713))

   x1MinMKS = numZeroCells * dx
   x1MaxMKS = (numZeroCells + numSlabCells_H) * dx
   x2MinMKS = 0.
   x2MaxMKS = Ly

   np2c = np2cRatio

// Specify loading that is more uniform than random
   LoadMethodFlag = 1
}


// Load the uniform, fixed H+ions over the H slab.
Load
{
   speciesName = Hydrogen
//    density = plasmaDensityMKS
   analyticF                =                plasmaDensityMKS*(1-step(x2-(1/4*Ny*dy)-(x1-
numZeroCells*dx)*0.713)*step(-x2+(3/4*Ny*dy)-(x1-(numZeroCells)*dx)*0.713))

   x1MinMKS = numZeroCells * dx
   x1MaxMKS = (numZeroCells + numSlabCells_H) * dx
   x2MinMKS = 0.
   x2MaxMKS = Ly

// This specifies a static uniform background (no macro-particles).
```

```
   np2c = 0
}



// // Load the PRE PLASMA in the cone
//
// // Load the pre plasma electrons
// Load
// {
//     speciesName = electrons
// //   density = plasmaDensityMKS
//                          analyticF          =          preplasmaDensityMKS*(ramp(x1-
numZeroCells*dx)/(numZeroCells*dx)*0.713)*(step(x2-(1/4*Ny*dy)-(x1-
numZeroCells*dx)*0.713)*step(-x2+(3/4*Ny*dy)-(x1-(numZeroCells)*dx)*0.713))
//
//     x1MinMKS = numZeroCells * dx
//     x1MaxMKS = (numZeroCells + numSlabCells_H) * dx
//     x2MinMKS = 0.
//     x2MaxMKS = Ly
//
//     np2c = np2cRatio
//
// // Specify loading that is more uniform than random
//     LoadMethodFlag = 1
// }
//
// // Load the pre plasma H+ions.
// Load
// {
//     speciesName = Hydrogen
// //   density = plasmaDensityMKS
//                              analyticF          =          preplasmaDensityMKS*(ramp(x1-
numZeroCells*dx)/(numZeroCells*dx)*0.713)*(step(x2-(1/4*Ny*dy)-(x1-
numZeroCells*dx)*0.713)*step(-x2+(3/4*Ny*dy)-(x1-(numZeroCells)*dx)*0.713))
//
//     x1MinMKS = numZeroCells * dx
//     x1MaxMKS = (numZeroCells + numSlabCells_H) * dx
//     x2MinMKS = 0.
//     x2MaxMKS = Ly
//
// // This specifies a static (fixed) uniform background (no macro-particles).
//     np2c = 0
// // This specifies a mobile (no macro-particles).
```

```
// //      np2c = np2cRatio
// }



// Launch the laser pulse
// This subsequently applies conducting boundary conditions along the left boundary.    It would be good if this could become an ExitPort...

PortGauss
{
   j1 = 0
   j2 = 0
   k1 = 0
   k2 = Ny
   normal = 1

   A = 0
   C = 1.0

// Wave (0) - polarization in y-direction
   pulShp_p0 = nPulseShape
   tdelay_p0 = 0.0
   pulLeng_p0 = pulseLength
   chirp_p0 = 0.0
   spotSize_p0 = waistSize
   waveLeng_p0 = laserWavelength
   focus_p0 = waistLocation
   amp_p0 =    peakElectricField


// Wave (1) - polarization in z-direction
   pulShp_p1 = nPulseShape
   tdelay_p1 = 0.0
   pulLeng_p1 = pulseLength
   chirp_p1 = 0.0
   spotSize_p1 = waistSize
   waveLeng_p1 = laserWavelength
   focus_p1 = waistLocation
   amp_p1 = 0.0

   EFFlag = 0
   name = PortGauss
}
```

```
// Top boundary
Conductor
{
   j1 = 0
   j2 = Nx
   k1 = Ny
   k2 = Ny
   normal = -1
}

// Bottom boundary
Conductor
{
   j1 = 0
   j2 = Nx
   k1 = 0
   k2 = 0
   normal = 1
}

// Right boundary
ExitPort
{
   j1 = Nx
   j2 = Nx
   k1 = 0
   k2 = Ny
   normal = -1
   EFFlag = 0
   name = ExitPort
   C = 0
   A = 0
}

}
```

APPENDIX D. SINGLE SHOT AND DETECTOR TRIGGER SETTING

Though the THOR operates 10Hz, all experiments in thesis were performed in a single shot mode. Basic timing setups were shown in Will Grigsby's Ph.D thesis [61], however, here I used a simpler setup for single shot operation. 'RED button' box consisting of a few 555 timer ICs and associated components generates a 5 V, 95 ms square pulse. This pulse and 10 Hz signal from the timing box in the laser room combines in the 'AND box'. 'AND box' is utilizing a NAND IC and 555 chip, and generate 5 V output and sending it to the 'UNIBLITZ' driver, of which setting is 'remote'

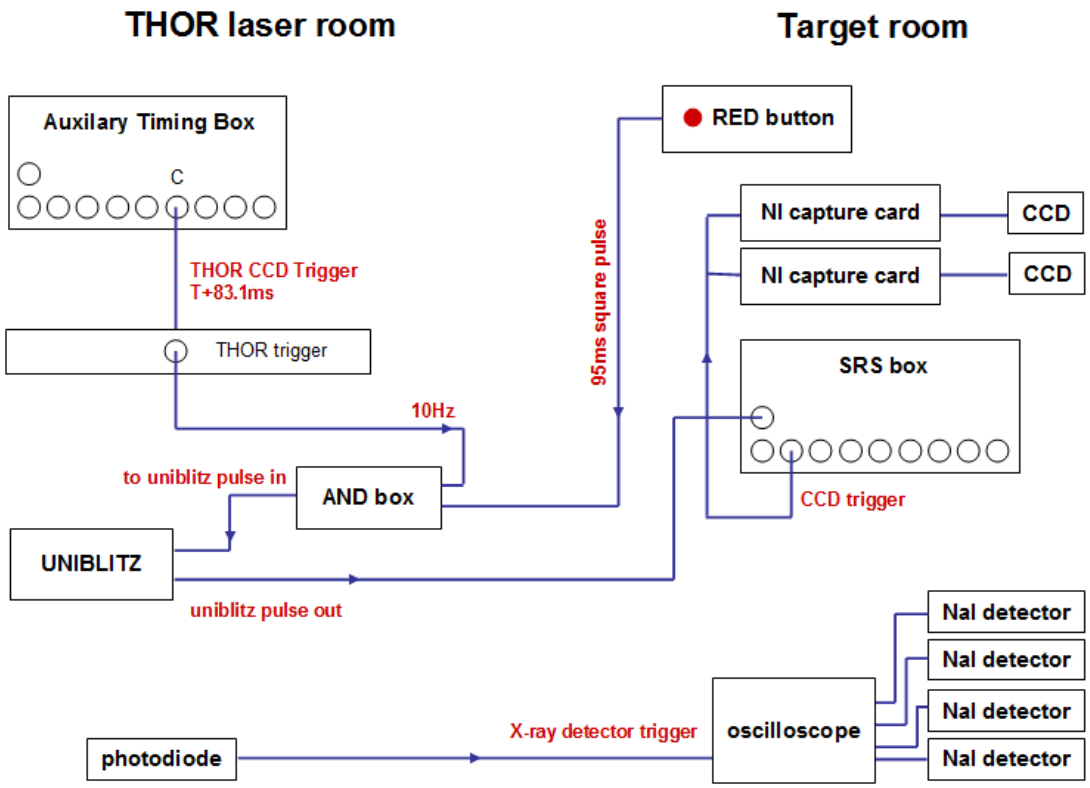

Figure 79. Diagram showing single shot operation wiring and detector triggers. Auxiliary timing box is the down-left box in the rack 2. A photodiode for x-ray detector trigger is located after the final spatial filter before the vacuum compressor.

and ‘N.O’. Since the pulse length from the ‘RED button’ is 95 ms and the THOR trigger is 10 Hz, there is ~ 5 % of chance that output pulse from the ‘AND box’ does not generate; i.e the laser does not fire. In most case, output from the ‘UNIBLITZ’ driver could be used for direct CCD trigger in the target room. If necessary, some delay also could be added using SRS box in the target area.

Trigger for x-ray detectors were separated from the above electronics. A photodiode installed after the final vacuum special filter picks up scattered light and sends a pulse to an oscilloscope. Rising edge of it is used to trigger NaI detectors. To avoid saturation of signal from photodiode, it is filtered with thick ND filters. Therefore the magnitude of this signal could be also used to monitor laser pulse energy.

APPENDIX E. OZONE CLEANING OF THE GRATING IN THE COMPRESSOR

Because of high fluence of compressed laser pulse, the surface of compression grating is contaminated with hydrocarbon compounds, which might be mainly originated from oils from the vacuum pumps. After several years of the THOR operation the reflectivity of the grating is degraded, so ozone shower with halogen lamp is used for getting rid of hydrocarbons and helps increasing the reflectivity of the grating and whole throughput of compressor. The closer the lamp is installed to the grating, the more effective ozone breaks down hydrocarbons. We set it within 5 mm from the grating surface and turn it on for 48 ~ 72 hours. After the cleaning, transmission of the whole compressor was determined by measuring laser pulse energy at various points (See Table 3). Amplified laser beam was divided using a beam splitter and sent to the compressor. Since an aperture size of power meter is smaller than the beam diameter after the final collimation lens, a 3" uncoated positive lens was used for collecting beam. Transmission of this lens was 89.3%. The total transmission of after the final amplifying stage is ~ 47%. As a result, about 560 mJ of laser energy in a pulse can be delivered on the target. After cleaning is completed, pulse length need to be checked using second order autocorrelator to ensure grating alignment is fine.

	Position 1	Position 2	Position 3	Position 4
w/o collecting optics	71.7 mJ	69.3 mJ	-	-
w/ collecting optics	-	61.9 mJ	52.6 mJ	30.0 mJ
Net energy	71.7 mJ	69.3 mJ	63.0 mJ	33.6 mJ
Transmission	1	0.95	0.88	0.47

Table 3. Pulse energy measurements at various points; before (position 1) and after (position 2) the final vacuum spatial filter, after the final collimation lens (position 3), and at the blue chamber (position 4).

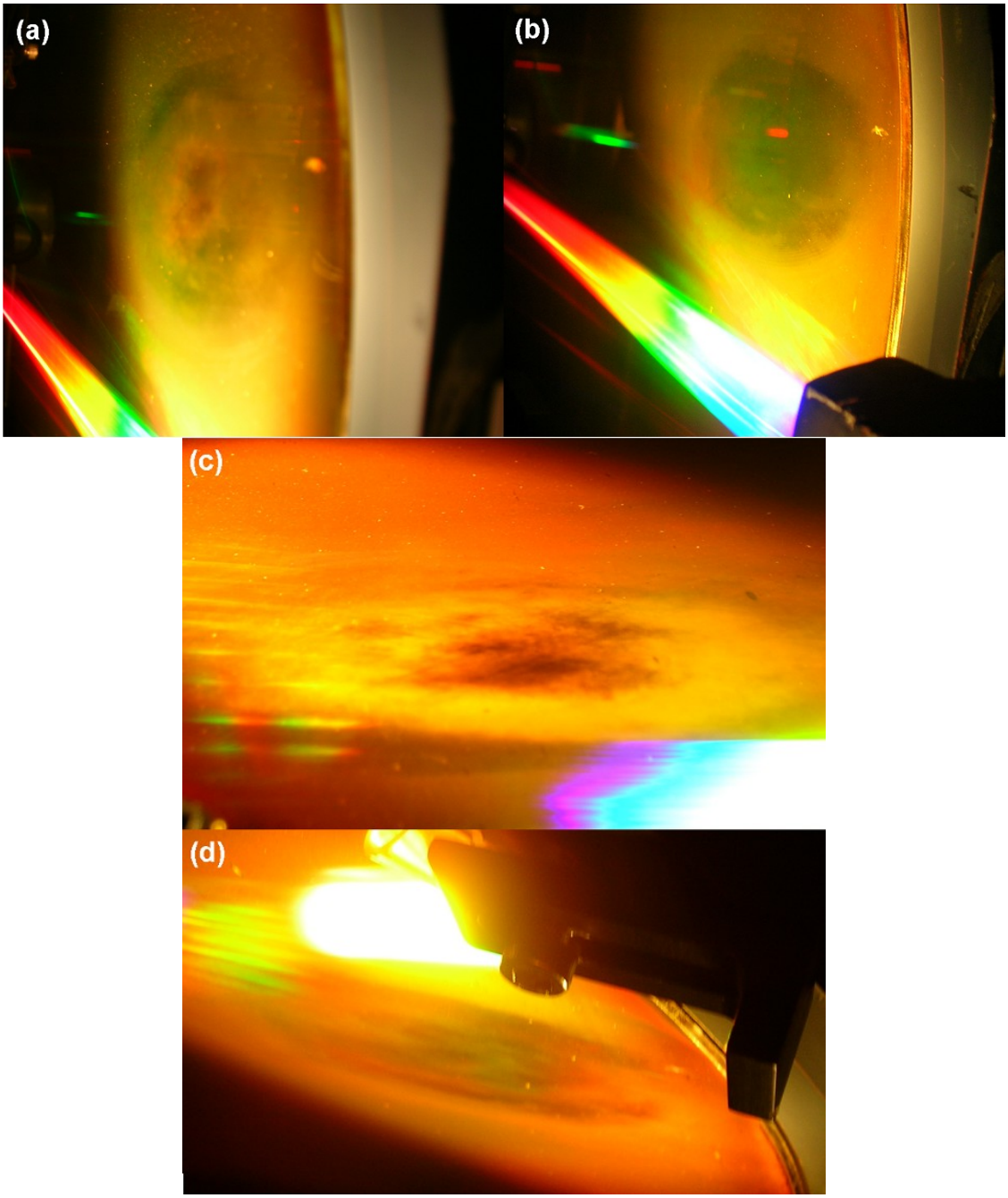

Figure 80. Photographs of the compressor grating. (a.c) Before and (b.d) after the ozone cleaning (03/13/08 ~ 03/16/08).

BIBLIOGRAPHY

1. W. L. Kruer and K. Estabrook, "J x B heating by very intense laser light," Physics of Fluids **28**, 430-432 (1985).

2. S. C. Wilks, W. L. Kruer, M. Tabak, and A. B. Langdon, "Absorption of ultra-intense laser pulses," Physical Review Letters **69**, 1383 (1992).

3. F. Brunel, "Not-so-resonant, resonant absorption," Physical Review Letters **59**, 52 (1987).

4. A. Pukhov and J. Meyer-ter-Vehn, "Relativistic laser-plasma interaction by multi-dimensional particle-in-cell simulations," in *The 39th annual meeting of division of plasma physics of APS*, (AIP, 1998), 1880-1886.

5. M. Chen, Z. M. Sheng, and J. Zhang, "On the angular distribution of fast electrons generated in intense laser interaction with solid targets," Phys. Plasmas **13**, 014504-014504 (2006).

6. J. S. Green, V. M. Ovchinnikov, R. G. Evans, K. U. Akli, H. Azechi, F. N. Beg, C. Bellei, R. R. Freeman, H. Habara, R. Heathcote, M. H. Key, J. A. King, K. L. Lancaster, N. C. Lopes, T. Ma, A. J. MacKinnon, K. Markey, A. McPhee, Z. Najmudin, P. Nilson, R. Onofrei, R. Stephens, K. Takeda, K. A. Tanaka, W. Theobald, T. Tanimoto, J. Waugh, L. Van Woerkom, N. C. Woolsey, M. Zepf, J. R. Davies, and P. A. Norreys, "Effect of Laser Intensity on Fast-Electron-Beam Divergence in Solid-Density Plasmas," Physical Review Letters **100**, 015003-015004 (2008).

7. F. N. Beg, A. R. Bell, A. E. Dangor, C. N. Danson, A. P. Fews, M. E. Glinsky, B. A. Hammel, P. Lee, P. A. Norreys, and M. Tatarakis, "A study of picosecond laser--solid interactions up to 10^19 W cm^-2," Physics of Plasmas **4**, 447-457 (1997).

8. M. D. Perry, J. A. Sefcik, T. Cowan, S. Hatchett, A. Hunt, M. Moran, D. Pennington, R. Snavely, and S. C. Wilks, "Hard x-ray production from high intensity laser solid interactions (invited)," in *Proceedings of the 12th topical conference on high temperature plasma diagnostics*, (AIP, 1999), 265-269.

9. D. C. Eder, G. Pretzler, E. Fill, K. Eidmann, and A. Saemann, "Spatial characteristics of Ka radiation from weakly relativistic laser plasmas," Applied Physics B: Lasers and Optics **70**, 211-217 (2000).

10. A. J. Mackinnon, Y. Sentoku, P. K. Patel, D. W. Price, S. Hatchett, M. H. Key, C. Andersen, R. Snavely, and R. R. Freeman, "Enhancement of Proton Acceleration by Hot-Electron Recirculation in Thin Foils Irradiated by Ultraintense Laser Pulses," Physical Review Letters **88**, 215006 (2002).

11. R. A. Snavely, M. H. Key, S. P. Hatchett, T. E. Cowan, M. Roth, T. W. Phillips, M. A. Stoyer, E. A. Henry, T. C. Sangster, M. S. Singh, S. C. Wilks, A. MacKinnon, A. Offenberger, D. M. Pennington, K. Yasuike, A. B. Langdon, B. F. Lasinski, J. Johnson, M. D. Perry, and E. M. Campbell, "Intense High-Energy Proton Beams from Petawatt-Laser Irradiation of Solids," Physical Review Letters **85**, 2945-2948 (2000).

12. J. Fuchs, P. Antici, E. d/'Humieres, E. Lefebvre, M. Borghesi, E. Brambrink, C. A. Cecchetti, M. Kaluza, V. Malka, M. Manclossi, S. Meyroneinc, P. Mora, J. Schreiber, T. Toncian, H. Pepin, and P. Audebert, "Laser-driven proton scaling laws and new paths towards energy increase," Nature Physics **2**, 48-54 (2006).

13. R. Kodama, P. A. Norreys, K. Mima, A. E. Dangor, R. G. Evans, H. Fujita, Y. Kitagawa, K. Krushelnick, T. Miyakoshi, N. Miyanaga, T. Norimatsu, S. J. Rose, T. Shozaki, K. Shigemori, A. Sunahara, M. Tampo, K. A. Tanaka, Y. Toyama, T. Yamanaka, and M. Zepf, "Fast heating of ultrahigh-density plasma as a step towards laser fusion ignition," Nature **412**, 798-802 (2001).

14. Z. L. Chen, R. Kodama, M. Nakatsutsumi, H. Nakamura, M. Tampo, K. A. Tanaka, Y. Toyama, T. Tsutsumi, and T. Yabuuchi, "Enhancement of energetic electrons and protons by cone guiding of laser light," Physical Review E **71**, 036403-036405 (2005).

15. G. Dyer, R. Sheppherd, J. Kuba, E. Fill, A. Wootton, P. Patel, D. Price, and T. Ditmire, "Isochoric heating of solid aluminium with picosecond X-ray pulses," Journal of Modern Optics **50**, 2495-2505 (2003).

16. G. Dyer, "Experimental Study of the Equation of State of Isochorically Heated Warm Dense Matter," Ph.D. Thesis - University of Texas at Austin (2007).

17. A. Tauschwitz, E. Brambrink, J. A. Maruhn, M. Roth, M. Schollmeier, T. Schlegel, and A. Tauschwitz, "Laser-produced proton beams as a tool for equation-of-state studies of warm dense matter," High Energy Density Physics **2**, 16-20 (2006).

18. R. Kodama, Y. Sentoku, Z. L. Chen, G. R. Kumar, S. P. Hatchett, Y. Toyama, T. E. Cowan, R. R. Freeman, J. Fuchs, Y. Izawa, M. H. Key, Y. Kitagawa, K. Kondo, T. Matsuoka, H. Nakamura, M. Nakatsutsumi, P. A. Norreys, T. Norimatsu, R. A. Snavely, R. B. Stephens, M. Tampo, K. A. Tanaka, and T.

Yabuuchi, "Plasma devices to guide and collimate a high density of MeV electrons," Nature **432**, 1005-1008 (2004).

19. Y. Sentoku, K. Mima, H. Ruhl, Y. Toyama, R. Kodama, and T. E. Cowan, "Laser light and hot electron micro focusing using a conical target," Phys. Plasmas **11**, 3083-3087 (2004).

20. L. Van Woerkom, K. U. Akli, T. Bartal, F. N. Beg, S. Chawla, C. D. Chen, E. Chowdhury, R. R. Freeman, D. Hey, M. H. Key, J. A. King, A. Link, T. Ma, A. J. MacKinnon, A. G. MacPhee, D. Offermann, V. Ovchinnikov, P. K. Patel, D. W. Schumacher, R. B. Stephens, and Y. Y. Tsui, "Fast electron generation in cones with ultraintense laser pulses," Physics of Plasmas **15**, 056304-056306 (2008).

21. Y. Oishi, T. Nayuki, K. Nemoto, Y. Okano, Y. Hironaka, K. G. Nakamura, and K.-i. Kondo, "Production of relativistic electrons by irradiation of 43-fs-laser pulses on copper film," Applied Physics Letters **79**, 1234-1236 (2001).

22. M. H. Key, M. D. Cable, T. E. Cowan, K. G. Estabrook, B. A. Hammel, S. P. Hatchett, E. A. Henry, D. E. Hinkel, J. D. Kilkenny, J. A. Koch, W. L. Kruer, A. B. Langdon, B. F. Lasinski, R. W. Lee, B. J. MacGowan, A. MacKinnon, J. D. Moody, M. J. Moran, A. A. Offenberger, D. M. Pennington, M. D. Perry, T. J. Phillips, T. C. Sangster, M. S. Singh, M. A. Stoyer, M. Tabak, G. L. Tietbohl, M. Tsukamoto, K. Wharton, and S. C. Wilks, "Hot electron production and heating by hot electrons in fast ignitor research," in *The 39th annual meeting of division of plasma physics of APS*, (AIP, 1998), 1966-1972.

23. M. I. K. Santala, M. Zepf, I. Watts, F. N. Beg, E. Clark, M. Tatarakis, K. Krushelnick, A. E. Dangor, T. McCanny, I. Spencer, R. P. Singhal, K. W. D. Ledingham, S. C. Wilks, A. C. Machacek, J. S. Wark, R. Allott, R. J. Clarke, and P. A. Norreys, "Effect of the Plasma Density Scale Length on the Direction of Fast Electrons in Relativistic Laser-Solid Interactions," Physical Review Letters **84**, 1459 (2000).

24. S. Ter-Avetisyan, M. Schnurer, T. Sokollik, P. V. Nickles, W. Sandner, H. R. Reiss, J. Stein, D. Habs, T. Nakamura, and K. Mima, "Proton acceleration in the electrostatic sheaths of hot electrons governed by strongly relativistic laser-absorption processes," Physical Review E **77**, 016403-016405 (2008).

25. F. Brandl, G. Pretzler, D. Habs, and E. Fill, "Cerenkov radiation diagnostics of hot electrons generated by fs-laser interaction with solid targets," EPL (Europhysics Letters) **61**, 632-638 (2003).

26. V. L. Ginzburg and I. M. Frank, "Radiation of a uniformly moving electron due to its transition from one medium into another," Zh. Eksp. Teor. Fiz **16**, 15-28 (1946).

27. S. D. Baton, J. J. Santos, F. Amiranoff, H. Popescu, L. Gremillet, M. Koenig, E. Martinolli, O. Guilbaud, C. Rousseaux, M. Rabec Le Gloahec, T. Hall, D. Batani, E. Perelli, F. Scianitti, and T. E. Cowan, "Evidence of Ultrashort Electron Bunches in Laser-Plasma Interactions at Relativistic Intensities," Physical Review Letters **91**, 105001 (2003).

28. J. J. Santos, F. Amiranoff, S. D. Baton, L. Gremillet, M. Koenig, E. Martinolli, M. Rabec Le Gloahec, C. Rousseaux, D. Batani, A. Bernardinello, G. Greison, and T. Hall, "Fast Electron Transport in Ultraintense Laser Pulse Interaction with Solid Targets by Rear-Side Self-Radiation Diagnostics," Physical Review Letters **89**, 025001 (2002).

29. J. J. Santos, A. Debayle, P. Nicolai, V. Tikhonchuk, M. Manclossi, D. Batani, A. Guemnie-Tafo, J. Faure, V. Malka, and J. J. Honrubia, "Fast-electron transport and induced heating in aluminum foils," Physics of Plasmas **14**, 103107-103118 (2007).

30. J. Zheng, K. A. Tanaka, T. Miyakoshi, Y. Kitagawa, R. Kodama, T. Kurahashi, and T. Yamanaka, "Theoretical study of transition radiation from hot electrons generated in the laser--solid interaction," Physics of Plasmas **10**, 2994-3003 (2003).

31. J. Zheng, K. A. Tanaka, T. Sato, T. Yabuuchi, T. Kurahashi, Y. Kitagawa, R. Kodama, T. Norimatsu, and T. Yamanaka, "Study of Hot Electrons by Measurement of Optical Emission from the Rear Surface of a Metallic Foil Irradiated with Ultraintense Laser Pulse," Physical Review Letters **92**, 165001-165004 (2004).

32. B. I. Cho, G. M. Dyer, S. Kneip, S. Pikuz, D. R. Symes, A. C. Bernstein, Y. Sentoku, N. R.-L. Galloudec, T. E. Cowan, and T. Ditmire, "Hot electron generation from intense laser irradiation of microtipped cone and wedge targets," Physics of Plasmas **15**, 052701-052706 (2008).

33. B. I. Cho, J. Osterholz, N. Renard-Le Galloudec, A. C. Bernstein, G. Dyer, and T. Ditmire, "Study of hot electron transport in foil, wedge, and cone targets irradiated with ultraintense laser pulses," J. Opt. Soc. Am. B **25**, B50-B56 (2008).

34. B. I. Cho, J. Osterholz, A. Bernstein, G. M. Dyer, A. Karmakar, A. Pukhov, and T. Ditmire, "Observation of Two Distinct Hot Electron Beams in Intense Laser-Solid Interactions," Physical Review Letters (submitted).

35. N. Renard-Le Galloudec, B. I. Cho, J. Osterholz, and T. Ditmire, "Controlled reproducible alignment of cone targets and mitigation of preplasma in high intensity laser interactions," Review of Scientific Instruments (submitted).

36. P. Gibbon and E. Forster, "Short-pulse laser - plasma interactions," Plasma Physics and Controlled Fusion **38**, 769 (1996).

37. W. L. Kruer, "The Physics of Laser Plasma Interactions," Westview Press (2003).

38. M. K. Grimes, A. R. Rundquist, Y. S. Lee, and M. C. Downer, "Experimental Identification of "Vacuum Heating" at Femtosecond-Laser-Irradiated Metal Surfaces," Physical Review Letters **82**, 4010 (1999).

39. W. L. Kruer and S. C. Wilks, "Advances in Plasma Physics," Woodbury, NY: AIP (1994).

40. S. C. Wilks and W. L. Kruer, "Absorption of ultrashort, ultra-intense laser light by solids and overdense plasmas," Quantum Electronics, IEEE Journal of **33**, 1954-1968 (1997).

41. V. T. Tikhonchuk, "Interaction of a beam of fast electrons with solids," Physics of Plasmas **9**, 1416-1421 (2002).

42. F. Pisani, A. Bernardinello, D. Batani, A. Antonicci, E. Martinolli, M. Koenig, L. Gremillet, F. Amiranoff, S. Baton, J. Davies, T. Hall, D. Scott, P. Norreys, A. Djaoui, C. Rousseaux, P. Fews, H. Bandulet, and H. Pepin, "Experimental evidence of electric inhibition in fast electron penetration and of electric-field-limited fast electron transport in dense matter," Physical Review E **62**, R5927 (2000).

43. D. W. Forslund, J. M. Kindel, and K. Lee, "Theory of Hot-Electron Spectra at High Laser Intensity," Physical Review Letters **39**, 284 (1977).

44. A. Rousse, P. Audebert, J. P. Geindre, F. Falli, J. C. Gauthier, A. Mysyrowicz, G. Grillon, and A. Antonetti, "Efficient K alpha x-ray source from femtosecond laser-produced plasmas," Physical Review E **50**, 2200 (1994).

45. A. R. Bell, J. R. Davies, S. Guerin, and H. Ruhl, "Fast-electron transport in high-intensity short-pulse laser - solid experiments," Plasma Physics and Controlled Fusion **39**, 653-659 (1997).

46. H. Alfven, "On the Motion of Cosmic Rays in Interstellar Space," Physical Review **55**, 425 (1939).

47. F. F. Chen, "Introduction to Plasma Physics and Controlled Fusion," Plenum Press (1984).

48. E. S. Weibel, "Spontaneously Growing Transverse Waves in a Plasma Due to an Anisotropic Velocity Distribution," Physical Review Letters **2**, 83 (1959).

49. A. Bret, M. C. Firpo, and C. Deutsch, "Collective electromagnetic modes for beam-plasma interaction in the whole k space," Physical Review E **70**, 046401 (2004).

50. A. Bret, "A simple analytical model for the Weibel instability in the non-relativistic regime," Physics Letters A **359**, 52-55 (2006).

51. B. Basu, "Moment equation description of Weibel instability," Physics of Plasmas **9**, 5131-5134 (2002).

52. A. Thompson, D. Vaughan, J. Kirz, D. Attwood, E. Gullikson, M. Howells, K. Kim, J. Kortright, I. Lindau, P. Pianetta, A. Robinson, J. Underwood, G. WIlliams, and H. Winick, "X-ray Data Booklet," Lawrence Berkeley National Laboratory (2001).

53. Y. B. Zel'dovich and Y. P. Raizer, "Physics of Shock Waves and High-Temperature Hydrodynamic Phenomena," Academic Press, Inc., New York (2002).

54. L. D. Landau and E. M. Lifshitz, "Fluid Mechanics," Addison-Wesley, Reading, Mass. (1959).

55. M. L. Ter-Mikaelian, "High-Energy Electromagnetic Processes in Condensed Media," John Wiley & Sons, Inc. (1972).

56. P. F. Moulton, "Spectroscopic and laser characteristics of Ti:Al2O3," J. Opt. Soc. Am. B **3**, 125 (1986).

57. D. Strickland and G. Mourou, "Compression of amplified chirped optical pulses," Optics Communications **56**, 219-221 (1985).

58. B. E. A. Saleh and M. C. Teich, "Fundamentals of Photonics," John Wiley & Sons, Inc. (1991).

59. V. Magni, G. Cerullo, S. De Silvestri, and A. Monguzzi, "Astigmatism in Gaussian-beam self-focusing and in resonators for Kerr-lens mode locking," J. Opt. Soc. Am. B **12**, 476 (1995).

60. G. Hays, "Development of Broad Spectrum Technologies for High Energy Chirped Pulse Amplification," Ph.D. Thesis - University of Texas at Austin (2007).

61. W. Grigsby, "Experimental Studies of High Energy Density Silicon Using Ultra-Fast Lasers," Ph.D. Thesis - University of Texas at Austin (2007).

62. A. Brun, P. Georges, G. L. Saux, and F. Salin, "Single-shot characterization of ultrashort light pulses," Journal of Physics D: Applied Physics **24**, 1225-1233 (1991).

63. H. A. Sumeruk, S. Kneip, D. R. Symes, I. V. Churina, A. V. Belolipetski, G. Dyer, J. Landry, G. Bansal, A. Bernstein, T. D. Donnelly, A. Karmakar, A. Pukhov, and T. Ditmire, "Hot electron and x-ray production from intense laser irradiation of wavelength-scale polystyrene spheres," Physics of Plasmas **14**, 062704-062709 (2007).

64. Y. Cho, T. Kuki, Y. Fukuta, H. Fujita, and B. Kim, "Fabrication of sharp knife-edged micro probe card combined with shadow mask deposition," Sensors and Actuators A: Physical **114**, 327-331 (2004).

65. A. E. Siegman, "Lasers," University Science Books (1986).

66. E. Hecht, "Optics," Addison-Wesley (1998).

67. L. V. Hamos, "X-ray spectroscopy and image formation with curved crystal reflectors. I. Geometrical-optical considerations," Annalen der Physik **17**, 716-724 (1933).

68. A. Shevelko, A. Antonov, I. Grigorieva, Y. Kasyanov, and O. Yakushev, "X-ray Focusing crystal Von Hamos Spectrometer with a CCD linear Array as a Detector," Advanced in X-ray Analysis **45**, 433 (2002).

69. J. P. Geindre, P. Audebert, A. Rousse, J. C. Gauthier, A. Y. Faenov, T. A. Pikuz, S. A. Pikuz, and T. A. Shelkovenko, "FSSR mica spherical crystal spectrometer with CCD detector for high-resolution x-ray spectroscopy of femtosecond laser produced plasma," Physica Scripta **53**, 645-647 (1996).

70. S. Kneip, "X-Ray And Hot Electron Enhancement With Advanced Targets Irradiated by Ultra-High Intensity Laser," Master Dissertation - University of Texas at Austin (2005).

71. J. H. Hubbell and S. M. Seltzer, "Tables of X-Ray Mass Attenuation Coefficients and Mass Energy-Absorption Coefficients from 1 keV to 20 MeV for Elements Z = 1 to 92 and 48 Additional Substances of Dosimetric Interest," http://physics.nist.gov/PhysRefData/XrayMassCoef/cover.html (1996).

72. K. Sato, M. Shikida, Y. Matsushima, T. Yamashiro, K. Asaumi, Y. Iriye, and M. Yamamoto, "Characterization of orientation-dependent etching properties of single-crystal silicon: effects of KOH concentration," Sensors and Actuators A **64**, 87-93 (1998).

73. E. Foerster, J. Heinisch, P. Heist, G. Hoelzer, I. Uschmann, F. Scholze, and F. Schaefer, "Measurements of the integrated reectivity of elastically bent crystals," In BESSY Annu. Rep., 481-483 (1992).

74. B. L. Henke, F. G. Fujiwara, M. A. Tester, C. H. Dittmore, and M. A. Palmer, "Low-energy x-ray response of photographic films. II. Experimental characterization," J. Opt. Soc. Am. B **1**, 828 (1984).

75. Y. T. Li, X. H. Yuan, M. H. Xu, Z. Y. Zheng, Z. M. Sheng, M. Chen, Y. Y. Ma, W. X. Liang, Q. Z. Yu, Y. Zhang, F. Liu, Z. H. Wang, Z. Y. Wei, W. Zhao, Z. Jin, and J. Zhang, "Observation of a Fast Electron Beam Emitted along the Surface of a Target Irradiated by Intense Femtosecond Laser Pulses," Physical Review Letters **96**, 165003 (2006).

76. M. Berger, J. Coursey, M. Zucker, and J. Chang, "Stopping-power and range table for electrons protons and helium ions," http://www.physics.nist.gov/PhysRefData/Star/Text/contents.html (2005).

77. C. Hombourger, "An emperical expression for k-shell ionization cross section by electron impact," Journal of Physics B: Atomic and Molecular Physics **31**, 3693 (1998).

78. J. P. Verboncoeur, A. B. Langdon, and N. T. Gladd, "An object-oriented electromagnetic PIC code," Computer Physics Communications **87**, 199-211 (1995).

79. W. H. Bennett, "Magnetically Self-Focussing Streams," Physical Review **45**, 890 (1934).

80. D. W. Forslund, J. M. Kindel, K. Lee, E. L. Lindman, and R. L. Morse, "Theory and simulation of resonant absorption in a hot plasma," Physical Review A **11**, 679 (1975).

81. Z. L. Chen, G. R. Kumar, Z. M. Sheng, T. Matsuoka, Y. Sentoku, M. Tampo, K. A. Tanaka, T. Tsutsumi, T. Yabuuchi, and R. Kodama, "Transient Electrostatic Fields and Related Energetic Proton Generation with a Plasma Fiber," Physical Review Letters **96**, 084802-084804 (2006).

82. M. Borghesi, A. J. MacKinnon, L. Barringer, R. Gaillard, L. A. Gizzi, C. Meyer, O. Willi, A. Pukhov, and J. Meyer-ter-Vehn, "Relativistic Channeling of a Picosecond Laser Pulse in a Near-Critical Preformed Plasma," Physical Review Letters **78**, 879 (1997).

83. A. Pukhov, "Three-dimensional electromagnetic relativistic particle-in-cell code VLPL (Virtual Laser Plasma Lab)," Journal of Plasma Physics **61**, 425-433 (1999).

VITA

Byoung-ick Cho was born in Seoul, Korea, on May 29 1976, the first son of Myung-won Cho and Kye-ock Chang. After graduating from Hansung Science High School with honors, he entered the Seoul National University in 1995. After sophomore year, he served in the Korean Army for 26 months. He returned to the university in 1999 and received the B.S. degree in physics (*Cum Laude*) in 2001. In the fall, he entered the physics graduate program in the University of Texas at Austin to pursue the Ph.D. Since 2002, he has worked for Dr. Todd Ditmire.

Permanent address: 1624 west 6th street APT J
Austin, TX, 78703

This dissertation was typed by the author.